

DISSERTATION

S-NITROSYLATION MEDIATES SYNAPTIC PLASTICITY IN THE RETINA

Submitted by

Ryan E Tooker

Department of Biomedical Sciences

In partial fulfillment of the requirements

For the Degree of Doctor of Philosophy

Colorado State University

Fort Collins, Colorado

Summer 2015

Doctoral Committee:

Advisor: Jozsef Vigh

Michael Tamkun

Shane Hentges

Kim Hoke

Copyright by Ryan Edward Tooker 2015

All Rights Reserved

ABSTRACT

S-NITROSYLATION MEDIATES SYNAPTIC PLASTICITY IN THE RETINA

Over the course of an entire day, our visual system must accommodate intensities of light that can change by a factor of 10^{10} . In order to do so, the retina adapts to large, daily changes in natural light intensity by shifting its dynamic range of coding. For example, as morning light intensity increases, the retina implements multiple strategies that result in decreases in overall sensitivity in order to avoid saturation. However, adaptation to bright environments poses the inherent risk of losing visual information carried by dim/weak signals in complex natural scenes. Here we studied whether the light-evoked increase in retinal nitric oxide (NO) production is followed by NO-mediated, direct post-translational modification of proteins called S-nitrosylation and if it contributes to the modulation of the dynamic range of vision. In the central nervous system, including the retina, S-nitrosylation has not been considered to be significant under physiological conditions, and instead, has been primarily associated with neurodegenerative diseases.

In this study, we provide immunohistochemical and proteomic evidence for extensive S-nitrosylation that takes place in the goldfish and mouse retinas under physiologically relevant light intensities, in an intensity-dependent manner. Functionally, we report a novel form of activity-dependent synaptic plasticity via S-nitrosylation: a “weighted potentiation” that selectively increases the output of Mb-type bipolar cells in the goldfish retina in response to weak inputs but leaves the input-output ratio for strong stimuli unaffected. Importantly, the NO

action resulted in a weighted potentiation of Mb output in response to small (≤ 30 mV) depolarizations.

Our data strongly suggest that in the retina, light-evoked NO production leads to extensive S-nitrosylation and that this process is a significant post-translational modification affecting a wide range of proteins under physiological conditions. S-nitrosylation may function to extend the dynamic range of vision by counteracting the decreases in retinal sensitivity during light adaptation ultimately preventing the loss of visual information carried by dim scotopic signals. Finally, our results may set the framework for exploring the role of S-nitrosylation in certain neurodegenerative retinal diseases that are associated with toxic levels of NO.

ACKNOWLEDGEMENTS

Over the course of my graduate career, I am fortunate and thankful to have been surrounded by a supportive and helpful environment, which played no small part in my ability to achieve success. I have learned an incredible amount from my advisor, Jozsef Vigh, who I appreciate for his commitment to integrity and humility. Mike Tamkun, Shane Hentges and Kim Hoke were an incredibly supportive advisory committee that challenged me and consistently offered valuable and constructive input. I wish to thank all my co-workers in the Vigh lab, particularly Mikhail Lipin and Valerie Leuranguer for their patience and helpful nature over the years and Shannon Gallagher for his friendship and always being a reminder to value perspectives different than my own.

I also wish to express appreciation to my family, whose love and encouragement were a constant reminder of the incredible support that was always behind me. Finally, I am forever grateful for my wife, Alex, who never batted an eye at the prospect of moving our life for me to pursue my dream. She has been my partner through all of this, sharing in the successes and failures, all the while reminding me that there is always something to celebrate.

TABLE OF CONTENTS

ABSTRACT.....	ii
ACKNOWLEDGEMENTS.....	iv
LIST OF FIGURES	vii
Chapter 1: Introduction.....	1
1.1 The Retina.....	2
1.2 Mechanisms of Light- and Contrast Adaptation in the Vertebrate Retina.....	7
1.3 Nitric Oxide Signaling in the Vertebrate Retina.....	10
1.4 Overall Hypothesis and Aims	16
Chapter 2: Light-Evoked S-nitrosylation in the Retina	17
2.1 Summary.....	17
2.2 Introduction.....	18
2.3 Materials and Methods.....	20
2.4 Results.....	31
2.5 Discussion.....	51
Chapter 3: Nitric Oxide Mediates Activity-Dependent Plasticity of Retinal Bipolar Cell Output via S-nitrosylation.....	58
3.1 Summary.....	58
3.2 Introduction.....	59
3.3 Materials and Methods.....	60
3.4 Results.....	67
3.5 Discussion.....	99

Chapter 4: Conclusion.....	105
4.1 S-nitrosylation Occurs Under Physiological Conditions in the Retina.....	106
4.2 S-nitrosylation Mediates Weighted Potentiation of Mb Output in the Goldfish Retina	109
4.3 S-nitrosylation in Neurodegenerative Diseases	112
4.4 Final Remarks	115
References.....	116
Appendix I	140
Appendix II.....	148
Appendix III.....	162
Appendix IV.....	163

LIST OF FIGURES

1.1 Schematic of retinal anatomy.....	3
1.2 Inherent challenges of a visual scene.....	8
1.3 Schematic of nitric oxide synthesis in neurons.....	12
1.4 NO signaling pathways.....	13
2.1 S-nitrosocysteine immunofluorescence in light- and dark-adapted goldfish retinas.....	32
2.2 S-nitrosocysteine immunofluorescence in light- and dark-adapted WT mouse retinas.....	33
2.3 S-nitrosocysteine immunofluorescence labeling pattern in the goldfish retina is shaped by light intensity.....	35
2.4 Light intensity determines the S-nitrosocysteine immunofluorescence labeling pattern in the wild-type mouse retina.....	38
2.5 Light-evoked S-nitrosylation in the goldfish and wild-type mouse retina is prevented by pre- incubation with N-Ethylmaleimide (NEM).....	42
2.6 Light-evoked S-nitrosylation in the adult retina requires nNOS activation.....	44
2.7 nNOS is necessary for robust S-nitrosylation in the mouse retina.....	46
3.1 Strong depolarization shifted calcium spike threshold in Mb-type bipolar cells.....	68
3.2 Strong depolarization induced modulation of I_{Ca} activation but not I_K kinetics.....	72
3.3 Modulation of I_{Ca} at the Mb terminal is Ca^{2+} dependent and required synaptic signaling.....	76
3.4 Exocytosis of glutamate and activation of neurons postsynaptic to the Mb terminal are required for modulation of I_{Ca}	78
3.5 Activation of postsynaptic neurons potentiated I_{Ca} and exocytosis from Mb terminals.....	81

3.6 The NO donor-mediated shift of I_{Ca} caused weighted potentiation of Mb output selectively in response to weak stimuli	83
3.7 Nitric oxide (NO) modulated I_{Ca} in Mb terminals through a cGMP-independent pathway that involved S-nitrosylation reactions	86
3.8 Photopic light stimulation modulated scotopic light responses of Mb axon terminals	92
3.9 Scotopic light responses of Mb axon terminals can be modulated by light through rod specific pathways	96
3.10 Both bright scotopic and photopic light induced modulation of scotopic light responses in Mb terminals in a NEM sensitive manner	98
4.1 Inhibition of denitrosylation does not alter dark-adapted levels of SNI	109
4.2 S-nitrosylation of GAPDH appears to be required for modulation of I_{Ca}	111

1. Introduction

Imagine you are standing on the corner of a frantically busy intersection, preparing to cross the street. Which of your senses did you engage to realize the scene in your mind? Chances are, you imagined *seeing* the intersection: the contrast of the sidewalk with the blacktop of the road, the different vehicles passing by, the color of the traffic lights indicating right of way, all together creating a visualization of the imagined situation. A substantial portion of our interaction with the world around us relies on our ability to perceive and interpret visual information. In the most extreme cases, our visual system prevents us from stepping into harm's way. While many components make up the entire visual system, the retina is the primary sensory organ tasked with translating visual information, in the form of light, into neuronal signals and propagating these signals to the brain. Therefore, it is critical that the retina is equipped to handle the variety of stimuli that are present in a visual environment.

Over a 24 h day and night cycle, our visual system is subjected to light intensities that change by a factor of $\sim 10^{10}$ (Dowling, 1987; Sterling, 2003). In order to maintain operational vision across this entire range, a series of cellular and synaptic specializations exist to ensure efficient and accurate information processing through the retina. For example, specific cells in the outer retina are designed to transduce dim light efficiently while a distinct subset respond maximally to bright light, thus creating an anatomical cellular designation to accommodate the wide range of light intensities within the natural world (the anatomical design of the retina will be discussed in greater detail below). On the circuitry level, various fast transmitters (i.e. glutamate and GABA) and neuromodulators (i.e. dopamine, nitric oxide) are released in response to changing light intensities and serve to modulate local circuits that are critical in mediating

information transfer through the retina (Wässle, 2004). One neuromodulator of particular interest for this study is nitric oxide (NO) which can exhibit its effects through two distinct mechanisms: (1) NO binds to the most sensitive NO target, soluble guanylate cyclase (sGC) which stimulates cGMP synthesis (Roy et al., 2008), or (2) NO covalently binds to free thiol side-chains of cysteine residues of various proteins in a reaction called S-nitrosylation (for review, see Ahern et al., 2002). Extensive work has described NO's modulatory effects, at many stages of retinal processing, via the $\text{NO} \rightarrow \text{sGC} \rightarrow \text{cGMP}$ pathway, yet there is very little evidence indicating how S-nitrosylation may influence signaling in the vertebrate retina (for review, see Vielma et al., 2012).

This study aimed to describe endogenous protein S-nitrosylation in the vertebrate retina and to characterize how this type of post-translational modification may be involved in modulating visual information processing. This section reviews: (1) the anatomy of the retina, with extra attention given to the cell types and structures pertinent to this study, (2) mechanisms of light- and contrast-adaptation, and (3) nitric oxide signaling in the retina.

1.1 The Retina

The fundamental role of vision is to detect and relay complex information about the outside world, such as contrast, color, and motion, to the brain; a processes which begins in the retina. Although substantial differences exist between species, vertebrate retinas share a similar organizational framework: as a laminar neural tissue, the retina contains two synaptic layers (outer and inner plexiform layers) and three cellular layers (outer and inner nuclear layers and ganglion cell layer) comprised of 5 major cell types (Fig. 1.1; Dowling, 1987; Masland, 2001). Each cell type has distinct subclasses of neurons that form unique circuits and play specific roles

in processing complex visual information (Masland, 2012a). Thus the ability to perceive the visual details of our environment comes down to the complex interplay between distinct retinal neurons and the circuits they create.

Outer Retina

The outer retina is populated by photoreceptors whose cell bodies form the outer nuclear layer (ONL) and synapse in the outer plexiform layer (OPL; Fig. 1.1). Rod and cone photoreceptors are responsible for transducing light into a neuronal signal that is propagated through the layers of the retina (Wässle, 2004). Rods are the most sensitive of the photoreceptors and allow for scotopic vision, which is characterized by dim or low light conditions such as those that would be experienced during starlight. To this point, the sensitivity of rods is such that they will respond to a single photon (Baylor et al., 1979; Schneeweis and Schnapf, 1995) while being prone to saturation at higher intensities (Bloomfield and Dacheux, 2001). Cone photoreceptors, on the other hand, are responsible for mediating photopic vision, characterized by brighter intensities of light, during daylight for example. Importantly, cones can be subdivided into two or three types (depending on species) that express distinct photopigments and selectively respond to different wavelengths of light, which forms the basis for color vision

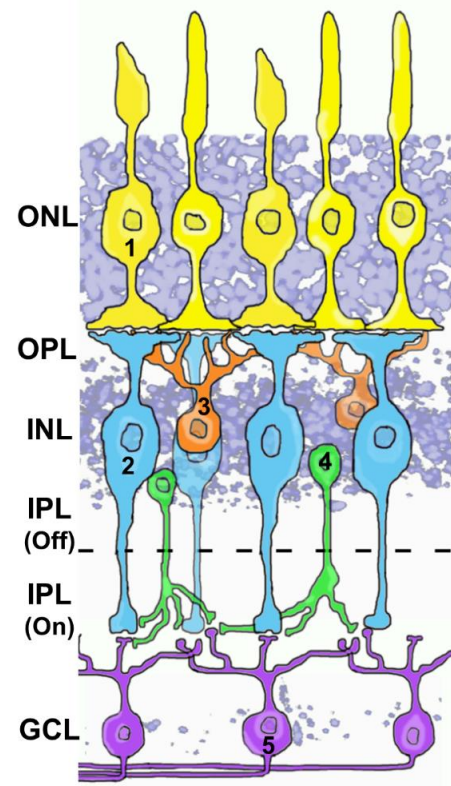


Figure 1.1. Schematic of retinal anatomy. Light is captured by the photoreceptors (1) in the outer nuclear layer (ONL) and the information is passed on to bipolar cells (2) and horizontal cells (3) through synapses in the outer plexiform layer (OPL). Along with the somas of bipolar cells and horizontal cells, the inner nuclear layer (INL) contains the cell bodies of amacrine cells (4). Bipolar cells synapse on ganglion cells (5) in the inner plexiform layer (IPL) which is split into two distinct sublaminae (Off and On). Visual signals are sent to the brain via the optic nerve which is formed by the convergence of individual ganglion cell axons projecting from cell bodies in the ganglion cell layer (GCL).

(Wässle, 2004). However, the intensities that activate rods or cones are not as independent as one would imagine. In the natural world, a significant range of behaviorally relevant light intensities can cause simultaneous activation of both rods *and* cones (Wu, 1994), and this overlap, between the intensities at cone activation threshold and rod saturation, forms the mesopic range (Krizaj, 2000).

In general the primary route for information flow in the retina is through vertical pathways, beginning with phototransduction in rods and cones. Within the OPL, photoreceptor output is sampled by dendritic processes of bipolar cells (BCs) and horizontal cells (HCs). BCs serve as an integral component of the vertical pathway linking the outer retina to the innermost retinal layers. HCs, on the other hand, filter signaling in the OPL by providing inhibitory feedback to photoreceptors and feedforward inhibition to BCs (Fig. 1.1). While the importance of HC modulation of the photoreceptor→BC synapse cannot be understated, it falls outside the scope of this study. Instead, focus will be on the cell types that contribute to the significant signal processing that occurs within the inner retina.

Inner Retina

The inner retina is composed of two individual cellular layers, the inner nuclear layer (INL) and the ganglion cell layer (GCL), which are spatially separated by one synaptic layer, the inner plexiform layer (IPL; Fig. 1.1). In the INL, BCs and amacrine cells (ACs) combine to make up ~80% of the cell population (Fig. 1.1; Jeon et al., 1998). BCs link the outer retina (photoreceptors) to the inner retina by synapsing in the IPL with ACs as well as GCs, which are the output neurons of the retina (Fig. 1.1; Masland, 2001; Wässle, 2004) and whose axons converge to form the optic nerve. A significant proportion of signal processing occurs in the IPL

as a result of AC influence. For example, ACs provide inhibitory feedback to BCs, feedforward inhibition to GCs and also modulate other ACs through lateral inhibition (Masland 2012b). A substantial point of focus for this study is the subtleties of the information transfer between BCs and GCs in the IPL, and in particular, how BC output is influenced by AC feedback. As the sole excitatory input to the GCs, BCs are as much a center for signal processing as they are a relay from outer retina to inner. Therefore, the sections below will address BCs specifically and the ACs that modulate synapses in the IPL.

Bipolar Cells

At present, there are more than 10 distinct types of BCs in the vertebrate retina yet all of them perform the same basic function: they link the sensory neurons (photoreceptors) to the projection neurons (GCs) and release glutamate as the primary neurotransmitter (Euler et al., 2014). However, while they may be generally similar, the characteristics that make BCs unique are central to how they shape and process visual information. In general, BCs synapse with either rods or cones, however in the retina of cold-blooded vertebrates, there are BCs that integrate signal information from both rods *and* cones (Lasansky, 1973; Tachibana, 1999). In the conventional view of the mammalian retina, only one type of bipolar cell contacts rods exclusively while the rest make connections with cones (Boycott et al., 1969; Boycott and Kolb., 1973; Euler et al., 2014). However, recent work by several groups has identified a population of mammalian BCs that receive mixed input from both rods and cones (Euler et al., 2014), indicating the convergence of rod and cone signals on second order neurons is a general feature of the vertebrate retina.

BCs can be subdivided further into either ON or OFF BCs. In general, ON BCs depolarize in response to light and project their axon terminals to the ON sublamina of the IPL,

while OFF BCs hyperpolarize upon illumination of the retina and stratify in the OFF sublamina of the IPL (Fig. 1.1; Euler et al., 1996). This characterization, either ON or OFF, stems from variation in the type of glutamate receptor (ionotropic or metabotropic) expressed on the BC dendrites (Masu et al., 1995; Euler et al., 1996; DeVries, 2000). Without understating the importance of BC modulation in the outer retina, this study will instead focus on mechanisms within the inner retina that modulate BC signaling.

Although some passive filtering occurs as the electrical signal travels down the axon (Oltedal et al., 2007), a significant portion of processing occurs at the axon terminal in the IPL. The temporal and spatial characteristics of glutamate release from the BC axon terminal have profound consequences on activation of GCs (Asari and Meister, 2012), as BCs provide the most significant excitatory input to the GCs. The primary source of modulation of the BC synaptic terminal arrives in the form of feedback from ACs (Boycott et al., 1969; Masland, 2001). AC feedback exerts finely-tuned, local control over the membrane voltage of the BC axon terminal and thus, the dynamics of signaling from the BC to GCs (Vigh et al., 2011).

Amacrine Cells

Amacrine cells are comprised of ~42 morphologically distinct types, making them the most diverse class of retinal interneuron, yet only a few have been studied in substantial detail (Masland, 2012b). Generally considered inhibitory, ACs are sub-classified as either GABAergic or Glycinergic (Masland, 2012b) although GABAergic ACs have been shown to co-express a variety of neuro-active substances such as: dopamine (Wulle and Wagner, 1990), substance P (Ayoub and Matthews, 1992), the endogenous opioid β -endorphin (Gallagher et al., 2010), and nitric oxide (Vielma et al., 2012). As an entire class of retinal neurons, ACs have unique and dedicated functions, making them players in modulating the output of BCs as well as the activity

of GCs and other ACs (Masland, 2001). However, without downplaying the significance of other ACs, this study focuses on ACs that express and release NO (NOACs).

While NOACs are not the exclusive source for NO in the retina, they are presumed to be the predominant source within the inner retina (Vielma et al., 2012). In the mammalian retina, NOACs have been subdivided into 3 main types: I, II, and displaced (Kim et al., 1999). Regardless of type, the dendritic arbors of all NOAC ramify in the ON sublamina of the IPL (Kim et al., 1999). NOACs form synaptic connections with other ACs, as well as GCs in both the ON and OFF sublaminae of the IPL and cone BCs in the ON sublamina (Vielma et al., 2012). Although NOACs have not been shown to make contact directly with rod bipolar cells (RBCs) (Chun et al., 1999), NO release from NOACs has been detected in response to rod-specific light stimulation (Pang et al., 2010b) indicating NOACs are active under scotopic light conditions.

1.2 Mechanisms of Light- and Contrast Adaptation in the Vertebrate Retina

Traditionally, the retina has been described as a simple spatiotemporal filter responsible for sharpening and relaying visual information through the optic nerve to the cortex where the “real” processing can occur that underlies image-forming vision. However, if this were the sole function of the retina, it could be accomplished with far fewer dedicated cell types and circuits than are present in reality (Gollisch and Meister, 2008). Therefore, logic dictates that the wide variety of cell types found in the retina must form distinct circuits tasked with selective computation of visual signals, essentially extracting specific features from the visual scene and relaying them to the cortex. While many mechanisms of signal processing in the retina have been described, this study will focus primarily on mechanisms of adaptation to light and contrast within a visual scene.

Over the course of a day, the intensity of ambient light varies over ~10 orders of magnitude (Dowling, 1987; Sterling, 2003) and the retina is charged with the being able to discriminate relatively small changes in light intensity across this range. A simple, linear solution to ensure coding for this wide range of inputs would be to use an output neuron that can adjust its firing rate 10 fold, reliably matching the range of possible intensity levels. However, the spiking rate of GCs, the output neurons of the retina, is limited to a range spanning only ~2 log units

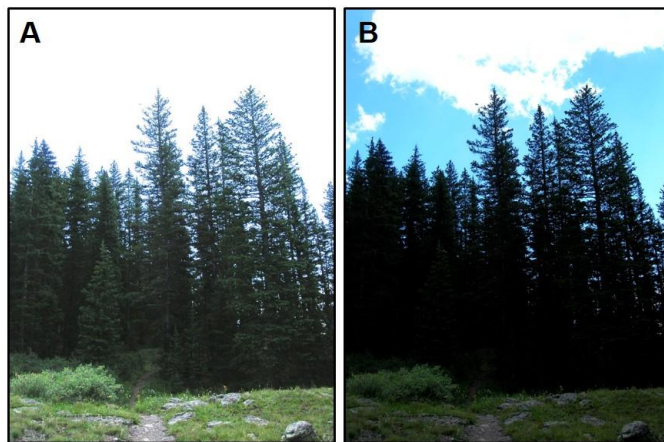


Figure 1.2. Inherent challenges of a visual scene. Identical images representing the two opposing results of sensitization and adaptation. In **A**, the dim and low contrast details of the image are visible, such as the individual trees and hiking path within the shadows. This sensitivity results in complete saturation of the bright, high contrast region, the clouds and the silhouette of the trees against the sky, and detail is lost. If the sensitivity is shifted to accommodate the high intensity/contrast region of the image as illustrated in **B**, the finer details within the shadows are eliminated, but the sky and clouds are now detectable.

(Demb, 2002). In order to overcome this disparity, the retina adapts to the average light intensity (“light adaptation”) as well as to the range of intensities around the mean (“contrast adaptation”) by shifting the dynamic range of coding (Demb, 2002;

Rieke and Rudd, 2009). Adaptation gives the retina the ability to make effective use of the relatively limited range of GC responsiveness and, yet it creates a fundamental challenge: maintain the

sensitivity that provides the coding capability for weak inputs while preventing saturation from high intensity/contrast stimuli (Fig 1.2).

While adaptation is achieved through various strategies and on multiple time scales, the end result is generally the same: saturation is prevented by reducing the overall gain of the system (Fig 1.2; Smirnakis et al., 1997; Demb, 2008). Changes in the firing rate of an individual GC may reflect intrinsic properties of the GC (i.e. Na^+ channel inactivation; Kim and Rieke,

2001; Baccus and Meister, 2002), yet mechanisms that modulate photoreceptor (Thoreson and Mangel, 2012) and BC signaling properties (Rieke, 2001; Manookin and Demb, 2006) can also play pivotal roles in light/contrast adaptation. In the outer retina, neuromodulators have been shown to influence the tuning properties of the circuitry. For example, during light adaptation, dopamine mediates the transition from scotopic to photopic vision by diminishing signal flow through rod circuits and increasing it through cone circuits (Witkovsky, 2004).

In the inner retina, glutamate release from BCs is modulated in an activity dependent manner by inhibitory feedback from nearby ACs (Vigh et al., 2005; Vigh et al., 2011). In this particular instance, light-evoked glutamate release from the BC terminal activated ACs and drove inhibitory feedback (via GABA) that ultimately reduced subsequent glutamate release from the BC terminal (Vigh et al., 2005; Vigh et al., 2011). In the context of classical adaptation, this particular mechanism prevents saturation of the GC by reducing the amount of glutamate released from the pre-synaptic terminal in response to a strong stimulus. Along these lines, a reduction in GC spiking activity has been directly correlated to reduced glutamate release from presynaptic BCs (Manookin and Demb, 2006), which strongly implicates the BC axon terminal as an influential target of modulation during periods of adaptation. Thus, mechanisms and distinct retinal circuits that target BCs, and directly modulate their output, significantly influence retinal adaptation and prevent GC saturation.

While reducing overall retinal sensitivity is key to preventing saturation under bright light conditions, it also introduces the problem of losing the ability to detect weak signals that may carry important visual information within a natural scene. Interestingly, a growing body of evidence suggests that while most GC responses are depressed during adaptation (Smirnakis et al., 1997), others actually become *more* sensitive to weaker inputs (Kastner and Baccus, 2011;

Asari and Meister, 2012; Nikolaev et al., 2013). These reports indicate that adaptation is far more complex than was traditionally assumed and involves opposing forms of plasticity in order to maintain coding ability across the entire dynamic range of vision. In other words, it appears that adaptation does not simply dampen the sensitivity of the entire retina, but instead, compartmentalizes the ability to respond to strong and weak inputs simultaneously. Importantly, the plasticity implicated in driving sensitization in GCs during light and contrast adaptation was suggested to be a result of enhanced efficacy of the BC→GC synapse, primarily through increased glutamate release from the BC terminal (Asari and Meister, 2012; Nikolaev et al., 2013). Although a mechanism responsible for enhanced signaling from the BC terminal was not explicitly defined, a general consensus was that it was a result of specialized AC input directly to the BC terminal (Asari and Meister, 2012, Kastner and Baccus; 2013). Various aspects of adaptation have been attributed to particular neuromodulators, such as dopamine (Witkovsky, 2004; see above), so it is feasible to speculate that the sensitization observed in opposition to adaptation may also be driven through release of specific neuro-active compounds from ACs. One particularly strong candidate for this role is nitric oxide (NO) and the features of NO signaling in the retina are discussed in the section below.

1.3 Nitric Oxide Signaling in the Vertebrate Retina

Since discovering that NO functions as a signaling molecule in the central nervous system (CNS) nearly 30 years ago, our understanding of NO as a neuromodulator has steadily expanded (Garthwaite et al., 1988; Garthwaite, 2008). In the vertebrate central nervous system, NO acts as a neurotransmitter and functions in mediating several behaviors, neurogenesis, memory formation, neuropathy/neuroprotection, and also by modulating physiological signaling

in sensory systems (Garthwaite, 2008; Vielma et al., 2012). Furthermore, NO has garnered significant attention as a potent neuromodulator in the vertebrate retina (Vielma et al., 2012). This section will review synthesis and transmission of NO in general and its influence on retinal function and signal processing.

NO Synthesis and Release

Throughout the body, nitric oxide synthase (NOS) enzymes convert L-arginine to NO; however, the physiological context of NO synthesis is based on the particular isoform of NOS that is active (Alderton et al., 2001; Garthwaite, 2008). In vertebrates, three types of NOS are expressed: neuronal (nNOS), endothelial (eNOS) and inducible (iNOS) isoforms and each have very distinct structural and functional features (Alderton et al., 2001). nNOS and eNOS are constitutively expressed and their activity is calcium-dependent (Knowles and Moncada, 1994; Alderton et al., 2001; Garthwaite et al., 2008). Expression of iNOS, on the other hand, is only elevated in response to inflammation or pathological conditions (Knowles and Moncada, 1994). While all three isoforms have been detected in the vertebrate retina, nNOS is considered to be the main player in influencing visual response via NO (Vielma et al., 2012) and therefore will be given a majority of the attention regarding NO signaling in the retina.

In neurons, Ca^{2+} ions, entering the cell through NMDA receptors, bind and interact with calmodulin which activates nNOS and initiates the liberation of NO from l-arginine (Fig. 1.3; Garthwaite, 1985; Garthwaite et al., 1988). In a simple neuronal circuit, a presynaptic neuron releases glutamate onto a post-synaptic nNOS expressing neuron, driving activation of postsynaptic NMDA receptors and ultimately synthesis of NO. Unlike other neurotransmitters, NO is not packaged into vesicles for release and therefore, as a gaseous, freely diffusible

molecule, NO can function as an anterograde and retrograde volume transmitter (Fig. 1.3; Wood and Garthwaite, 1994; Park et al., 1998, Steinert et al., 2008) making it a potent mediator of neuronal excitability. In the retina, NO is synthesized in a light-dependent manner primarily by nNOS, as made evident by the coincidence of light-evoked NO production with the retinal expression pattern of nNOS, found predominantly in the inner retina (mostly in NOACs; see *Amacrine Cells* section above) of many species (Blute et al., 1997; Eldred and Blute, 2005; Blom et al., 2009; Giove et al., 2009, Pang et al., 2010; Walter et al., 2014; Zhu et al., 2014). Along these lines, light stimulation has been shown to significantly increase NO in the retinas of a number of vertebrate species including carp (Sekaran et al., 2005), salamander, turtle (Eldred and Blute, 2005), rabbit (Neal et al., 1998) and miniature pig (Donati et al., 1995).

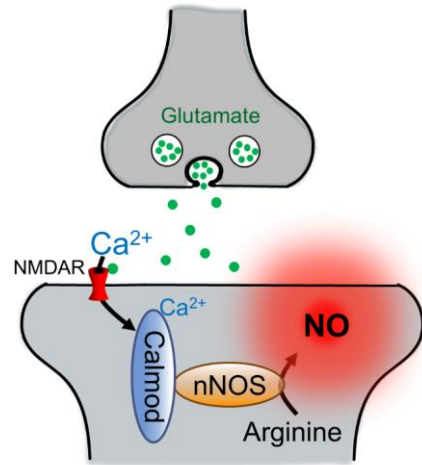


Figure 1.3. Schematic of nitric oxide synthesis in neurons. Presynaptic glutamate release activates postsynaptic NMDA receptors resulting in an influx of Ca^{2+} ions which bind to calmodulin (Calmod), activating the neuronal isoform of nitric oxide synthase (nNOS). nNOS converts l-arginine into NO, and as a gaseous molecule, NO can freely diffuse across the cellular membrane.

Neuromodulatory Effects of NO

Currently, there are two distinct routes by which NO can modulate synaptic transmission: (1) the “classical” cGMP-dependent cascade and (2) direct protein modification via S-nitrosylation (Fig. 1.4; Ahern et al., 2002). In this section, the general overview of each signaling pathway is discussed along with evidence (or lack there of) of its role in information processing in the vertebrate retina.

The “classical” pathway

In the well-characterized traditional view of NO signaling, NO binds to the “NO-receptor” soluble guanylate cyclase (sGC) which stimulates an increase in intracellular cGMP (Fig. 1.4; Southam and Garthwaite, 1993). Elevated levels of cGMP can elicit functional changes in cellular processes by targeting several downstream proteins, however

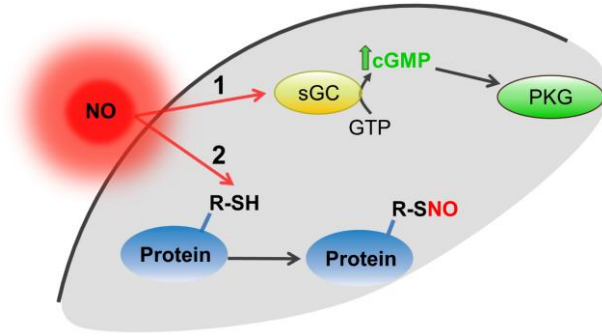


Figure 1.4. NO signaling pathways. **1.** The “classical pathway requires activation of soluble guanylate cyclase (sGC) by NO. This stimulates the production and elevation of intracellular cyclic GMP (cGMP) which can target and activate protein kinase G (PKG). **2.** Additionally, NO can modify proteins directly by binding to free thiols (R-SH), forming nitrosothiols (R-SNO) via S-nitrosylation.

the most widespread effects are attributed to cGMP-dependent activation of protein kinase G (PKG) (Fig. 1.4 #1; Garthwaite, 2008). It is important to note that the designation of the $\text{NO} \rightarrow \text{sGC} \rightarrow \text{cGMP}$ pathway as “classical” or “traditional” is simply a result of it being identified and explored nearly a decade before other routes of action by NO and does not diminish its ability to exert changes in cellular processes.

In the retina, extensive work has described NO’s modulatory effects via the $\text{NO} \rightarrow \text{sGC} \rightarrow \text{cGMP}$ pathway at many stages of retinal processing. The most notable effect of NO in the retina is cGMP-dependent uncoupling of gap junctions between horizontal cells (DeVries and Schwartz, 1989; Lu and McMahon, 1997; Daniels and Baldrige, 2011) and between AII ACs and BCs (Mills and Massey, 1995). In the outer retina, NO has been shown to influence transmission of glutamate to horizontal cells (Bing et al., 1997; Savchenko et al., 1997) as well as decrease the responsiveness of glutamate receptors on horizontal cells (McMahon and Ponomareva, 1996). In the inner retina, NO exerts cGMP-dependent effects on BCs, ACs, and GCs. In BCs, NO has been shown to modulate the light responsiveness and sensitivity through a

cGMP-dependent pathway (Shiells and Falk, 2002; Snellman and Nawy, 2004). In ACs, NO has been implicated in converting the response to GABA from inhibitory to excitatory by mediating an increase in intracellular $[Cl^-]$ (Hoffpauir et al., 2006). At the level of GCs, NO appears to modulate spiking frequency as well as increase voltage-gated calcium channel activity (Hirooka et al., 2000; Kawai and Sterling, 2002). Altogether, the “classical” NO signaling cascade can exert effects on multiple spatial and temporal scales and can play a significant role in the processing of visual information during light adaptation.

S-nitrosylation

In an alternative mechanism, NO can alter protein function directly by covalently binding to free thiol groups of cysteine residues of proteins in a chemical reaction called S-nitrosylation (Fig. 1.4; Stamler, 1994; Ahern et al., 2002). This reversible covalent post-translational modification has been shown to alter protein function (reviewed by Ahern et al., 2002) much like phosphorylation. Thousands of proteins with potential S-nitrosylation sites have been identified and many are associated with neural signaling (Seth and Stamler, 2011). For example, NR2 subunits of NMDA receptors, expressed in heterologous systems, have been shown to undergo S-nitrosylation that inhibits NMDA currents (Choi et al., 2000). It is important to note, however, that a vast majority of the reports describing S-nitrosylation in the CNS use exogenous NO donors to drive robust S-nitrosylation and do not evoke endogenous NO release (Ahern et al., 2002). Initial reports did not detect S-nitrosylated proteins without the application of NO donors, which was assumed to be because endogenous S-nitrosoproteins are present at extremely low levels (Jaffrey et al., 2001). Further experiments exposed a handful of proteins (12) that were endogenously S-nitrosylated under conditions of tonic NO release in the mouse brain (Jaffrey et

al., 2001), however these experiments still lacked information regarding S-nitrosylation following specific stimulation-evoked release of NO.

Compared to the sensitivity of sGC, which can be activated by levels of NO in the nanomolar range (Roy et al., 2008), the S-nitrosylation reaction is thought to require low micromolar NO concentrations, minimally (Ahern et al., 2002; Palmer et al., 2008). This disparity in required concentrations of NO for effective signaling raises the question of whether or not S-nitrosylation can and does occur under physiological conditions in the CNS (Hardingham et al., 2013). Very few reports definitively show endogenous S-nitrosylation in the healthy nervous system, and in fact, detectable (endogenous) S-nitrosylation in neural tissue has been mostly associated with pathophysiological conditions in which nitrosative stress influences the progression of the disease (Nakamura et al., 2013). For example, the pathogenesis of neurodegenerative diseases such as Parkinson's and Alzheimer's is, in part, influenced by S-nitrosylation from aberrant levels of NO (Chung et al., 2004; Qu et al., 2011).

While evidence is scarce regarding the presence of endogenous S-nitrosylation in the CNS, it is almost entirely absent when considering the vertebrate retina. Upon NMDA application, NO-selective electrodes detected $\sim 0.2 \mu\text{M}$ NO near a single GC in the turtle retina (Eldred and Blute, 2005) indicating, at least, that the retina is capable of producing NO levels sufficient to drive S-nitrosylation. However, application of NMDA is commonly used to simulate excitotoxic conditions associated with retinal diseases and to initiate cell death (Siliprandi et al., 1992; Li et al., 1999; Akopian et al., 2014). There is very little evidence indicating that the concentration of NO in the retina reaches high enough levels to facilitate S-nitrosylation under physiological conditions. Although relatively sparse, evidence does exist that carves out a functional role for S-nitrosylation in the vertebrate retina. In 1994, Kureny et al. described an

NO-dependent process that modulated rod photoreceptor ion channels independent of sGC/cGMP. With these data, the authors imply that the observed effect was due to direct nitrosylation of key proteins in the rod photoreceptor transduction machinery. Furthermore, intravitreal injection of exogenous NO donors at low, non-pathological concentrations, amplified the rat electroretinogram (ERG) independent of cGMP (Vielma et al., 2010), leading to the conclusion that NO may have amplified ERG responses via protein nitrosylation. Overall, endogenous protein nitrosylation in the retina represents an exciting and unexplored avenue to understanding how NO can influence visual information processing at various points in the retinal circuitry.

1.4 Overall Hypothesis and Aims

The overall hypothesis of this study is that endogenous S-nitrosylation is present in the vertebrate retina under physiological conditions and underlies functional aspects of signal processing. The basis for this hypothesis is rooted at the crossroads of two key aims regarding retinal physiology: 1) under physiological conditions, endogenous NO drives S-nitrosylation in the vertebrate retina and 2) during periods of light adaptation, mechanisms exist to extend the dynamic range of vision and prevent loss of critical visual information. Aims 1 and 2 will be addressed in chapters 2 and 3, respectively. Finally, chapter 4 will provide preliminary evidence for expanding upon the conclusions made in chapters 2 and 3 and will discuss the implications of S-nitrosylation in the healthy retina and in neurodegenerative diseases.

2. Light-Evoked S-nitrosylation in the Retina¹

2.1 Summary

Nitric oxide (NO) synthesis in the retina is triggered by light stimulation. NO has been shown to modulate visual signal processing at multiple sites in the vertebrate retina, via activation of the most sensitive target of NO signaling, soluble guanylate cyclase. NO can also alter protein structure and function and exert biological effects directly by binding to free thiol groups of cysteine residues in a chemical reaction called S-nitrosylation. However, in the central nervous system, including the retina, this reaction has not been considered to be significant under physiological conditions. Here we provide immunohistochemical evidence for extensive S-nitrosylation that takes place in the goldfish and mouse retinas under physiologically relevant light intensities, in an intensity-dependent manner, with a strikingly similar pattern in both species. Pre-treatment with NEM, which occludes S-nitrosylation, or with TRIM, an inhibitor of neuronal NO synthase, eliminated the light-evoked increase in S-nitrosylated protein immunofluorescence (SNI) in the retinas of both species. Similarly, light did not increase SNI, above basal levels, in retinas of transgenic mice lacking neuronal NO synthase. Qualitative analysis of the light-adapted mouse retina with mass spectrometry revealed more than 300 proteins that were S-nitrosylated upon illumination, many of which are known to participate directly in retinal signal processing. Our data strongly suggest that in the retina, light-evoked NO production leads to extensive S-nitrosylation and that this process is a significant post-translational modification affecting a wide range of proteins under physiological conditions.

¹ Tooker R, Vigh J (2015) J Comp Neurol Advance online publication. DOI: 10.1002/cne.23780. Reproduced with permission: see Appendix I.

2.2 Introduction

As visual signals from photoreceptors are transmitted across the synaptic layers of the retina towards the output elements, the ganglion cells (GCs), they are subjected to modulation by a great variety of neuro active substances. One of these neuromodulators is nitric oxide (NO). Under physiological conditions, NO is synthesized from L-arginine in a light-dependent manner primarily by the neuronal-type nitric oxide synthase (nNOS), as made evident by the coincidence of light-evoked NO production with the retinal expression pattern of nNOS in many species (Blute et al., 1997; Blom et al., 2009; Giove et al., 2009). In vertebrates, the most sensitive target of NO is soluble guanylate cyclase (sGC) which is activated by nanomolar NO concentrations (Roy et al., 2008). It is also the best known path of NO action in the retina: extensive work has described NO's modulatory effects at many stages of retinal processing via the $\text{NO} \rightarrow \text{sGC} \rightarrow \text{cGMP}$ pathway (DeVries and Schwartz, 1989; Mills and Massey, 1995; McMahon and Ponomareva, 1996; Savchenko et al., 1997; Bing et al., 1997; Xin and Bloomfield, 1999; Hirooka et al., 2000; Kawai and Sterling, 2002; Yu and Eldred, 2005; Hoffpauir et al., 2006; Daniels and Baldrige, 2011). However, NO can exert biological effects via another signal transduction pathway: NO can react directly with free thiol groups of cysteine residues of proteins in a chemical reaction called S-nitrosylation (Stamler, 1994; Ahern et al., 2002). This reversible, covalent post-translational modification has been shown to alter protein function (reviewed by Ahern et al., 2002) much like phosphorylation. Thousands of proteins with potential S-nitrosylation sites have been identified, many associated with neural signaling (Seth and Stamler, 2011). For example, NR2 subunits of NMDA receptors, expressed in heterologous systems, have been shown to undergo S-nitrosylation that inhibits NMDA currents (Choi et al., 2000). However, based on NO-donor studies, S-nitrosylation is thought to require at least low

micromolar NO concentrations (Ahern et al., 2002; Palmer et al., 2008), raising the question of whether it can occur under physiological conditions in the CNS (Hardingham et al., 2013). To date, detectable S-nitrosylation in neural tissue has been associated primarily with pathophysiological conditions that are characterized by aberrant, high levels of endogenous NO production (Nakamura et al., 2013): for example, elevated NO-triggered S-nitrosylation can take part in the pathogenesis of Parkinson's and Alzheimer's disease (Chung et al., 2004; Qu et al., 2011).

NO-selective electrodes detected $\sim 0.2 \mu\text{M}$ NO near a single GC in the turtle retina upon NMDA application (Eldred and Blute, 2005), but little evidence supports the notion that in the healthy retina endogenous retinal NO concentrations under physiological conditions might be high enough to cause direct S-nitrosylation of proteins. To that end, in the salamander retina, Kureny et al. (1994) described an NO-dependent process that modulated rod photoreceptor ion channels independent of sGC/cGMP. Likewise, exogenous application of NO donors at low, non-pathological concentrations, via intravitreal injection, amplified the rat electroretinogram (ERG) independent of cGMP (Vielma et al., 2010), leading to the conclusion that NO may have amplified ERG responses via protein nitrosylation. Recently, we reported evidence of a modulatory process in which endogenous retinal NO mediated activity-dependent plasticity of Mb-type bipolar cell (Mb) output in the goldfish retina through S-nitrosylation (Tooker et al., 2013).

Here we present immunohistochemical evidence describing S-nitrosylation in the adult retina under normal physiological conditions, triggered by endogenous NO. Importantly, we show that light induces S-nitrosylation with a similar pattern in goldfish and mouse retinas and the extent of immunolabeling depends on the intensity of illumination in both species. Our

results are consistent with the notion that retinal NO production/release depends on the light intensity and we confirm that light-induced NO production that causes S-nitrosylation is mediated by the nNOS isoform in both goldfish and mouse. Therefore, we propose that light-evoked, NO-mediated S-nitrosylation in the vertebrate retina is a ubiquitous, dynamic modulatory process that exists across species and may function to modify the transfer of light information at multiple sites of actions within specific synaptic locations. Finally, using mass spectrometry, we provide the first descriptive account of the identities of retinal proteins that are subject to light-dependent S-nitrosylation via endogenous NO. Our findings provide a framework for future investigations of NO-mediated modulation of retinal function.

2.3 Materials and Methods

Animals

Adult male and female wild type C57BL/6J (WT; Jackson laboratories, Bar Harbor, ME, RRID: IMSR_JAX:000664) mice were used for a majority of the experiments requiring mammalian retinas. We also used retinas from adult male and female mice lacking the α isoform of neuronal nitric oxide synthase (nNOS α). These animals were generated on a C57BL/6 background by deletion of exon 6, the heme binding domain, in the nNOS gene (Gyurko et al. 2002; originally generated by P. Huang, Harvard Mass General Hospital and generously provided by S. Tobet, Colorado State University, RRID: IMSR_JAX:008519). Mice containing the genetic deletion were backcrossed to C57BL/6 mice for more than 10 generations. All mice were housed under a constant 12 h light/dark cycle with lights on at 6:00 am and were fed standard rodent chow and water *ad libitum*.

Adult 4- to 5-inch long Goldfish (*Carassius auratus*) of either sex were kept on a 12 h light/dark cycle with lights on at 10:00 am. All animals were handled in compliance with the Colorado State University Institutional Animal Care and Use Committee and all experiments and procedures met United States Public Health and Service Guidelines.

Eyecup Preparation

For all experiments, animals were killed between 10:00 and 14:00 hours. Mice were anesthetized with isoflurane and decapitated before both eyes were enucleated. Goldfish were anesthetized with MS 222 before decapitation and enucleation. MS 222 stock solution (1000x) was made fresh in saturated bicarbonate buffer (pH: 7.5) which was mixed into the holding water to achieve 100 mg/l final concentration. Eyecups from both mouse and goldfish eyes were made by removing the cornea and lens. For all experiments, eyecups were maintained in bicarbonate buffered Ames' medium (US Biological, Salem, MA) supplemented with 1.15 mM CaCl₂. The pH was set to 7.45 with NaOH. The osmolarity was 290 ± 5 mOsmol for mouse eyecups and 260 ± 2 mOsmol for goldfish eyecups and in both cases the solution was gassed continuously with 95% O₂/5% CO₂.

Light Exposure of Eyecup Preparations

To obtain fully light-adapted retinal tissue, the animal was subjected to ambient light for at least 1 h before the eyecups were made under a standard dissection microscope. For all other experiments, animals were dark-adapted for at least 3 h before the preparation took place under infrared illumination as previously described (Vigh et al., 2011). Quantified light exposure of the fully dark-adapted eyecups was accomplished using full-field illumination by green ($\lambda=505$ nm)

LEDs (American Bright Optoelectronics, Chino, CA) with various intensities and durations. The light intensity was calibrated with an optical meter (model 1918-C, sensor 918D-SL-OD3; Newport, Irvine, CA). Dark-adapted eyecups were illuminated with 10^{10} photons/cm²/s for 10 s to mimic mesopic light stimulation and for 500 ms with 2.4×10^8 photons/cm²/s as scotopic light stimulation (Busskamp et al., 2010; Joselevitch and Kamermans; 2009). For experiments requiring incubation in specific pharmacological agents, the drug was added to the Ames' media. One eyecup was incubated in the drug solution while the other eyecup was kept in un-altered control Ames' medium for the same length of time as the drug-incubated eyecup in complete darkness, prior to light stimulation. Mouse and goldfish eyecups were incubated in Ames' medium containing 1 mM N-Ethylmaleimide (NEM; Tocris Bioscience Bristol, UK) for 20 min or 50 μ M 1-(2-Trifluoromethylphenyl)imidazole (TRIM; Tocris Bioscience Bristol, UK) for 30 min prior to 10 s of mesopic light stimulation.

Immunohistochemistry

Light-adapted, dark-adapted and light stimulated eyecups were fixed at room temperature in freshly prepared 4% paraformaldehyde in 0.1 M phosphate-buffered saline (PBS; pH 7.45) for 20 min while protected from further light exposure. Cryostat-sectioned retinas were used for standard immunohistochemistry as previously described (Gallagher et al., 2010) with one minor adjustment: extreme care was taken to protect the retinal tissue from direct light exposure during every experimental step, beginning with fixation, as direct light can reverse and eliminate the S-nitrosylation moiety (Forrester et al., 2007). Retinal sections were permeabilized for 20 min in 0.5% Triton X-100 in 0.1 M PBS and then immediately blocked for 1 h in 5% bovine serum albumin (BSA) containing 0.5% Triton X-100 in 0.1 M PBS. The sections were incubated in

blocking solution containing rabbit anti-S-nitrosocysteine (Abcam, Cat# ab50185, RRID: AB_881716) and mouse anti-PKC α primary antibodies (Enzo Life Sciences, Cat# KAM-PK020D, RRID: AB_2168539) (Table 2.1) overnight at room temperature. Sections were washed 3 X 15 min in 0.1 M PBS and then incubated for 2 h at room temperature in secondary antibodies donkey anti-rabbit Cy3 (Millipore, Cat# ap182C, RRID: AB_92588) and chicken anti-mouse fluorescein (Rockland, Cat# 610-9202, RRID: AB_218559), diluted 1:400 in blocking solution. Slides were washed 3 X 15 min with 0.1 M PBS and mounted in Vectashield (Vector labs, Burlingame, CA). For all immunohistochemical preparations, treated and control tissue were run in parallel, including a treated and a control retinal section on a single slide, to account and control for any inter- and intra-experimental differences.

Antibody Characterization

The primary antibodies used in this study are listed in Table 2.1.

Table 2.1. Primary antibodies used

Antigen	Immunogen	Manufacturer, Cat. #, host species, mono- vs. polyclonal, RRID	Dilution used
S-nitrosocysteine	S-nitrosylated cysteine-KLH	Abcam, cat. #ab50185, rabbit polyclonal, RRID: AB_881716	1:100
Protein Kinase Ca (PKC α)	Bovine Brain PKC α	Enzo Life Sciences, cat. #KAM-PK020D, mouse monoclonal, RRID: AB_2168539	1:200

S-nitrosocysteine

The polyclonal S-nitrosocysteine antiserum was raised in rabbit against S-nitrosylated cysteine conjugated to keyhole limpet hemocyanin (KLH) followed by purification via ion-exchange chromatography. The antibody specifically recognizes S-nitrosocysteine-BSA in

immunoblotting and ELISA but does not recognize unconjugated BSA (Abcam; Cat#: ab50185, RRID: AB_881716; Table 2.1). The specificity of the antibody was demonstrated by Chakrabarti et al. (2010) who reported a ~70-80% loss in specific staining when S-nitrosylated human umbilical vein endothelial cells were incubated for 10 min with 100 μ M DTT, a strong reducing agent capable of eliminating the nitrosothiol moiety from the cysteine. Further characterization was reported by Rossi-George and Gow (2013) who asserted that the detection of S-nitrosocysteine immunofluorescence from LPS treated BV2 cells remained present after antigen competition by pre-incubation of the primary antibody with S-nitrosoglutathione (GSNO), indicating that the antibody was specifically recognizing S-nitrosocysteine and not other nitroso compounds. Additionally, Rossi-George and Gow (2013) showed a reduction in S-nitrosocysteine immunofluorescence in BV2 cells that were treated with LPS and then subjected to strong reducing conditions using organic mercury as the reducing agent. In our hands, we saw a dramatic reduction in S-nitrosocysteine immunolabeling when we incubated the retinal tissue in 1 mM NEM for 20 min prior to light stimulation, when compared to control retinas which received the exact same light stimulation (Compare Figs. 2.3 and 2.4 with Fig. 2.5). This is consistent with the notion that NEM covalently binds to sulfhydryl groups with high affinity (Smyth et al., 1960) thereby preventing consecutive S-nitrosylation by NO (Hu et al., 2012).

Protein Kinase C α

Bovine brain protein kinase C α (PKC α ; UniProt ID: P04409) was used as the immunogen for production of the monoclonal antiserum in mouse. The affinity purified antibody specifically recognizes a band of ~80 kDA by Western blot in mouse and fish (Enzo Life Sciences, Cat# KAM-PK020D, RRID: AB_2168539; Table 2.1). This primary antibody labels the appropriate pattern in the mouse that corresponds to mouse rod bipolar cells (RBCs; Greferath et al., 1990;

Haverkamp and Wässle, 2000) as well as the appropriate pattern in the goldfish retina which corresponds to Mbs (Negishi et al., 1988; Suzuki and Kaneko, 1990; Yazulla and Studholme, 1992).

Confocal Laser Microscopy and Analysis

Fluorescent images were taken using a Zeiss LSM 510 confocal microscope (Carl Zeiss, Oberkochen, Germany). Digital images were acquired separately from each laser channel and then merged to avoid crosstalk between channels. Images were acquired at 40X; for Z-stacks, 2 μm increments were used. Laser power and acquisition settings were kept identical across all retinal sections imaged. Images were compiled using Zeiss LSM Images Examiner software (Carl Zeiss, Oberkochen, Germany). For representative images, brightness and contrast were adjusted in Photoshop CS4 (version 11.0; Adobe, San Jose, CA) and all adjustments were made uniformly to the entire digital image. Quantification of immunofluorescence was performed on raw, unadjusted images of retinal sections using the Plot Profile tool in Image J (version 1.49c; NIH, Bethesda, MD, RRID: nif-0000-30467). For this analysis, we made selections of uniform size (1290 X 575 pixels) from the raw images (i.e. one selection each from the channels corresponding to S-nitrosocysteine and PKC α immunolabeling), ensuring all retinal layers were present in the vertical orientation of the selection. The intensity profile of the fluorescent signal associated with S-nitrosocysteine or PKC α immunolabel was obtained by applying the Plot Profile tool which horizontally integrated the intensity across the entire digital image selection (gray line in Fig. 2.1B and E and in Fig. 2.2B and E). The average intensity of fluorescence was calculated for each individual retinal layer from each unique plot profile after background fluorescence was subtracted, similar to the method reported by Vielma et al. (2010). In this

manner, we were able to systematically quantify the intensity and pattern of S-nitrosocysteine immunofluorescence across the retinal layers (Figs. 2.1G and 2.2G). For retinal sections from eyecups stimulated with mesopic or scotopic light, we compared the extent to which the S-nitrosylation immunolabeling was distributed within the IPL, specifically, what percentage was located within the Mb/RBC terminal region. During this analysis, we divided the integral of the intensity profile curve for the region defined only by the terminals of Mbs/RBCs by the integral of the curve associated with the entire IPL. To determine the boundaries of the terminal region in the profile of the S-nitrosocysteine plot, we used the intensity profile from the PKC α fluorescence and correlated the exact pixels corresponding to the beginning and end of the terminal region. Integrals from individual images were averaged to obtain a final overall average for the integral of the intensity within the entire IPL and the intensity specific to the terminal region. Colocalization of the S-nitrosocysteine immunolabeling and the terminal region of the Mbs/RBCs was determined for individual goldfish Mb terminals or terminal clusters for mouse RBCs using images taken from a single optical plane to avoid exaggeration of the coincidence of colocalization. The JACoP plugin in the Image J software (version 1.49c; NIH, Bethesda, MD, RRID: nif-0000-30467) was used to calculate the Manders' coefficient for 100 X 100 pixel square selections of Mb terminals or RBC terminal clusters were cut out from single-plane confocal images. Note that the Manders' coefficient, M1, returns a value between 0 and 1, corresponding to the ratio of "summed intensities of pixels from the green image for which the intensity in the red channel is above zero to the total intensity in the green channel" and vice versa for M2 (Bolte and Cordelières, 2006). As the Manders' coefficient is sensitive to noise and might provide a false positive correlation (Bolte and Cordelières, 2006), we used the Costes' approach to ensure accurate measures of coincidence: the Costes' approach, sets an automatic

value for intensity threshold, thereby eliminating noise and setting the background value to zero. Statistical analysis was completed using Prism (version 6.01; GraphPad, San Diego, CA, RRID: rid_000081). Unpaired Student's *t* tests were used for comparison between individual groups and one-way ANOVA with Tukey's multiple comparison tests were performed across multiple groups. Comparisons across experiments were justified by performing the immunohistochemistry and imaging of the retinal tissue from the experimental group (i.e. drug treated) in parallel with at least one tissue slide from each group involved in the comparison (i.e. dark-adapted or control incubation without drug). All data are presented as mean +/- SEM, with $p < 0.05$ considered significant.

Identification of S-nitrosylated Proteins

Biotin-Switch Assay

Retinal lysates were made by homogenizing the 2 retinas, obtained from individual light- or dark-adapted mice, in ice-cold lysis buffer (S-nitrosylation Buffer A, Cayman Chemical, Ann Arbor, MI, Item #10006520), supplemented with 1 mM Phenylmethanesulfonyl fluoride (PMSF, Sigma, St. Louis, MO). Retinal lysates were obtained in triplicate (i.e. from 3 animals) in either a dark- or light-adapted state, providing 6 total lysates to be used. The homogenized lysates were centrifuged at 1,000xg for 10 min at 4°C to remove debris. The supernatant was collected and used as the starting material for the biotin-switch assay using the S-nitrosylated Protein Detection kit (Cayman Chemical, Ann Arbor, MI, Item #10006518). The S-nitrosylated Protein Detection Kit is a modified version of the biotin-switch assay described by Jaffrey et al. (2001) in which only proteins containing the S-nitrosylation moiety are covalently labeled with a biotin in place of the nitrosothiol group. The steps in the S-nitrosylated protein detection kit were

followed exactly and extreme care was taken to prevent exposure of the sample to light (fluorescent and/or sunlight) as this can cause inappropriate biotinylation and ultimately false positive protein identification (Forrester et al., 2007). Following completion of the assay per the kit, the protein samples were suspended in 200 μ L of wash buffer (S-nitrosylation wash buffer, Cayman Chemical, Ann Arbor, MI, Item # 10006519) with 1 mM PMSF and stored at -20°C overnight.

NeutrAvidin Resin-Assisted Capture of Biotinylated Proteins

Prior to incubation with protein sample, 100 μ L of settled NeutrAvidin agarose resin (Pierce Biotechnology, Rockford, IL) was blocked by incubation with 2.5% biotin-free BSA (Sigma, St. Louis, MO) in 0.1 M PBS for 1 h at room temperature. The blocking solution was removed and the protein samples (200 μ L) were incubated with the NeutrAvidin agarose resin for 2 h at room temperature. The resin was washed 5 X 20 min in 0.1 M PBS. After washing all of the unbound protein, the biotinylated proteins were removed from the resin by 4 X 20 min incubations in 150 μ L of the elution buffer: 8 M guanidine-HCL (ThermoFisher Scientific), pH 1.5. All of the elution buffer fractions were collected and combined to ensure maximum protein recovery from the resin. The entire 500 μ L volume of elution buffer containing the biotinylated proteins was immediately dialyzed against 0.1 M PBS for 24 h at 4°C. The eluates were precipitated from the PBS via trichloroacetic acid (TCA) protein precipitation using deoxycholate. The precipitated protein pellets were resuspended in 50 μ L 0.1 M PBS and stored at -20°C. Protein concentration was determined by BCA analysis (Thermo Scientific, Rockford, IL).

Sample Preparation for LC-MS/MS Analysis

Protein samples from light-adapted (n=3) and dark-adapted (n=3) were submitted to the Proteomics and Metabolomics Facility at Colorado State University. Samples were processed for in-solution trypsin digestion as previously described (Schauer et al., 2013). Briefly, protein was precipitated out of solution in the presence of 4 volumes of 100% -20° C acetone and then resolubilized in 8 M urea, 0.2% ProteaseMAX surfactant trypsin enhancer (Promega, Madison, WI). Samples were reduced and alkylated with 5 mM dithiothreitol and 5 mM iodoacetamide. Trypsin (MS Grade, Thermo Pierce, San Jose, CA) was added at an enzyme to substrate ratio of 1:50 and incubated at 37° C for 3 h. Trypsin was deactivated with the addition of 5% trifluoroacetic acid and desalted using C18 OMIX tips (Agilent Technologies, Santa Clara, CA) using manufacturer's instructions. Peptide eluate was dried in a vacuum evaporator and resuspended in 3% acetonitrile/0.1% formic acid at a concentration of approximately 1 µg/µL.

LC-MS/MS Analysis

Approximately 2 µg of tryptic digest for each sample was injected using an EASY nanoLC-II system (Thermo Scientific, San Jose, CA). Peptides were purified and concentrated using an on-line enrichment column (EASY-Column, 100 µm ID x 2 cm ReproSil-Pur C18). Subsequent chromatographic separation was performed on a reverse phase nanospray column (EASY-Column, 3µm, 75 µm ID x 100 mm ReproSil-Pur C18) using a 90 min linear gradient from 10%-35% buffer B (100% ACN, 0.1% formic acid) at a flow rate of 400 nL/min. Peptides were eluted directly into the mass spectrometer (Thermo Scientific Orbitrap Velos). The instrument was operated in Orbitrap-LTQ mode where precursor measurements were acquired in the Orbitrap (60,000 resolution) and MS/MS spectra (top 20) were acquired in the LTQ ion trap with a normalized collision energy of 35%. Mass spectra were collected over a m/z range of 400-

2000 Da using a dynamic exclusion limit of 2 MS/MS spectra of a given peptide mass for 30 s (exclusion duration of 90 s). Compound lists of the resulting spectra were generated using Xcalibur 2.2 software (Thermo Scientific) with a S/N threshold of 1.5 and 1 scan/group.

Database Search and Protein Identification Criteria

Tandem mass spectra were extracted, charge state deconvoluted and deisotoped by ProteoWizard (version 3.0; MSConvert, RRID:OMICS_03354). All MS/MS samples were analyzed using Mascot (version 2.3.02; Matrix Science, London, UK). Mascot was set up to search the UniProt-KB *Mus Musculus* reverse-concatenated database (102,390 entries, downloaded January, 2013, RRID:nlx_53981) assuming the digestion enzyme was trypsin with a missed cleavage tolerance set to 2. Mascot was searched with a fragment ion mass tolerance of 0.80 Da and a parent ion tolerance of 20 PPM. Oxidation of methionine and carbamidomethyl of cysteine were specified in Mascot as variable modifications. Search results were compiled and validated using Scaffold (version 4.4.0; Proteome Software, Portland, OR). Peptide identifications were accepted if they could be established at greater than 90.0% probability by the Scaffold Local False Discovery Rate (FDR) algorithm. Protein identifications were accepted if they could be established at greater than 99.0% probability to achieve an FDR less than 1.0% and contained at least 2 identified peptides. The number of accepted peptide identifications for each identified protein was reported as the peptide score in Table 2.2 (Appendix II). Protein probabilities were assigned by the Protein Prophet algorithm (Nesvizhskii et al., 2003). Proteins that contained similar peptides and could not be differentiated based on MS/MS analysis alone were grouped to satisfy the principles of parsimony.

2.4 Results

Light Adaptation Induces S-nitrosylation in All Retinal Layers

In the dark-adapted retina, the concentration of NO is present at a minimal, tonic level, however as the retina becomes light-adapted, NO synthesis is initiated and NO levels are substantially elevated (Neal et al., 1998; Walter et al., 2014). As NO levels tend to increase during light adaptation, it stands to reason that levels of S-nitrosylated proteins become elevated as well. To evaluate this possibility, we compared the levels of S-nitrosylation, by assessing S-nitrosocysteine immunofluorescence (SNI), over entire retinal sections from light-adapted and dark-adapted goldfish. For these, and all other images obtained from goldfish retinas, Mbs were identified by PKC α immunoreactivity and served to provide orientation and identification of the synaptic layers within the retina (Fig. 2.1A and D). In the light-adapted goldfish retina, we observed a robust SNI; the pattern of intense immunolabeling extended to all layers of the retina (Fig. 2.1B and C). In contrast, the overall intensity of SNI in the dark-adapted goldfish retina was drastically less than that of the light-adapted one and the pattern of labeling was also different (Fig. 2.1E and F). Specifically, in the dark-adapted goldfish retina, SNI was limited to the ganglion cell layer (GCL) and photoreceptor layer (PL) with greatest intensity within the GCL. Quantitative analysis of the fluorescence intensity of the S-nitrosylation signal (see Materials and Methods) revealed that, on average, the light-adapted goldfish retina (n=8 sections from 4 retinas) displayed significantly more S-nitrosylated proteins than the dark-adapted goldfish retina (Fig. 2.1G; n=7 sections from 2 retinas). This was consistent with previous reports describing levels of NO as being lowest when the retina is dark-adapted (Neal et al., 1998; Sekaran et al., 2005; Walter et al., 2014). These results also suggest that basal NO release in the dark-adapted

retina reaches sufficient levels to cause S-nitrosylation that is detectable by immunohistochemical methods.

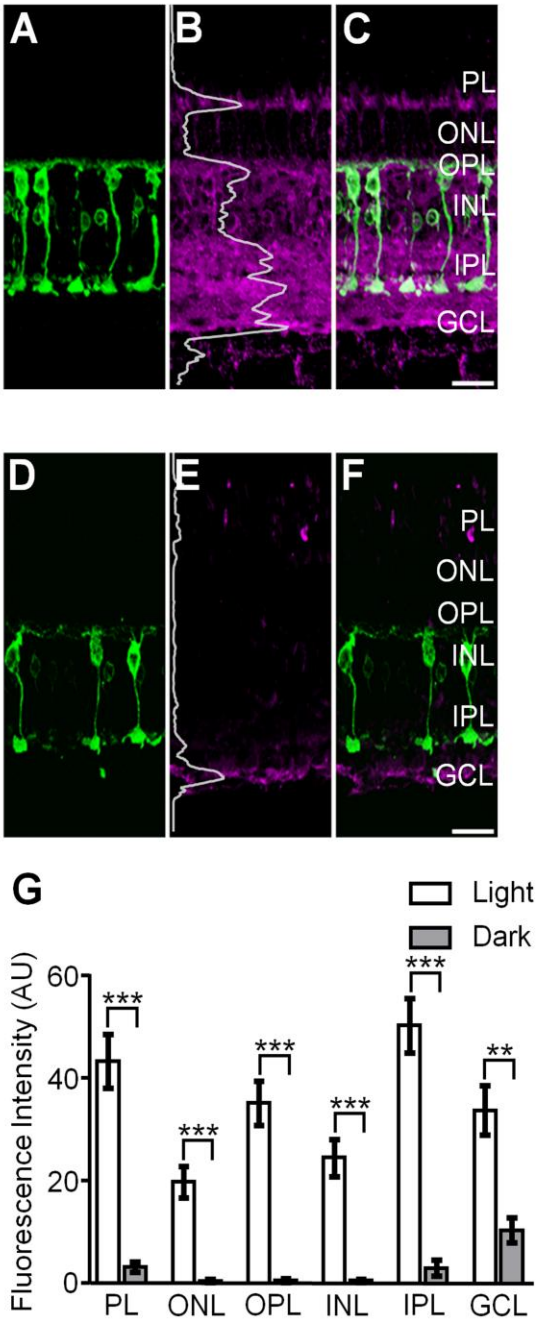
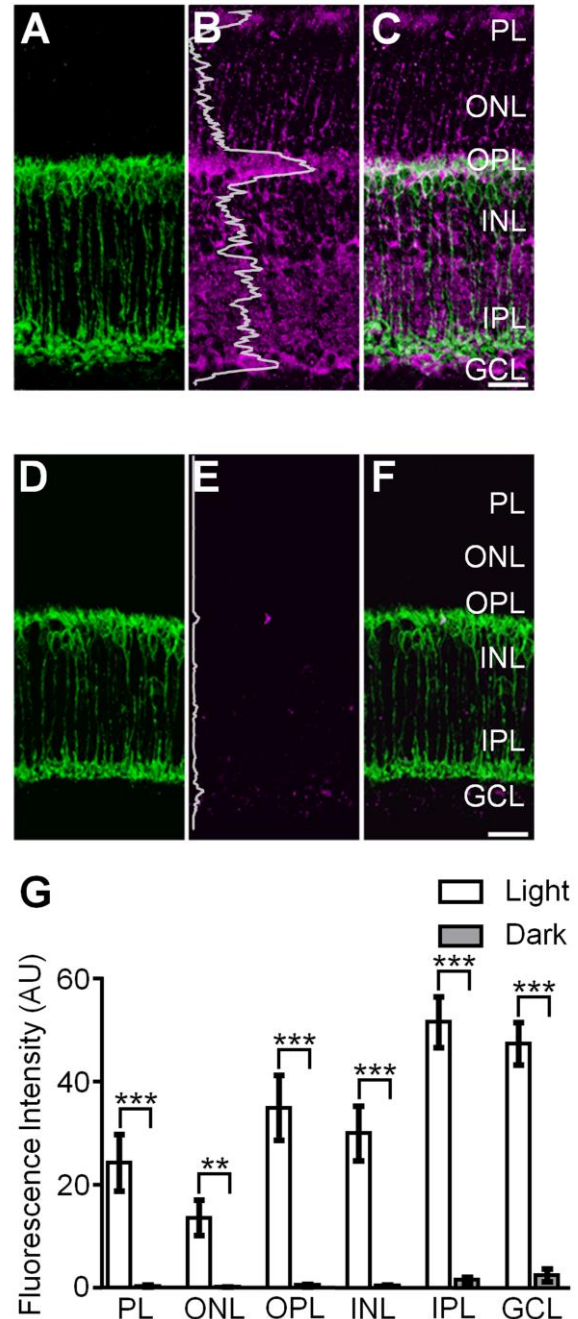


Figure 2.1. S-nitrosocysteine immunofluorescence in confocal images of vertical cryostat sections from light- and dark-adapted goldfish retinas. **A, D:** PKC α positive Mbs (green) in the light- and dark-adapted goldfish retina. **B:** Confocal image of the same region presented in **A** showing that in the light-adapted goldfish retina, SNI (magenta) was present in all retinal layers. Fluorescence intensity was integrated horizontally across the image (the gray superimposed trace) and indicated the relative amount and location of S-nitrosylated proteins in the light-adapted retina. **C:** Merged image of **A** and **B** showing colocalization of SNI and PKC α + cells as a component of the robust S-nitrosocysteine labeling pattern across all retinal layers. **E:** Confocal image of the same region represented in **D** showing SNI in the dark-adapted goldfish retina. The superimposed gray trace illustrates the fluorescence intensity plot of the SNI and indicates a significant lack of S-nitrosocysteine + label in the dark-adapted goldfish retina. Of note: confocal images in **B** and **E** were obtained using the exact same laser power settings and the intensity plot profiles in **B** and **E** are plotted on the same scale. **F:** Merged image of **D** and **E** illustrating the weak S-nitrosocysteine labeling pattern in select retinal layers. **G:** Summary graph illustrating S-nitrosylation, as determined by the fluorescence intensity of SNI, is significantly greater in every retinal layer of the light-adapted goldfish retina as compared to the dark-adapted goldfish retina. Unpaired Student's *t* test, ***: $p \leq 0.0005$, **: $p \leq 0.005$, light-adapted: $n=4$ retinas, dark-adapted: $n=2$ retinas. Data is presented as mean \pm SEM. PL: Photoreceptor Layer; ONL: Outer Nuclear Layer; OPL: Outer Plexiform Layer; INL: Inner Nuclear Layer; IPL: Inner Plexiform Layer; GCL: Ganglion Cell Layer. SNI: S-nitrosocysteine immunofluorescence. Scale bars=20 μ m.

Considering that light-evoked NO synthesis and release has been described in a number of species, including retinas of cold blooded vertebrates and mammalian retinas (Vielma et al., 2012), we then shifted our attention to a mammalian preparation to determine whether light

induces S-nitrosylation, detectable by immunohistochemical methods, in the mouse retina. For all mouse retinal sections, PKC α immunoreactivity was used to identify rod bipolar cells (RBCs) and orient the observer within the various retinal layers (Fig. 2.2A and D). The light-adapted mouse retina showed a robust labeling pattern of SNI, spanning all layers of the retinal section (Fig. 2.2B and C). This robust labeling was in stark contrast to the near absence of SNI labeling

Figure 2.2. S-nitrosocysteine immunofluorescence in confocal images of vertical cryostat sections from light- and dark-adapted wild-type mouse retinas. **A, D:** PKC α positive rod bipolar cells (RBCs, green) in the light- and dark-adapted wild-type mouse retina. **B:** Confocal image of the same region presented in **A** showing SNI (magenta) was present in all retinal layers of the light-adapted wild-type mouse retina. The relative amount and location of S-nitrosylated proteins in the light-adapted retina was illustrated by the fluorescence intensity (the gray superimposed trace) which was integrated horizontally across the image. **C:** Merged image of **A** and **B** showing the robust S-nitrosocysteine labeling pattern across all retinal layers. Note the colocalization of SNI and PKC α + RBCs. **E:** Confocal image of the same region represented in **D** showing SNI in the dark-adapted wild-type mouse retina. The superimposed gray trace illustrates the fluorescence intensity plot of the SNI and indicates a substantial reduction of S-nitrosocysteine + label in the dark-adapted wild-type mouse retina as compared to the light-adapted retina. Of note: confocal images in **B** and **E** were obtained using the exact same laser power settings and the intensity plot profiles in **B** and **E** are plotted on the same scale. **F:** Merged image of **D** and **E** illustrating the faint and nearly absent S-nitrosocysteine labeling pattern in the dark-adapted wild-type mouse retina. **G:** Summary graph illustrating S-nitrosylation, as determined by the fluorescence intensity of SNI, is significantly greater in every retinal layer of the light-adapted wild-type mouse retina as compared to the dark-adapted wild-type mouse retina. Unpaired Student's *t* test, ***: $p \leq 0.0005$, **: $p \leq 0.005$, light-adapted: $n=8$ retinas, dark-adapted: $n=6$ retinas. Data is presented as mean \pm SEM. Scale bars=20 μ m.



in the dark-adapted mouse retina (Fig. 2.2E and F). By comparison, the average intensity of SNI in individual retinal layers was significantly increased across all layers in the light-adapted retina (n=8 sections from 8 retinas) compared to dark-adapted (n=7 sections from 6 retinas) (Fig. 2.2G). When taken all together, these data indicate strongly that retinal S-nitrosylation is light-dependent and becomes increasingly more prevalent at higher, stronger light intensities in both goldfish and mouse retinas.

The Pattern of Light Driven SNI Across Retinal Layers is Intensity Dependent

In the natural world, a significant range of behaviorally relevant light intensities can cause simultaneous activation of both rods *and* cones (Wu, 1994). The overlap between the intensities at cone activation threshold and rod saturation forms the mesopic range (Krizaj, 2000). Indeed, in the goldfish retina, a rod saturating green light (1×10^{10} photons/cm²/s, 505 nm) will also activate cones (Joselevitch and Kamermans, 2007). Compared to baseline levels of SNI in the dark-adapted goldfish retina (Fig. 2.1E), SNI evoked by a 10 s exposure to mesopic light stimulus was significantly higher in the PL (Fig. 2.3B and C; n=9 sections from 4 retinas) (p=0.03, unpaired Student's *t* test), in the OPL (p=0.01, unpaired Student's *t* test), in the INL (p=0.003, unpaired Student's *t* test), in the IPL (p<0.0001, unpaired Student's *t* test) and in the GCL (p=0.003, unpaired Student's *t* test). Although every layer, except the ONL, showed an increase in SNI intensity above basal levels, the most dramatic increase occurred within the IPL (8 fold increase from dark-adapted levels). Furthermore, mesopic green light stimulation induced an SNI labeling pattern in the IPL that clearly labeled cellular structures, particularly the large, bulbous terminals of Mbs (Fig. 2.3D, E and F), consistent with our previous results indicating physiologically relevant S-nitrosylation within the Mb terminal (Tooker et al., 2013). Note that

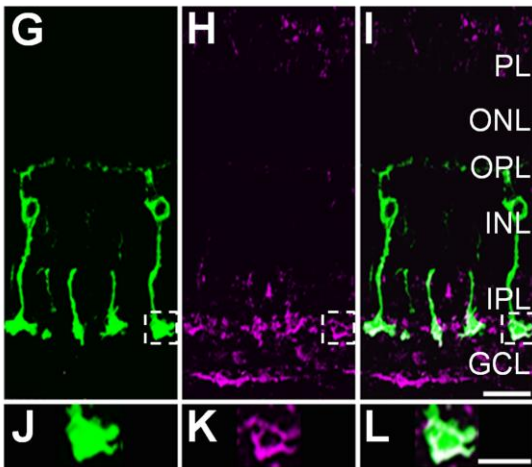
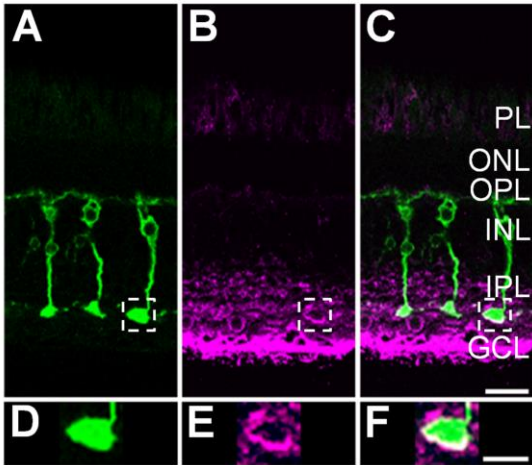


Figure 2.3. S-nitrosocysteine immunofluorescence labeling pattern in the goldfish retina is shaped by light intensity. For panels **A-F**, a dark-adapted goldfish retina was stimulated with rod saturating mesopic light (1×10^{10} photons/cm²/s, 505 nm, 10 sec). **A**: 40X single-plane confocal image showing PKC α positive Mbs (green) in a vertical cryostat section. **B**: S-nitrosocysteine immunolabel (magenta) in the same region as in **A**. At this light intensity, S-nitrosocysteine immunolabeling pattern is restricted to the inner retina, primarily the IPL and GCL. **C**: Merged images of **A** and **B** showing colocalization of S-nitrosocysteine + and PKC α + cellular structures within the IPL. **D**: Enlargement of the Mb terminal region located within the dashed box in **A**. **E**: Enlargement of the outlined selection in **B** that corresponds to the same region as the terminal outlined in **A** and enlarged in **D**. **F**: Enlargement of the merged image of the exact same regions as presented in **D** and **E**. Note the colocalization of the PKC α + Mb terminal with the S-nitrosocysteine immunolabel as a result of rod saturating mesopic light stimulation. For panels **G-I**, a dark-adapted goldfish retina was stimulated with bright scotopic light (2.4×10^8 photons/cm²/s, 505 nm, 500 msec). **G**: 40X single-plane confocal image showing PKC α positive Mbs (green) in a vertical cryostat section. **H**: The same region as presented in **G**, immunolabeled for S-nitrosocysteine (magenta). Although limited and nearly absent in most of the retinal layers, the SNI appears to be restricted to the innermost region of the IPL and some within the GCL. **I**: Merged image of **G** and **H** showing colocalization of PKC α + Mb terminal structures with S-nitrosocysteine immunolabel. **J**: Enlarged image of the area outlined by the dashed line box in **G** focused on the PKC α + Mb terminal. **K**: Enlargement of the S-nitrosocysteine+ structures within the same terminal region presented in **J**. **L**: Merged image of **J** and **K** showing precise colocalization of a PKC α + Mb terminal with an S-nitrosocysteine + cellular structure in the same optical plane. Scale bars: **C**, **I**=20 μ m; **F**, **L**=10 μ m.

SNI appears to localize to the plasma membrane of the Mb terminals. Intensity profiles of both the PKC α and the SNI revealed that 67.8 ± 3.5 % of the SNI within the IPL was located within the region associated with the Mb terminals (n=9 sections from 4 retinas). Furthermore, colocalization analysis of PKC α and S-nitrosocysteine immunolabeling within individual Mb terminals revealed that 67.2 ± 11.9 % of green pixels (PKC α) overlapped with magenta pixels (SNI) and that 75.0 ± 9.9 % of magenta pixels overlapped with green pixels (data not shown, n=10 terminals).

Recently, we reported a functional aspect of retinal S-nitrosylation responsible for mediating the modulation of bipolar cell light responses in the goldfish retina; Mb light responses to dim, rod mediated input were enhanced via S-nitrosylation upon exposure to illumination with intensity of at least 2.4×10^8 photons/cm²/s for 500 ms (Tooker et al., 2013). Accordingly, we reduced the intensity of the stimulus to a bright scotopic light step (2.4×10^8 photons/cm²/s, 505 nm, 500 ms). In the goldfish this bright scotopic light nearly fully activates rods, and the subsequent elements of the rod pathways, without reaching the threshold of cone activation (Joselevitch and Kamermans, 2009). After a 500 ms exposure to 2.4×10^8 photons/cm²/s, SNI was nearly fully confined to the inner retina (Fig. 2.3H and I) and the IPL was the only layer to show a significant increase in SNI compared to basal levels in the dark-adapted retina ($p=0.01$, unpaired Student's *t* test, $n=10$ sections from 4 retinas). Importantly, $80.0 \pm 2.7\%$ of the SNI found within the IPL was restricted to the portion containing the Mb terminals. SNI was found to colocalize with structures defined by PKC α immunofluorescence (Fig. 2.3G, H and I, boxed area). Analysis of individual Mb terminals revealed that $61.5 \pm 17.4\%$ of green pixels overlapped magenta pixels and $82.1 \pm 14.4\%$ of magenta pixels overlapped with green pixels ($n=10$ terminals). Within the IPL, analysis by one-way ANOVA revealed a significant difference between fully light-adapted retinas, retinas stimulated with rod saturating mesopic light and bright scotopic light ($p<0.0001$, one-way ANOVA). Post hoc comparisons using Tukey's multiple comparison test indicated that the mean intensity of SNI in the IPL was significantly higher in light-adapted retinas (50.2 ± 5.3) than in retinas stimulated with 1×10^{10} photons/cm²/s (23.5 ± 1.8) and both were significantly elevated over the SNI in retinas stimulated with 2.4×10^8 photons/cm²/s (9 ± 1.3). Furthermore, the average percentage of SNI that was associated with Mb terminals was significantly greater in retinas stimulated with 2.4×10^8

photons/cm²/s than in those stimulated with 1x10¹⁰ photons/cm²/s (p=0.01, unpaired Student's *t* test). In the GCL, analysis by one-way ANOVA indicated a significant difference between light stimulation paradigms. Tukey's multiple comparison test revealed a significant reduction in the mean SNI when the retina was stimulated with 2.4x10⁸ photons/cm²/s (9.9 ± 1.4) as compared to light-adapted (33.7 ± 4.8) and 1x10¹⁰ photons/cm²/s stimulated retinas (30.8 ± 3.8). No significant difference was detected between the mean SNI in the GCL of light-adapted or 1x10¹⁰ photons/cm²/s stimulated retinas. Importantly, when we increased the stimulus duration of the bright scotopic flash to 10 s, matching the duration of the mesopic flash, we did not observe any significant difference in the SNI labeling pattern when compared to the 500 ms flash (data not shown).

Next, we addressed the question of whether the extent of S-nitrosylation is regulated in a light intensity dependent manner in the mammalian retina. To this end, we subjected wild-type mouse retinas to the exact same light stimulation paradigm as was applied to the goldfish retinas and then assessed overall retinal S-nitrosylation through S-nitrosocysteine immunofluorescence. Wild-type mouse retinas stimulated with 1x10¹⁰ photons/cm²/s (505 nm, 10 s), a mesopic light stimulus which surpasses the activation threshold for cones (~10¹⁰ photons/cm²/s) and approaches rod saturation (~10¹¹ photons/cm²/s, Busskamp et al., 2010), displayed an SNI labeling pattern that was primarily restricted to the inner retina (Fig. 2.4B and C). This labeling pattern in the mammalian retina was strikingly similar to the pattern of SNI in goldfish that was evoked by the exact same flash. Compared to baseline levels of SNI in the dark-adapted mouse retina (Fig. 2.2E), the 1x10¹⁰ photons/cm²/s flash evoked significantly more SNI in the inner retina: INL p=0.003, IPL p=0.001 and GCL p<0.0001(unpaired Student's *t* test, n=11 sections from 6 retinas). Additionally, SNI appeared to colocalize with the RBC terminal clusters

(marked by PKC α immunofluorescence) in the IPL (Fig. 2.4D, E and F). Intensity analysis within the IPL revealed that $68.0 \pm 3.7\%$ of the SNI was restricted to the region of the IPL that contained the terminals of RBCs. Systematic analysis of RBC terminal clusters indicated that $48.3 \pm 12.6\%$ of green pixels overlapped with magenta and $78.8 \pm 6.3\%$ of magenta pixels overlapped with green (n=10 terminal regions), indicating a majority of colocalization between the two individual patterns of immunofluorescence.

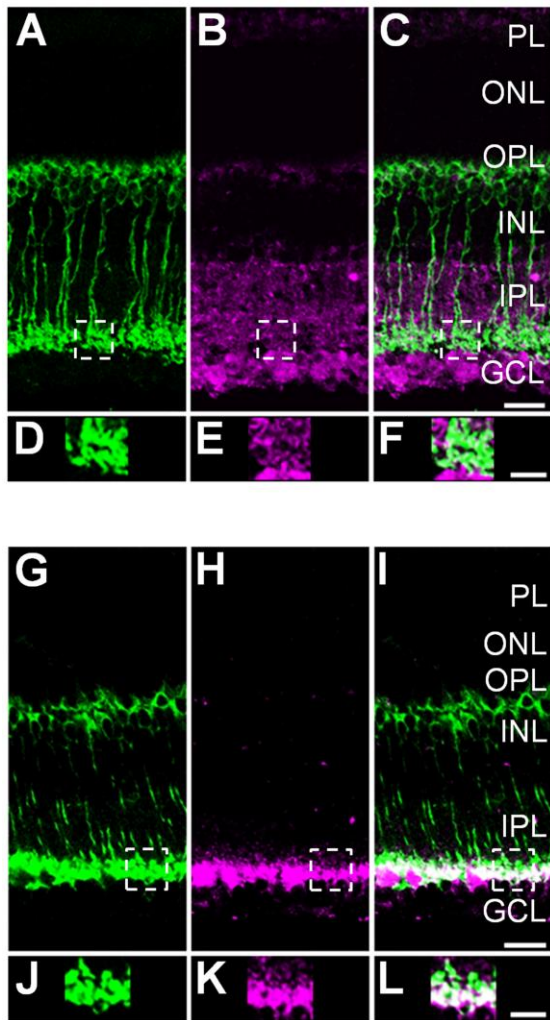


Figure 2.4. Light intensity determines the S-nitrosocysteine immunofluorescence labeling pattern in the wild-type mouse retina. For panels **A-F**, a dark-adapted wild-type mouse retina was stimulated with mesopic light (1×10^{10} photons/cm²/s, 505 nm, 10 sec). **A**: 40X single-plane confocal image showing PKC α positive RBCs (green) in a vertical cryostat retinal section. **B**: Confocal image of the S-nitrosocysteine immunolabel (magenta) in the same retinal region as illustrated in **A**. Stimulation with mesopic light restricted the S-nitrosocysteine immunolabeling pattern to the inner retina. **C**: Merged images of **A** and **B** showing colocalization of S-nitrosocysteine + and PKC α + cellular structures within the IPL. **D**: Enlargement of the RBC terminal region located within the dashed box in **A**. **E**: Enlargement of the outlined selection in **B** that corresponds to the SNI in the same region as the terminal outlined in **A** and enlarged in **D**. **F**: Enlargement of the merged image of the exact same regions as presented in **D** and **E**. Note the colocalization of the PKC α + RBC terminal structures with the S-nitrosocysteine immunolabel as a result of mesopic light stimulation. For panels **G-I**, a dark-adapted wild-type mouse retina was stimulated with bright scotopic light (2.4×10^8 photons/cm²/s, 505 nm, 500 msec). **G**: 40X single-plane confocal image showing PKC α positive RBCs (green) in a vertical cryostat section. **H**: The same region as presented in **G**, immunolabeled for S-nitrosocysteine. Scotopic light stimulation of the wild-type mouse retina appears to restrict the SNI to the innermost region of the IPL and some within the GCL. **I**: Merged image of **G** and **H** showing colocalization of PKC α + RBC terminal structures with S-nitrosocysteine immunolabel. **J**: Enlarged image of the area outlined by the dashed line box in **G** focused on the PKC α + RBC terminals. **K**: Enlargement of the S-nitrosocysteine + structures within the same terminal region presented in **J**. **L**: Merged image of **J** and **K** showing colocalization of PKC α + RBC terminal cluster with a S-nitrosocysteine + immunolabel in the same optical plane. Scale bars: **C**, **I**=20 μ m; **F**, **L**=10 μ m.

When the intensity of light stimulation was reduced to a bright scotopic flash (2.4×10^8 photons/cm²/s, 505 nm, 500ms), the pattern of S-nitrosocysteine immunofluorescence was localized primarily in the inner retina (Fig. 2.4H and I). Interestingly, the bright scotopic flash significantly elevated SNI intensity, above baseline dark-adapted levels, in the IPL and in the GCL ($p < 0.0001$, $p = 0.003$ respectively, unpaired Student's *t* test, $n = 7$ sections from 3 retinas). Within the IPL, $81.8 \pm 2.7\%$ of the SNI label was associated with the RBC terminal region of the IPL which was significantly more than the average percentage of SNI label within the terminal region of retinas stimulated with mesopic light stimulation ($p = 0.03$, unpaired Student's *t* test). Both light flashes evoked SNI label that was restricted to the inner retina. However, by comparison, the brighter intensity light stimulation (1×10^{10} photons/cm²/s) induced a greater distribution of SNI in the inner retina as there was significantly more SNI label in the INL as compared to the dim light intensity (2.4×10^8 photons/cm²/s; $p = 0.009$ unpaired Student's *t* test). In line with these results, analysis of individual terminal regions ($n = 10$) from retinas stimulated with bright scotopic light revealed a colocalization pattern similar to retinas stimulated with mesopic light: $38.2 \pm 13.6\%$ of green pixels overlapped with red, while $80.5 \pm 16.3\%$ of magenta pixels overlapped with green (Fig. 2.4J, K and L).

We compared the fluorescent intensity within the IPL and GCL across the three various light stimulated states (i.e. photopic, mesopic, bright scotopic). One-way ANOVA revealed a significant difference in the SNI intensity within the IPL between light-adapted retinas, mesopic light stimulated retinas, and scotopic light stimulated retinas ($p < 0.0001$). Interestingly, the difference was a result of a significant increase in the mean SNI of the light-adapted retina (51.5 ± 4.8) as compared to both the mesopic (21.7 ± 3.1) and the bright scotopic light stimulated retinas (16.0 ± 2.1 , Tukey's multiple comparison test). Although the mean SNI intensity within

the IPL evoked by 1×10^{10} photons/cm²/s was greater than the mean intensity evoked by 2.4×10^8 photons/cm²/s, the difference was not significant (Tukey's multiple comparison test). Within the GCL, a significant difference was detected in SNI intensity across light-adapted retinas, retinas stimulated with a single mesopic step and retinas stimulated with a single scotopic step of light ($p < 0.0001$, one-way ANOVA). Similar to our observation in the IPL of the mouse retinas, Tukey's multiple comparison test indicated that the difference was due to the significant increase of SNI intensity within the GCL of the light-adapted retina (47.3 ± 4.1) as compared to retinas stimulated with either 1×10^{10} photons/cm²/s (24.3 ± 2.4) or 2.4×10^8 photons/cm²/s (17.0 ± 4.1). Again, although there was a greater level of SNI intensity measured in the GCL of retinas stimulated with mesopic light flash, it was not significantly larger than the SNI intensity measured in retinas stimulated with scotopic light stimuli.

Together, these data strongly support the notion that the overall intensity of SNI is positively correlated with the illumination levels in both the goldfish and mouse retina. Furthermore, the reported pattern of SNI is consistent with observations that NO levels in the retina increase in a manner dependent upon intensity of a light stimulus (Sekaran et al., 2005). This increase of NO is primarily mediated by nNOS, which, in general, is localized primarily to the inner retina in a variety of vertebrates, including goldfish and mouse (Eldred and Blute, 2005; Giove et al., 2009, Pang et al., 2010b; Walter et al., 2014; Zhu et al., 2014).

Light-Evoked S-nitrosocysteine Immunofluorescence is Occluded by Pre-treatment with NEM

To further test our finding that light stimulation evoked increased S-nitrosylation within the fish and mouse retina, we inhibited the formation of nitrosocysteine prior to the evoked release of NO. Dark-adapted eyecups were incubated in NEM (1 mM) which irreversibly binds

to free sulfhydryl groups (Smyth et al., 1960), blocking them from interacting with NO and thereby preventing the formation of S-nitrosothiols (Hu et al., 2012). In this regard, the pre-incubation with NEM prevents the formation of *new* S-nitrosocysteines which would be created by the light-evoked release of NO. After the incubation in NEM, goldfish and mouse retinas were stimulated for 10 s with mesopic green light (1×10^{10} photons/cm²/s) as this light intensity evoked a significant increase in SNI (compared to dark-adapted retinas) across multiple retinal layers in both animal models.

In the goldfish retina, the amount of SNI induced by a mesopic light flash was drastically reduced as compared to control conditions (Fig. 2.5B and C). By comparison, every retinal layer showed significantly less intense light-evoked SNI labeling in the NEM treated retina compared to the control: PL: $p=0.01$, ONL: $p=0.03$, OPL: $p=0.008$, INL: $p=0.002$, IPL: $p<0.0001$, GCL: $p=0.0002$ (unpaired Student's *t* test, control: $n=9$ sections from 4 retinas, NEM: $n=7$ sections from 2 retinas). Furthermore, compared to the baseline level of SNI in the dark-adapted goldfish retina, NEM prevented a significant light-evoked increase in all retinal layers and, in fact, induced a significant *decrease* in the amount of SNI within the GCL ($p=0.04$, unpaired Student's *t* test). The SNI labeling that is observed in the NEM-treated goldfish retina is most likely due to S-nitrosylation that was present prior to the application and incubation in NEM.

In the mouse retina, under control conditions, a 10 s exposure to mesopic green light at 1×10^{10} photons/cm²/s induced significantly increased levels of SNI in the INL, IPL and GCL. However, after incubation in NEM, the same illumination failed to induce elevated SNI (Fig. 2.5E and F). In other words, when compared to the levels of SNI evoked in the INL, IPL and GCL by mesopic stimulation under control conditions, incubation in NEM resulted in a significant reduction (INL: $p=0.005$ IPL: $p=0.0004$, GCL: $p<0.0001$, unpaired Student's *t* test,

control: n=11 sections from 6 retinas, NEM: n=7 sections from 3 retinas). Furthermore, mesopic light stimulation evoked SNI in the presence of NEM was not measurably different from that in the dark-adapted mouse retina.

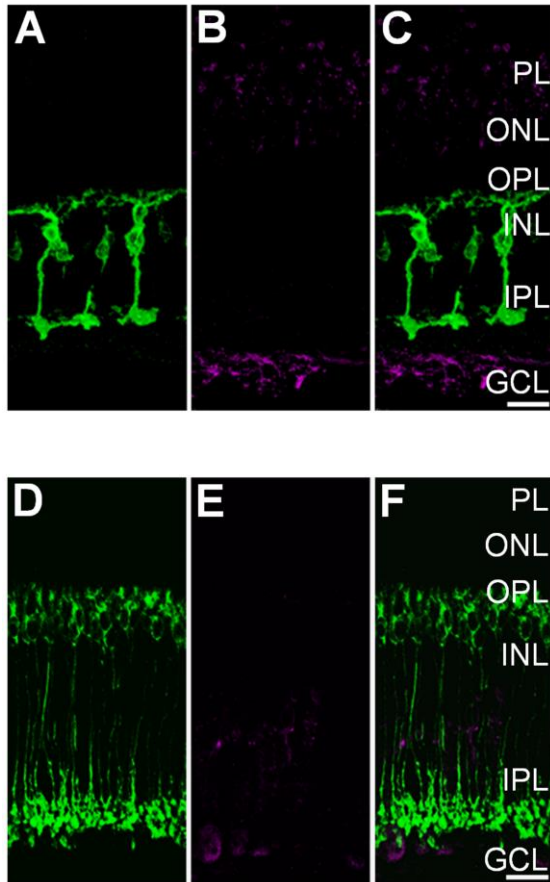


Figure 2.5. Light-evoked S-nitrosylation in the goldfish and wild-type mouse retina is prevented by pre-incubation with N-Ethylmaleimide (NEM). **A:** Single plane 40X confocal image showing PKC α + (green) Mbs in a vertical cryosection from a goldfish retina incubated in 1 mM NEM for 20 min prior to mesopic light stimulation (1×10^{10} photons/cm 2 /s, 505 nm, 10 sec). **B:** Same region as in **A** showing S-nitrosocysteine immunolabeling (magenta) in response to mesopic light stimulation. Note absence of immunolabel signal when compared to the untreated goldfish retina seen in **Fig. 2.3A, B,** and **C.** **C:** Merged image of confocal images from **A** and **B** showing very little colocalization between PKC α + Mbs and S-nitrosocysteine immunofluorescence. **D:** Single plane 40X confocal image showing PKC α + (green) RBCs in a vertical cryosection from a wild-type mouse retina incubated in 1 mM NEM for 20 min prior to mesopic light stimulation (1×10^{10} photons/cm 2 /s, 505 nm, 10 sec). **E:** Confocal image of the same region as presented in **A** illustrating that the mesopic light-evoked SNI (magenta) is dramatically reduced as compared to the untreated wild-type mouse retina (**Fig. 2.4A, B,** and **C).** **F:** Merged 40X confocal imaged of a wild-type mouse retina co-immunolabeled for PKC α and S-nitrosocysteine. Scale bars=20 μ m.

Activation of nNOS is Required for Light Dependent S-nitrosylation in the Retina

In the vertebrate retina, the pattern of light-evoked NO release is intimately connected to the expression of nNOS (Eldred and Blute, 2005; Giove et al., 2009; Walter et al., 2014), and although all three NOS isoforms have been discovered in the retina, nNOS is thought to be the major source for light-evoked NO during visual responses (Vielma et al., 2012). Therefore, the light driven S-nitrosylation we observed is most likely a result of light-evoked synthesis and release of NO via nNOS positive neurons that are mostly localized to the inner retina (Eldred and

Blute, 2005; Giove et al., 2009, Pang et al., 2010b; Walter et al., 2014). To assess the relative contribution of nNOS to the light-evoked increase in SNI that we observed after a mesopic light flash, we incubated goldfish and mouse retinas in TRIM (50 μ M), a potent inhibitor of nNOS (Handy et al., 1996).

After pre-incubation with TRIM, a 10 s light flash at intensity of 1×10^{10} photons/cm²/s failed to induce SNI at levels that were greater than baseline dark-adapted conditions in the goldfish retina (Fig. 2.6B and C; n=6 sections from 2 retinas). In fact, we obtained a similar result after incubating the goldfish retina in TRIM as when the retina was incubated in NEM prior to light stimulation: there was no significant difference in SNI intensity across all layers except for the GCL which showed a 4 fold decrease in SNI intensity, which proved to be significant compared to SNI intensity levels in the dark-adapted control ($p=0.02$, unpaired Student's *t* test). Compared to the goldfish retina which was stimulated with the same rod saturating light flash under control conditions (Fig. 2.3, top panel), the TRIM treatment significantly reduced SNI intensity in all retinal layers: PL: $p=0.01$, ONL: $p=0.03$, OPL: $p=0.009$, INL: $p=0.002$, IPL: $p<0.0001$, GCL: $p=0.0002$ (unpaired Student's *t* test, control: n=9 sections from 4 retinas, TRIM: n=6 sections from 2 retinas). These results were consistent with the finding that, in the goldfish retina, nNOS immunoreactivity is found in nearly all retinal layers (Liepe et al., 1994). Note that TRIM also inhibits inducible NOS (iNOS) (Handy et al., 1996). Unlike its constitutively active counterparts, iNOS expression is only elevated in the retina under pathological conditions (Knowles and Moncada, 1994) or after intense, prolonged illumination (i.e. 8 hrs, 1,200-1,400 Lux, 490-580 nm, Palamalai et al., 2006). It is highly unlikely that our 10 s light flash at intensity 1×10^{10} photons/cm²/s would stimulate iNOS expression and subsequent NO release. However, note the weak SNI present in both the

photoreceptors as well as in GCL in the presence of TRIM that might be resulted by the endothelial NOS (eNOS) activity that has been shown to localize to the outer and inner retina (Haverkamp et al., 1999).

In the mouse retina, TRIM significantly disrupted the pattern of SNI observed under control conditions after the mesopic light exposure (1×10^{10} photons/cm²/s; Fig. 2.6E and F; n=9 sections from 3 retinas). In the presence of TRIM the light stimulation did not significantly elevate the intensity of SNI above dark-adapted baseline levels in any retinal layer except for the GCL (p=0.03; unpaired Student's *t* test, dark-adapted: n=7 sections from 6 retinas, TRIM: n=9 sections from 3 retinas). When compared side-by-side with retinas that were incubated in Ames' media only, the TRIM incubation significantly reduced the amount of SNI that was evoked by mesopic light flash. Under control conditions, a robust SNI labeling pattern was observed in the INL, IPL and GCL (Compare

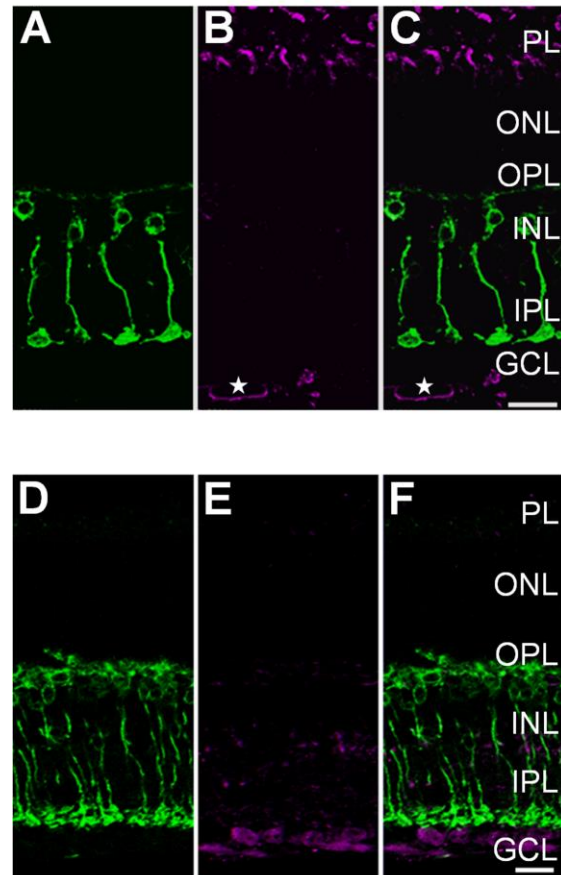


Figure 2.6. Light-evoked S-nitrosylation in the adult retina requires nNOS activation. **A:** Single plane 40X confocal image showing PKC α + (green) Mbs in a vertical cryosection from a goldfish retina incubated in 50 μ M TRIM for 30 min prior to mesopic light stimulation (1×10^{10} photons/cm²/s, 505 nm, 10 sec). **B:** Immunolabeling, of the same region as in **A**, for S-nitrosocysteine (magenta). Compared to the S-nitrosocysteine immunolabeling pattern in the untreated goldfish retina (**Fig. 2.3A, B, and C**), pre-incubation with TRIM resulted in dramatically less light-driven SNI. The SNI below the GCL appears to label a structure with morphology that is consistent with a blood vessel (star). **C:** Merged confocal image depicting co-immunolabeling of PKC α and S-nitrosocysteine with minimal colocalization. **D:** Single plane 40X confocal image showing PKC α + (green) RBCs in a vertical cryosection from a wild-type mouse retina incubated in 50 μ M TRIM for 30 min prior to mesopic light stimulation (1×10^{10} photons/cm²/s, 505 nm, 10 sec). **E:** S-nitrosocysteine immunolabeling (magenta) in the same region as presented in **D**. Notice the drastic reduction in SNI compared to that in the untreated mouse retina in **Fig. 2.4A, B, and C**. **F:** Merged image of the PKC α immunolabel from **D** and the S-nitrosocysteine immunolabel from **E**. Scale bars=20 μ m.

Fig. 2.6E and F with Fig. 2.4B and C). After incubation in TRIM, SNI was significantly reduced in the INL, IPL and GCL ($p=0.005$, $p<0.0001$, $p<0.0001$, respectively; unpaired Student's *t* test, control: $n=11$ sections from 6 retinas, TRIM: $n=9$ sections from 3 retinas). These data are consistent with the notion that the light stimulation is evoking nNOS dependent-NO release which drives SNI in the INL, IPL and GCL as was observed under the control conditions and further prevented with the incubation in TRIM.

While it was not significantly greater as compared to the dark control, there is still obvious SNI labeling after incubation with TRIM, particularly in the PL and the GCL in both the goldfish and mouse retinas. These results are consistent with the previous reports that some S-nitrosylation is observed in the presence of NOS inhibitors, indicating a basal, stable level of nitrosylation (Hess et al., 2005). Additionally, it is highly probable that this S-nitrosylation labeling pattern is due to NO release from endothelial NOS (eNOS), independent of the light stimulation. Note the S-nitrosocysteine labeling pattern beneath the GCL resembling the morphology of a blood vessel (Fig. 2.6B and C, star), an observation consistent with the general consensus that eNOS is considered to be expressed in high levels within the vascular endothelium (Knowles and Moncada, 1994).

In order to dissect the role of nNOS in contributing to light dependent S-nitrosylation in the mammalian retina, we examined the S-nitrosocysteine immunoreactivity in light- and dark-adapted retinas from mice lacking the nNOS isoform (nNOS KO). In the light-adapted nNOS KO animal, we observed a dramatic reduction in SNI across all layers of the retina (Fig. 2.7B and C), when compared to light-adapted WT littermates (Fig. 2.7E and F), with the most striking difference being the near lack of labeling in the outer retina. SNI labeling in dark-adapted nNOS KO retinas (Fig. 2.7H and I) was similar to dark-adapted WT littermates (Fig. 2.7K and L).

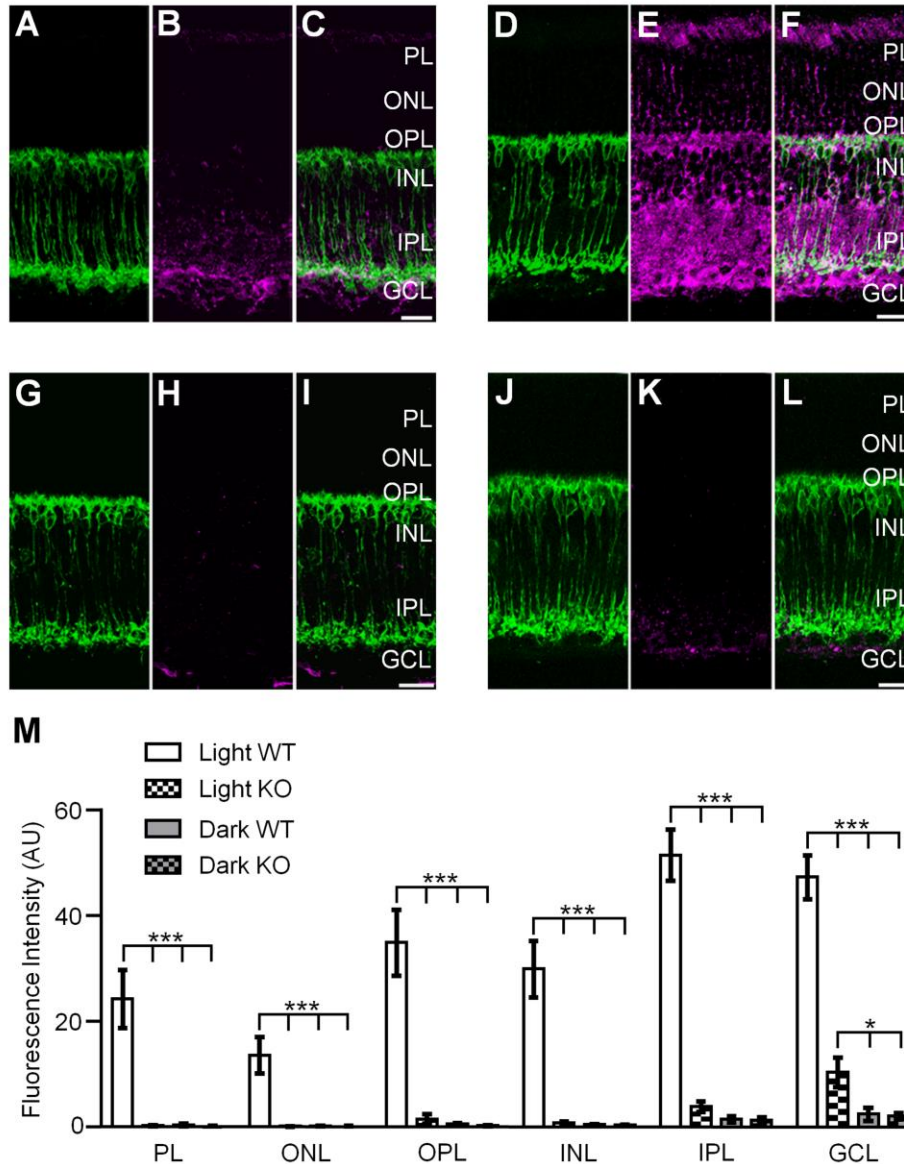


Figure 2.7. nNOS is necessary for robust S-nitrosylation in the mouse retina. 40X vertical cryostat sections of retinas from a light-adapted nNOS KO animal (top left), a light-adapted WT littermate (top right), a dark-adapted nNOS KO animal (bottom left) and a dark-adapted WT littermate (bottom right). **A, D:** RBCs indicated by PKC α + immunolabeling (green) in a light-adapted nNOS KO animal (**A**) and WT littermate (**D**). **B, E:** light-evoked S-nitrosocysteine immunofluorescence (magenta) is reduced and confined to the inner layers of the nNOS KO retina (**B**) as compared to the light-adapted wild-type mouse retina (**E**). **C:** Merged confocal image showing the co-immunolabeling of PKC α and S-nitrosocysteine from **A** and **B**. **F:** Merged image from panels **D** and **E** illustrating robust SNI in the light-adapted WT control retina. **G, J:** PKC α + immunofluorescence of RBCs from dark-adapted nNOS KO (**G**) and WT-littermate (**J**) retinas. SNI is nearly absent across all retinal layers in both the dark-adapted nNOS KO (**H**) and the dark-adapted WT (**K**) animals. **I:** Merged confocal image of panels **G** and **H** showing very little co-immunolabeling of RBCs and SNI in the dark-adapted KO animal. **L:** Merged confocal image of the dark-adapted WT control retina showing very little SNI. **M:** Summary histogram of SNI intensity across all retinal layers in light- and dark-adapted WT and nNOS KO animals. The SNI intensity is significantly reduced in all layers of the light- and dark-adapted nNOS KO retinas as compared to light-adapted WT. The intensity of SNI in the GCL of light-adapted KO animals was significantly higher than the SNI intensity quantified in both the dark-adapted KO and WT. One-way ANOVA with Tukey's multiple comparison test, ***: $p \leq 0.0005$, *: $p = 0.01$, light-adapted KO: $n = 6$ retinas, dark-adapted KO: $n = 2$ retinas, light-adapted WT: $n = 8$ retinas, dark-adapted WT: $n = 6$ retinas. Data is presented as mean \pm SEM. Scale bars = 20 μ m.

In the absence of nNOS, it is readily apparent that light-evoked S-nitrosylation is reduced, but is it, however, entirely absent? In order to address this question we performed a one-way ANOVA comparing the intensity of the fluorescence associated with S-nitrosocysteine in the retinas of light-adapted WT animals, light-adapted nNOS KO animals and dark-adapted nNOS KO animals. The comparison between light- and dark-adapted WT animals was omitted as it had been described and analyzed above (Fig. 2.2G). Analysis via one-way ANOVA revealed a significant difference in SNI in all layers of the retina across the three experimental groups (PL: $p < 0.0001$, ONL: $p = 0.0002$, OPL, INL, IPL and GCL: $p < 0.0001$, Fig. 2.7M). Tukey's multiple comparison test revealed that in every retinal layer, the intensity of the SNI was significantly reduced for both light- and dark-adapted nNOS KO animals as compared to the light-adapted WT retina. Interestingly, in the GCL, the mean intensity of SNI was significantly higher in the light-adapted nNOS KO (10.4 ± 2.8 , $n=9$ sections from 6 retinas) than in the dark-adapted nNOS KO retina (2.02 ± 0.6 , $n=6$ sections from 2 retinas).

Maintaining the assumption that the SNI label that is present in the dark-adapted wild-type retina is a representation of the basal levels of S-nitrosylation, we examined whether the SNI intensity observed in the light-adapted and dark-adapted retinas of nNOS KO animals was different than the SNI intensity in the dark-adapted WT retina. A one-way ANOVA comparison of the individual intensity profiles from light-adapted nNOS KO retinas, dark-adapted nNOS KO retinas, and dark-adapted WT retinas revealed there was a significant difference in the SNI labeling pattern only in the GCL ($p=0.02$, Fig. 2.7M). Tukey's multiple comparison test revealed that in the GCL, the mean SNI intensity was significantly higher in the light-adapted nNOS KO retina (10.4 ± 2.8) compared to both the dark-adapted WT (2.4 ± 1.2) and nNOS KO (2.02 ± 0.6) retinas. In summary, it appears that the lack of nNOS significantly reduces light-evoked S-

nitrosylation in the mammalian retina. However, light-adaptation evoked a small amount of S-nitrosylation (above dark-adapted baseline levels) within the GCL (Fig. 2.7M), which may be a result of light-evoked NO release from other sources. Furthermore, while two alternative forms of nNOS, α and γ , have been shown to be present in the mammalian retina (Giove et al., 2009), the KO animals used in these studies only eliminated expression of nNOS α (Gyurko et al. 2002). Thus even though the nNOS α isoform is considered to be the predominant source of NO release in the retina (Giove et al., 2009), the small, albeit significant, increase in SNI above baseline levels in the GCL of light-adapted nNOS KO animals may be a result of light-evoked NO release from neurons expressing the nNOS γ isoform.

Qualitative Assay of S-nitrosylated Retinal Proteins

Although our immunohistochemical methods provide a qualitative account as to the functional nature of light-dependent S-nitrosylation in the adult retina, they fall short in providing critical information as to the identity of individual proteins being nitrosylated. One of the inherent challenges associated with attempting to identify S-nitrosylated proteins is the fragile, labile nature of the nitrosothiols moiety which can be lost when subjected to reducing conditions (Paige et al., 2008), reduced metal ions such as Cu^+ (Dicks and Williams, 1996), and even to prolonged light exposure (Forrester et al., 2007). For example, using mass spectrometry (MS) an S-nitrosylated protein could be detected by a mass increase of 29 DA on an otherwise unmodified peptide (Lee et al., 2007). Nonetheless, due to the labile nature of the nitrosothiol moiety, S-nitrosylated proteins are rarely detected in MS spectra (Wang et al., 2008). Therefore, with these limitations in mind, we chose to employ a modified version (see Materials and Methods) of the biotin-switch method, originally developed by Jaffrey et al. (2001), as its

reliability and specificity in identification of S-nitrosylated proteins have been well established (Jaffrey et al., 2001; Forrester et al., 2007; Seth and Stamler, 2011). The biotin-switch assay overcomes the issue of S-nitrosocysteine instability by covalently labeling only proteins containing the S-nitrosylation moiety with a biotin in place of the nitrosothiol group. The biotinylated proteins, within the retinal lysates, were enriched by resin-assisted capture before trypsin digestion and MS. Protein sequences are identified by comparison to existing protein databases (see Materials and Methods for details). Due to the limited proteomic databases that are specific to the goldfish proteome, these experiments were performed using only mouse retinas.

Our MS approach revealed 154 proteins that were S-nitrosylated *only* under dark-adapted conditions and 351 S-nitrosylated proteins unique to the light-adapted retina. In general, these results corroborate our immunohistochemical data suggesting that S-nitrosylation is increased in the light-adapted mammalian retina. In order to remain consistent and systematic with our approach used for interpreting our immunohistochemical results, we treated the dark-adapted MS data as providing insight into baseline S-nitrosylated proteins. In other words, we assumed that the constitutive, baseline SNI observed in the dark-adapted mouse retina (Fig. 2.2E and F) was (at least partly) originating from proteins which were determined by MS to be S-nitrosylated only in the dark-adapted retina. Consequently, we focused our attention on the 351 proteins that were identified as unique to the light-adapted retina. A comprehensive list of all the identified proteins can be found in Table 2.2 (Appendix II).

Importantly, we detected several nitrosylated proteins in the mammalian retina that have also been detected and confirmed to be subject of S-nitrosylation, in other systems. For example, we detected channels and transporters such as: Na⁺/K⁺-ATPase, Ca²⁺-ATPase, and cGMP-gated

cation channel ($\alpha 1$); enzymes such as: creatine kinase, protein kinase C, low mw phosphatase, and aldehyde dehydrogenase; redox enzymes such as: thioredoxin and glutathione peroxidase (Stamler et al., 2001; Hess et al., 2005). Due to the importance of information transfer across layers of the retina, proteins that are involved in the mechanism and regulation of exocytosis are particularly noteworthy. Based on our list of putative S-nitrosylated proteins from the light-adapted retina, we identified several proteins which play unique roles in modulating exocytosis. For example, synaptic vesicle glycoprotein, syntaxin-1B, Ras-related protein Rab-3C, excitatory amino acid transporter 1, and protein lin-7 homolog A are all involved in specific aspects of synaptic transmission and are subjected to light evoked S-nitrosylation in the mammalian retina. Syntaxin-1A and B share a conserved primary nitrosylation site at Cys (145) which, upon nitrosylation, alters the quantal size of neurotransmitter release (Palmer et al., 2008). In our experimental design and sample preparation, we did not attempt to isolate proteins with specific subcellular localization as we were not concerned with identifying any particular S-nitrosylated protein. Therefore, this approach may have hindered the identification of particular membrane bound proteins that would require a specific sample preparation for complete extraction. Nonetheless, we were able to identify several proteins known to localize to the membrane (e.g., Na⁺- and Cl⁻-dependent GABA transporter 1&3, excitatory amino acid transporter 1, E3 ubiquitin ligase, and CaM kinase-like vesicle-associated protein). Additionally, our proteomics approach identified the voltage-gated potassium channel subunit Kv 2.1, which is a significant component of the delayed rectifier K⁺ current in neurons (Murakoshi and Trimmer, 1999). In the mouse retina, Kv2.1 has been localized to rod-photoreceptors and horizontal cells (Klumpp et al., 1995; Pinto and Klumpp, 1998), cholinergic and dopaminergic ACs (Tian et al., 2005) in the INL and GCs in the GCL (Pinto and Klumpp, 1998). In the goldfish retina, Kv2.1 was observed

from the ONL to the GCL with confirmed localization to cone inner segments, horizontal cells, Mbs, ACs and GCs (Yazulla and Studholme, 1998). Functionally, reduction of cysteine sulfhydryl groups on the N-terminal domain of Kv2.1, *in vitro*, resulted in sluggish channel gating and prolonged latency to channel opening (Pascual et al., 1997). However, it remains to be determined whether or not S-nitrosylation of retinal Kv2.1 results in a functionally relevant modulation of retinal information processing.

2.5 Discussion

Despite of the large number of proteins that have been identified as potential targets of S-nitrosylation by NO, there is little evidence of S-nitrosylation taking place in neural tissue under physiological conditions. The present immunohistochemical investigation was undertaken to determine if S-nitrosylation, mediated by endogenous NO, takes place under normal, physiologically relevant illumination conditions in the adult goldfish and mouse retina. The use of various light stimulation intensities, pharmacological tools and a transgenic mouse line allowed us to describe the light-dependent nature of S-nitrosylation in vertebrate retinas for the first time. Additionally, our global proteomics approach provided qualitative identification of retinal proteins that are subject to light-dependent S-nitrosylation.

Focal S-nitrosylation Occurs Under Dim, Scotopic Light Conditions in the Retina

Over the past several decades, NO has garnered more and more attention as an important neurochemical signaling molecule responsible for modulating light responses at multiple levels of the retinal circuit. In the vertebrate retina, the synthesis and release of NO is highly coordinated with light stimulation: light stimulation has been shown to significantly increase NO

in the retinas of a number of species including carp (Sekaran et al., 2005), salamander and turtle (Eldred and Blute, 2005), rabbit (Neal et al., 1998) and miniature pig (Donati et al., 1995). Synthesis and release of NO occurs at basal levels in the dark-adapted retina and is elevated in light-adapted retinas (Sekaran et al., 2005; Walter et al., 2014). Of the three NOS isoforms in the retina, the role of the endothelial type (eNOS), in mediating visual responses is unknown (Haverkamp et al., 1999; Tekmen-Clark and Gleason, 2013). The inducible (iNOS) isoform contributes to increased NO synthesis under extremely bright illumination (Palamalai et al., 2006; Piehl et al., 2007) and mediates pathological conditions, possibly through light-dependent protein nitration (Miyagi et al., 2002). Strong evidence suggests that light-evoked NO release under physiological intensities is primarily mediated by the constitutive, calcium-dependent isoform, nNOS (Blute et al., 1997; Blom et al., 2009; Giove et al., 2009). There are some differences in the expression pattern of nNOS across vertebrate species, however, nNOS expressing neurons are mostly localized to the inner retina, sending processes across the IPL in both mouse (Haverkamp and Wassle, 2000; Pang et al., 2010b; Zhu et al., 2014) and goldfish (Villani and Guarnieri, 1996). This is consistent with the fact that in this study, the dimmest illumination (2.4×10^8 photons/cm²/s, 505 nm, for 500 ms) to trigger a detectable increase of SNI, only did so in the IPL and in the GCL in both species (Figs. 2.3 and 2.4). In our hands, lower intensities of illumination produced SNI that was indistinguishable from that seen in fully dark-adapted retinas (data not shown) suggesting that the intensity threshold for producing S-nitrosylation, detectable via immunohistochemistry, is $\sim 2.4 \times 10^8$ photons/cm²/s. This intensity is the same that reliably caused S-nitrosylation dependent modulation of voltage-gated calcium currents (I_{CaS}) in goldfish Mb terminals (Tooker et al., 2013). Although the molecular target of S-nitrosylation that is responsible for I_{Ca} modulation in Mbs has not been identified, it is

noteworthy that in the current study, we found light-evoked SNI clearly outlining the membranes of Mb terminals, among other structures.

As a gaseous, freely diffusible neuromodulator, the instantaneous concentration of NO in retinal tissue is inversely proportional to the distance from the source: when measured $\sim 10 \mu\text{m}$ away from an NO producing GC with an intracellular NO concentration of $\sim 0.2 \mu\text{M}$, the NO concentration dropped to 10 nM (Eldred and Blute, 2005). S-nitrosylation of protein cysteine groups is thought to require more NO than is necessary for the activation of sGC (Ahern et al., 2002), thus, SNI is also expected to be restricted to regions that are in close proximity to NO production at threshold light intensities. Furthermore, some cysteine thiol side-chains have a very high affinity for reacting with NO, based on their surface availability and flanking amino acid sequence (Stamler et al., 1997), adding a level of specificity to S-nitrosylation mediated signaling.

In the mouse retina, the light sensitivity of nNOS expressing (amacrine) cells (ACs) was determined to be $\sim 10^5$ photons/cm²/s (Pang et al., 2010b). These data indicate that nNOS expressing ACs receive rod input. In our hands, light stimulation below the intensity of $\sim 10^8$ photons/cm²/s did not generate SNI in either mouse or goldfish retina. Furthermore, $\sim 10^8$ photons/cm²/s was found to produce NO-mediated functional changes via S-nitrosylation in Mb signaling based on electrophysiological evidence obtained in retinal slice preparation (Tooker et al., 2013). However, on one hand, it is important to point out that both slice electrophysiology and immunohistochemistry may overestimate the light threshold for endogenous S-nitrosocysteine formation: (1) in slice, some NO might quickly diffuse to the bath solution without exerting a measurable effect on the recorded cell; (2) our ability to detect subtle light-evoked increases in S-nitrosocysteine might be limited by the sensitivity of our antibody. On the

other hand, it is also possible that NO production by nNOS+ amacrine cells in the mouse at threshold intensities ($\sim 10^5$ photons/cm²/s) is sufficient to activate the most sensitive NO target, sGC, (activated by nanomoles of NO; Roy et al., 2008), but still be less than the levels required for S-nitrosylation (Ahern et al., 2002). Therefore, the discrepancy between the activation threshold of nNOS+ amacrine cells ($\sim 10^5$ photons/cm²/s) and our observed threshold for SNI ($\sim 10^8$ photons/cm²/s) may be a combinatorial effect of the light intensity-dependent nature of NO synthesis and release (Sekaran et al., 2005) and the relatively high levels of NO needed to form nitrosothiols (as compared to activating sGC, Ahern et al., 2002). To date, neither NO release, nor NO-mediated effects via the sGC pathway have been reported to be triggered in the retina by $\sim 10^5$ photons/cm²/s.

Due to the asymmetric excitatory input resulting in larger OFF excitation of nNOS expressing ACs, maximal NO production is expected to be most profoundly activated by bright, flickering light with frequency of 1-2 Hz (Pang et al., 2010b). We have not tested the effect flickering light stimulation on retinal S-nitrosocysteine formation. Nonetheless, we could not increase SNI further than what was detected in light-adapted retinas (Figs. 2.1 and 2.2) via illumination with 10^{13} photons/cm²/s ($\lambda=505$ nm or 660 nm, for various durations up to 10 min) or by application of the NO donor DETA/NO (1 mM for 1 hour) in either light-adapted or dark-adapted retinas (data not shown). Taking it together, it seems difficult to determine how accurate the threshold value of 10^8 photons/cm²/s might be for endogenous, light-evoked S-nitrosocysteine formation.

NO Modulation of Visual Information Under Physiological and Pathological Conditions

In general, much of the fundamental work describing the effects of NO in the retina focused on the traditional sGC→cGMP-dependent signaling cascade. NO has been shown to influence transmission from cones (Savchenko et al., 1997), as well as the signaling of bipolar cells (BCs; Shiells and Falk, 2002; Snellman and Nawy, 2004). The most notable effect of NO in the retina is the uncoupling of gap junctions between horizontal cells (DeVries and Schwartz, 1989; Lu and McMahon, 1997; Daniels and Baldrige, 2011) and between AII ACs and BCs (Mills and Massey, 1995).

However, evidence has shown that the classical cGMP-dependent pathway is *not* the exclusive route of action for NO and that modulation of cellular function can occur alternatively through S-nitrosylation reactions in the retina. For instance, exogenous NO amplified the a- and b-wave amplitude in rat electroretinograms through a cGMP-independent mechanism (Vielma et al., 2010), and recently, we reported a mechanism in which endogenous NO enhanced the sensitivity of BCs via S-nitrosylation (Tooker et al., 2013). In line with these results is the observation that GCs in nNOS KO mice show a significant deficit in their sensitivity to light stimulation compared to wild-type animals (Wang et al., 2007); however, a mechanism underlying the NO-mediated GC sensitivity was not determined.

Based on the results presented in this study, it appears that S-nitrosylation is a large scale, post-translational modification underlying retinal processes under physiologically relevant light conditions, affecting hundreds of proteins (Table 2.2; Appendix II). However, a global approach such as this most likely underestimates the actual number of retinal proteins undergoing light-dependent S-nitrosylation as it focused on the most abundant S-nitrosylated proteins in the retinal homogenates and used the most conservative proteomics approach to identify them. This

might explain why certain proteins that have been implicated to undergo S-nitrosylation, such as the NR2 subunits of NMDA receptors (Choi et al., 2000) or BK calcium-dependent potassium channels (Bolotina et al., 1994) did not show up in our list of nitrosylated proteins, although they are expressed in the mouse retina (Tanimoto et al., 2012).

It is important to point out, however, that while our immunohistochemical method and global proteomic analysis appears appropriate to detect the presence of S-nitrosylated cysteine groups on certain proteins, the resulted SNI pattern and protein identification has to be treated with caution: it cannot be interpreted as a clear indicator of S-nitrosylation evoked modulation in protein function as S-nitrosylation of any protein might not be associated with structural/functional changes. In fact, only a few examples exist where the S-nitrosylation triggered molecular mechanisms were fully elucidated (Palmer et al., 2008; Choi et al., 2000). Even if S-nitrosylation of a cysteine group does not result in a change in synaptic processing of visual function in every instance, it could serve to buffer the retinal NO and restrict its free diffusion (Wood and Garthwaite, 1994; Eldred and Blute, 2005).

Although we did not specifically direct our proteomics approach to identify a selected set of S-nitrosylated proteins, we observed an interesting set of data that corroborates a previous supposition by Kurenyy et al. (1994) regarding the modulation of rod photoreceptors via NO through a cGMP-independent manner. In their report, Kurenyy et al. (1994) described an increase in a non-voltage-dependent current in rod photoreceptor cells after application of NO donors, and it was proposed that NO may be modulating cGMP channels through S-nitrosylation (Kurenyy et al., 1994). Along these lines, we identified the rod specific cGMP-gated cation channel $\alpha 1$ subunit and $\beta 1$ subunit in our proteomic analysis of proteins that are S-nitrosylated in a light dependent manner (Table 2.2; Appendix II).

S-nitrosylation remains a hallmark characteristic of neurodegenerative diseases in the nervous system (Nakamura et al., 2013) as well as in the retina. When rats were given an intravitreal injection of NMDA and glycine, mimicking excitotoxic conditions often accompanying neurodegenerative diseases, retinal S-nitrosylation dramatically increased and was correlated with GC death (Manabe et al., 2005). In neurodegenerative disease, iNOS can be induced and contribute to the production of toxic levels of NO (Nakamura et al., 2013). Retinal neuronal cell death has been correlated directly to the elevated levels of NO after iNOS activation in Müller cells, under pathological conditions, and apoptosis was significantly reduced in iNOS KO animals (Goureau et al., 1999; Sennlaub et al., 2002). Interestingly, NO induced apoptosis of retinal neurons in a cGMP-*independent* manner, and was instead, attributed to protein nitration (Sennlaub et al., 2002), which is strong evidence implicating aberrant S-nitrosylation as the underlying mechanism.

The results presented here indicate that although aberrant S-nitrosylation may be contributing to neuronal death in certain retinopathies, in the healthy eye, S-nitrosylation can be regulated by physiologically relevant stimuli and may be important in normal visual function, for example, in regulating the sensitivity of GCs via BC output. Importantly, we provided insight into the identification of protein targets susceptible to light-dependent S-nitrosylation. These results provide the framework for further exploration into the functional implications of endogenous S-nitrosylation in modulating visual information processing in the healthy and diseased retina.

3. Nitric Oxide Mediates Activity-Dependent Plasticity of Retinal Bipolar Cell

Output via S-nitrosylation²

3.1 Summary

Coding a wide range of light intensities in natural scenes poses a challenge for the retina: adaptation to bright light should not compromise sensitivity to dim light. Here we report a novel form of activity-dependent synaptic plasticity; specifically, a “weighted potentiation” that selectively increases output of Mb-type bipolar cells in the goldfish retina in response to weak inputs but leaves the input-output ratio for strong stimuli unaffected. In retinal slice preparation, strong depolarization of bipolar terminals significantly lowered the threshold for calcium spike initiation, which originated from a shift in activation of voltage-gated calcium currents (I_{Ca}) to more negative potentials. The process depended upon glutamate-evoked retrograde nitric oxide (NO) signaling as it was eliminated by pretreatment with an NO synthase blocker, TRIM. The NO-dependent I_{Ca} modulation was cGMP independent but could be blocked by N-Ethylmaleimide (NEM), indicating that NO acted via an S-nitrosylation mechanism. Importantly, the NO action resulted in a weighted potentiation of Mb output in response to small (≤ -30 mV) depolarizations. Coincidentally, light flashes with intensity $\geq 2.4 \times 10^8$ photons/cm²/s lowered the latency of scotopic ($\leq 2.4 \times 10^8$ photons/cm²/s) light-evoked calcium spikes in Mb axon terminals in a NEM-sensitive manner, but light responses above cone threshold ($\geq 3.5 \times 10^9$ photons/cm²/s) were unaltered. Under bright scotopic/mesopic conditions, this novel form of Mb output potentiation selectively amplifies dim retinal inputs at Mb \rightarrow ganglion cell synapses. We propose

² Tooker RE, Lipin MY, Leuranguer V, Rozsa E, Bramley JR, Harding JL, Reynolds MM, Vigh J (2013) J Neurosci 33:19176-19193. Reprinted with permission: See Appendix IV.

that this process might counteract decreases in retinal sensitivity during light adaptation by preventing the loss of visual information carried by dim scotopic signals.

3.2 Introduction

The retina codes for contrast, color and motion information of an image projected to the photoreceptor mosaic (Wässle, 2004) under light intensities changing across 10 orders of magnitude (Dowling, 1987; Sterling, 2003). To fit this wide range of inputs to the output limited by the maximal spiking rate of ganglion cells (GCs) ($\sim 10^2$), the retina adapts to the average light intensity (“light adaptation”) as well as to the range of intensities around the mean (“contrast adaptation”) by shifting the dynamic range of coding (Demb, 2002; Rieke and Rudd, 2009). Both light and contrast adaptation are accomplished by implementing various strategies at different stages of retinal processing and on multiple time scales. However, the fundamental challenge for all retinal adaptation processes is similar: prevent saturation of retinal output at high stimulus intensity/contrast while maintaining coding capability for weak inputs.

Contrast adaptation of GC responses is resolved by employing two opposing forms of plasticity in parallel: following high-contrast stimulation, some GC responses were depressed in response to consecutive low-contrast stimuli whereas others were sensitized (Smirnakis et al., 1997; Kim and Rieke, 2001; Baccus and Meister, 2002; Kastner and Baccus, 2011). Besides adaptation processes intrinsic to GCs (Kim and Rieke, 2001; Baccus and Meister, 2002), short-term synaptic plasticity mechanisms that affect bipolar cell (BC) output onto GCs also play a critical role in both adaptation and sensitization during contrast adaptation of GCs (Rieke, 2001; Kastner and Baccus, 2011; Nikolaev et al., 2013). To adapt to changing light intensity and sustain vision across all light conditions, the retina employs a highly sensitive rod pathway for night vision and

a less sensitive cone pathway for daylight vision (Walraven et al., 1990). The light sensitivities of rods and cones overlap, forming a substantial mesopic range that covers behaviorally relevant environmental light intensities for many vertebrates (Krizaj, 2000; Wu, 1994). The dynamic interaction between the rod and cone pathways is influenced by neuromodulators. For example, during light adaptation, dopamine increases signal flow through cone circuits, diminishes that through rod circuits (Witkovsky, 2004) and reduces GC responses to prevent saturation (Hayashida et al., 2009), which ultimately reduces overall retinal sensitivity.

Here we report a novel form of activity-dependent synaptic plasticity in the retina, mediated by retrograde NO signaling. Mbs in the goldfish retina receive and process both rod and cone input (Wong et al., 2005, Joselevitch and Kamermans, 2009). The synaptic plasticity described here results in selective, weighted potentiation of Mb output in response to weak rod- but not cone-mediated inputs. We propose that this new form of NO-mediated, activity-dependent synaptic plasticity plays an important role under bright scotopic and mesopic conditions. Selective enhancement of weak, rod-mediated inputs at the Mb→GC synapses may counteract sensitivity loss during light adaptation, ultimately preventing the loss of visual information carried by low intensity signals. Our results suggest that, similar to contrast adaptation (Kastner and Baccus, 2011), adaptation to increasing luminance also employs opposing forms of plasticity in parallel to extend the dynamic range of retinal signaling.

3.3 Materials and Methods

Retinal Preparations

Retinal slices and isolated bipolar cells were prepared from retinal tissue dissected from adult 4-5" long Goldfish (*Carassius auratus*) of either sex that had been dark-adapted for at least

1 h. Goldfish were kept on a 12 h light/dark schedule. All experimental procedures conformed to the guidelines of the Colorado State University Institutional Animal Care and Use Committee.

Retinal Slice Preparation

Retinal slices (200-250 μm) were prepared as described previously (Palmer et al., 2003). In experiments requiring light stimulation, slice preparation and dissection procedures were performed under infrared illumination as previously described (Vigh et al., 2011). Following the slicing procedure, slices in the recording chamber were moved to an upright microscope (Axioskop 2, Zeiss) and superfused at 2-5 ml/min with Ringer's solution containing (in mM): 100 NaCl, 2.5 KCl, 1.0 MgCl_2 , 2.5 CaCl_2 , 25 NaHCO_3 , 0-0.2 ascorbic acid, and 12 glucose or with bicarbonate buffered Ames' medium (US Biological) supplemented with 1.15 mM CaCl_2 . The pH was set to 7.45 with NaOH. The osmolarity was 260 ± 2 mOsmol for both Ringer's solution and Ames' medium, and both were gassed continuously with 95% O_2 /5% CO_2 . To block inhibitory feedback to Mb terminals, picrotoxin (PTX, 100 μM) was present (Vigh et al., 2005, 2011) in all retinal slice experiments unless otherwise noted. Slices were viewed using a 40 \times water-immersion objective and infrared differential contrast (IR-DIC) and through an IR CCD camera with 2.5 pre-magnification (XC-75, Sony). The camera was connected to a Camera Controller C2741-62 (Hamamatsu) which directed the output to a 19" monitor (Westinghouse). Identification of Mb terminals within the inner plexiform layer was based on the large, bulbous terminal morphology and C_m increase following depolarization (Palmer et al., 2003).

Dissociated Mb Preparation

Solitary bipolar cells were isolated by conventional methods (Tachibana and Kaneko, 1987). Briefly, retinal pieces were dissociated by mechanical trituration with a Pasteur pipette after papain digestion (10 units/ml, Worthington Biochemical). Dissociated cells were plated on

clean glass bottom dishes (MatTek, Ashland, MA) coated with poly-D-lysine and stored at room temperature in low Ca^{2+} (0.2 mM CaCl_2) Ringer's solution containing (in mM): 117 NaCl, 2.6 KCl, 1.0 MgCl_2 , 0.2 CaCl_2 , 10 glucose, 5 HEPES and supplemented with 0.5 mg/ml BSA. The pH 7.45 was set with NaOH; osmolarity was 260 ± 2 mOsmol. Plated cells were viewed using DIC optics through a 40 \times air objective coupled to a 2.5 \times Optovar cube (Axio Observer Z1; Zeiss) and AxioCam HRm CCD camera (Zeiss) and were superfused at 2-5 ml/min with Ringer's solution (see above).

Electrophysiology and Light Stimulation

Whole-cell voltage- and current-clamp recordings were made directly from Mb terminals in both slice and dissociated preparations using a EPC-10 USB patch-clamp amplifier and Patchmaster software (V 2.3; both HEKA) at room temperature during daytime (10 A.M to 6 P.M.). Membrane current and voltage data were filtered at 3 kHz, sampling rates were set at 5 kHz for voltage ramp protocols, 20 kHz for voltage step protocols and 25 kHz for recording spiking membrane potential responses in either current-clamp ramp protocol or using light stimulation. The current-clamp ramp protocol used in these studies stretched from -20 pA to +65 pA over 2 s and was applied relative to the holding current that kept the resting membrane potential at -60 mV. The holding current was determined in voltage-clamp mode when establishing whole-cell mode ("patch break") and was maintained when switching to current-clamp mode using the "Gentle CC-switch" option of Patchmaster. The threshold of current ramp-evoked spikes was determined as follows: The leak was estimated based on the slope of the membrane voltage trace between -100 mV and -60 mV. The leak-subtracted data were normalized to the first (initial) spike amplitude. A current ramp-evoked membrane potential

change was considered a spike if its peak voltage exceeded 2 SD of the baseline noise between -100 mV and -60 mV. The threshold was defined as 5% of the peak membrane voltage for the first spike. Current-voltage relationships were determined by whole-cell voltage-clamp ramps and conventional stepwise reconstructions. The whole-cell voltage-clamp ramp protocol used in these studies was a linear 2 s ramp from -100 to +50 mV. The stepwise I-V protocol consisted of 3 ms steps to potentials (from -80 mV to +60 mV, 10 mV increments) with 5 s between each step. For real-time measurement of membrane capacitance, the Sine+DC technique was used (Gillis, 2000). The capacitive current was measured by the lock-in amplifier following a 1 kHz sinusoidal voltage command (20 mV peak to peak) applied to the holding potential of -60 mV. Patch pipettes of 8-12 M Ω were pulled using a horizontal puller (model p-97, Sutter) from 1.5 mm-diameter thick-walled borosilicate glass (World Precision Instruments) and were coated with dental wax (Cavex) to reduce stray pipette capacitance. For isolation of I_{Ca} in whole-cell voltage-clamp experiments, a Cs-gluconate based internal solution was used (in mM) as follows: 85 Cs-gluconate, 10 phosphocreatine-di(tris) salt, 10 L-ascorbic acid, 10 TEA-Cl, 10 methylamine HCl, 2 EGTA, 3 Mg-ATP, 0.5 Na-GTP, pH of 7.2 (adjusted with CsOH), and osmolarity of 260 \pm 2 mOsmol. For current-clamp (including light-evoked response) recordings, a K-gluconate based internal was used (in mM): 106 K-gluconate, 10 phosphocreatine-di(tris), 3 L-ascorbic acid, 10 KCl, 3 Mg-ATP, 2 EGTA, 0.5 Na-GTP, with pH of 7.2 (adjusted with NaOH), and osmolarity of 260 \pm 2 mOsmol. During experiments using BAPTA, Exo 1, KT5823, or N-Ethylmaleimide (NEM) in the pipette solution, at least 1 min was allowed for intracellular perfusion with the pipette solution before any recording and at least 45 s with standard pipette solution. To keep the osmolarity constant, when 10 mM BAPTA was included in the pipette solution, the amount of Cs-gluconate was reduced accordingly.

In voltage-clamp experiments voltage commands were not corrected for liquid junction potential. Series resistance (R_s) was tightly monitored during recording and was not compensated electronically. Data obtained from Mb terminals were excluded if the uncompensated R_s exceeded 30 M Ω , as in such recordings we found the slope of I_{Ca} activation curve to exceed $1/R_s$ indicating the lack of voltage-clamp (Marty and Neher, 1995). R_s change by 20% any time during the recording also resulted in exclusion of the recording from further evaluation. Recordings with greater than ± 1 mV drift of electrode potential, measured at the beginning and conclusion of the recording, were also excluded. Light stimulation was performed as previously described (Vigh et al., 2011). Briefly, 500-ms-long green ($\lambda=505$ nm), or red ($\lambda=660$ nm) LEDs (American Bright Optoelectronics) were used for full-field illumination of retinal slices. The LED voltage was controlled by the EPC-10 through D/A output. The light intensity was calibrated with an optical meter (model 1918-C, sensor 918D-SL-OD3; Newport).

Drugs and Chemicals

Kainic acid (KA), NBQX, D-(-)-2-amino-5-phosphonopentanoic acid (D-AP5), 1-(2-trifluoromethylphenyl)imidazole (TRIM), 8-bromoguanosine cyclic 3',5'-monophosphate sodium salt (8-Br-cGMP), Exo 1, KT5823 and picrotoxin were obtained from Tocris Bioscience. All other chemicals and salts were obtained from Sigma.

Diethyltriamine-NO/NO (DETA/NO) was synthesized and validated as an NO donor as previously described (Maragos et al., 1991; Hrabie et al., 1993; Damodaran et al., 2012). Briefly, 500 mg of diethyltriamine was added to a thick walled glass reaction vessel equipped with a stir bar. The vessel contained 40 ml of dehydrated acetonitrile dried over 40 nm molecular sieves. The reaction vessel was capped with a gas tight lid and was attached to a custom made NO

reactor. Oxygen was flushed from the reaction vessel using argon purges. Nitric oxide was introduced to the vessel and kept at a pressure of 80 psi for 24 h under stirring conditions. The resulting white DETA/NO precipitate was collected by filtration, washed with acetonitrile and dried under vacuum. The DETA/NO was then validated by a characteristic UV absorbance feature at 252 nm in 0.01 M NaOH with a molar extinction coefficient of $7600 \text{ M}^{-1} \text{ cm}^{-1}$. Direct and real-time NO measurements were performed using GE Analytical Nitric Oxide Analyzer (NOA) equipped with a custom sample cell. A 3 ml aliquot of the media containing DETA/NO was added to the sample cell. The temperature of the sample cell was maintained at 21 °C. Measurements were collected at 5 s intervals at the following instrument operating parameters: cell pressure (1.37 kPa), supply pressure (38.6 kPa) and cooler temperature (-12 °C). The DETA solution was prepared 20 min prior to evaluation. Upon injection into the NOA sample cell, NO release with a steady rate was observed for the duration of the measurement. An average NO release rate of $2.00 \pm 0.19 \text{ nM s}^{-1}$ was measured (n=4). This value corresponds to an average instantaneous concentration of NO of $9.99 \pm 0.93 \text{ nM}$, which matches retinal NO concentrations measured extracellularly 10–20 μm away from relatively strong sources of NO production (Eldred and Blute, 2005). In all of our experiments, the DETA/NO solution (1 mM) was made fresh every day at least 1 h before the experiment began and used for a maximum of 12 h.

Data Analysis

All data was analyzed off-line using IgorPro software (version 5.03; Wavemetrics). Voltage-clamp ramp and stepwise I-V curves were leak-subtracted and normalized to the peak in order to analyze the Ca^{2+} or K^{+} currents. Estimation of the leak current was accomplished using a procedure similar to that reported by Hirasawa and Kaneko (2003). The leak subtraction

procedure consisted of extrapolating the slope of the line between -100 mV and -60 mV. The estimated leak current was subtracted from the raw value providing the “pure” I_{Ca} or I_K .

Normalized, leak subtracted ramp-evoked I_K I-V curves were fit using the following Boltzmann equation:

$$I = 1 / \{1 + \exp[(V - V_{1/2})/S]\},$$

where $V_{1/2}$ is the half activation potential and S is the slope of the voltage dependency (Griguer and Fuchs, 1996). For the step-wise I_{Ca} I-V curve, the first 3 points (-80, -70, -60 mV) were used to estimate the leak current for extrapolation. Leak subtracted step-wise and ramp-evoked I_{Ca} I-V curves were fit using the following modified Boltzmann equation:

$$I = G_{max} \times (V - V_{rev}) / \{1 + \exp[-(V - V_{1/2})/k_G]\},$$

where V_{rev} is the reversal potential, G_{max} is the maximum Ca^{2+} conductance, $V_{1/2}$ is the half-activation potential, and k_G is the slope factor (Leuranguer et al., 2003). Curve fits were done using SigmaPlot (version 11; Systat Software). For ramp evoked I_{Ca} I-V data, analysis of I-V kinetics was also determined directly by using MiniAnalysis software (version 6.0.3;

Synaptosoft). “Activation” ($V_{(5\%)}$) was defined as the voltage at which the resulting current was 5% of the peak current, “half activation” ($V_{(50\%)}$) was defined as the voltage at which the resulting current was halfway between “activation” and the peak current, and “maximum” ($V_{(Max)}$) was defined as the voltage which resulted in the peak current.

Threshold of calcium spikes, in current-clamp ramp protocols, was determined using baseline-subtracted and normalized recordings. A baseline subtraction procedure similar to that used for voltage-clamp was implemented for the current-clamp recordings. Then, the data was normalized to first (initial) spike amplitude. For light-evoked spikes, the latency to first spike was determined by the time point corresponding to the peak of the first evoked spike relative to

the onset of the light stimulus. Where appropriate, depolarization triggered transmitter release was calculated based on the increase in membrane capacitance (C_m jump or ΔC_m) by the equation $\Delta C_m = C_m \text{Response} - C_m \text{Baseline}$ (Vigh and von Gersdorff, 2005). Statistics were calculated using SigmaPlot (version 11; Systat Software), GraphPad Prism (version 6.01), IgorPro software (version 5.03; Wavemetrics) and Excel (Microsoft). Paired or unpaired Student's t tests were used for comparisons between groups; data are presented as mean \pm SEM, with $p < 0.05$ considered a significant difference. For I-V curves and current-clamp ramps, paired Student's t tests were performed on parameters obtained from normalized, leak subtracted pairs of traces unless otherwise noted. For light-evoked spiking responses, paired Student's t tests were performed on latencies determined from original recordings of membrane potentials. One-way ANOVA with Tukey's multiple-comparison test was used for analyzing light-evoked spiking response latencies obtained after sensitizing light stimulations with different intensities.

3.4 Results

Strong Depolarization Shifted Calcium Spike Threshold in Mb-type Bipolar Cells

The classical view by which visual signals are coded by slow, graded potentials in BCs (Werblin and Dowling, 1969) has been challenged by observations in many species: some BCs signal with light evoked sodium spike in ground squirrel (Saszik and De Vries, 2012) and with calcium (Ca^{2+}) spikes in goldfish (Saito et al., 1979), zebrafish (Dreosti et al., 2011; Baden et al., 2011) and mouse (Baden et al., 2013a). However, the role of Ca^{2+} spike-coded, digital signaling by BCs in visual information processing is not fully understood (for review, see Baden et al., 2013b). Voltage-gated Ca^{2+} channels, expressed at the axon terminal region, play a critical role in the spiking light responses of Mb-type BCs in the goldfish retina (Zenisek and Matthews,

1998; Protti et al., 2000); therefore, Ca^{2+} spikes have been proposed to play a role in transmitter release (Zenisek and Matthews, 1998). We made whole-cell current-clamp recordings directly from the large axon terminals of intact Mbs in goldfish retinal slice preparation. With a K^+ -based internal solution in the recording pipette, a current-ramp protocol from -20 pA to +65 pA over 2 s induced membrane potential spikes in Mbs (Fig. 3.1Ai, Aii). The depolarizing current threshold of calcium spike initiation was determined by using baseline-subtracted and normalized recordings (for details, see Materials and Methods) from which the current value, in turn, was used to determine the membrane potential threshold on the original traces. We found that in intact Mbs, the depolarizing current needed to reach the

spike threshold was between 25.5 pA and 59.3 pA, averaging 46.76 ± 5.76 pA, giving the average membrane potential threshold for Ca^{2+} spikes a value of -38.66 ± 5.13 mV ($n=5$) at the axon terminal. These values fell into the range of Ca^{2+} spike threshold for BCs in the zebrafish retina (Baden et al., 2011). Interestingly, when we applied a second current-clamp ramp at least

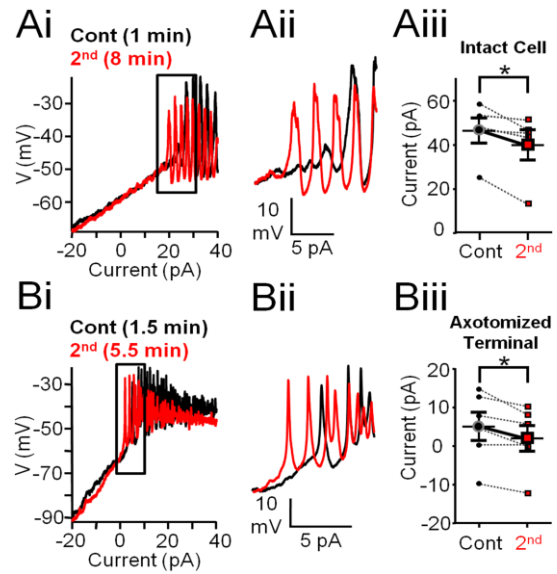


Figure 3.1. Strong depolarization shifted calcium spike threshold in Mb-type bipolar cells. **Ai**, Consecutive current ramp recordings made directly from the large axon terminals of intact Mbs in goldfish retinal slice preparation. Less depolarizing current was needed to evoke spikes when a second current ramp was applied 8 minutes (red) after the first (black). **Aii**, Enlargement of **Ai** focusing on the region of spike initiation. Notice the initiation of spikes is shifted leftward for the 8 min trace. **Aiii**, Summary showing less current required for the initiation of Ca^{2+} spikes in terminals of whole Mbs in response to current ramp when preceded by strong depolarization. Data are taken from leak-subtracted and normalized traces (*: $p=0.03$, paired Student's t test, $n=5$). **Bi**, Current ramp evoked Ca^{2+} spikes recorded from an axotomized Mb terminal in slice preparation. The second current ramp (red: 5.5 min after break-in) triggered spikes with less depolarizing current than the first current ramp (black: 1.5 min after break-in). **Bii**, Enlargement of the regions of spike initiation from **Bi**. Note the leftward shift in the red trace. **Biii**, Summary showing less current is required for the initiation of Ca^{2+} spikes in axotomized Mb terminals in response to current ramp when preceded by strong depolarization. Data are taken from leak-subtracted and normalized traces (*: $p=0.02$, paired Student's t test, $n=5$). Data are presented as mean \pm SEM.

2.5 min after the completion of the first, we found that less depolarizing current (between 13.1 pA and 51.7 pA, averaging 40.24 ± 6.91 pA) was necessary to induce a Ca^{2+} spike (Fig. 3.1Aii). In other words, the membrane potential threshold for Ca^{2+} spike initiation was lower during the second current-ramp (-42.95 ± 5.92 mV) than that during the first (control). Concurrently, the decrease in membrane potential threshold (-4.30 ± 1.46 mV) was significant ($p=0.02$, paired Student's *t* test). Importantly, the holding current (I_{hold}) needed to keep Mbs at -60 mV did not change during the recordings (I_{hold} first ramp): -99.25 ± 31.16 pA vs. I_{hold} second ramp: -99.75 ± 32.98 pA, ΔI_{hold} : -0.5 ± 1.81 pA) indicating that the input resistance was unaltered between consecutive ramps.

Next, we tested if the shift in Ca^{2+} spike threshold was related to the perfusion, over time, of intact cells with complex morphology. In the next set of experiments, we targeted terminals of Mbs whose axon was severed. In concert with their simple morphology, axotomized Mb terminals exhibit a single-exponential membrane time constant and have high input resistance (i.e., “less leaky”) in the absence of dendritic and somatic inputs (Palmer et al., 2003). The data included for processing were obtained from axotomized Mb terminals with I_{hold} recorded at patch-break between -3 pA and -38.5 pA, averaging -24.35 ± 6.16 pA ($n=5$). Consistent with the high input resistance, the depolarizing current threshold during the first ramp for Ca^{2+} spike initiation was much lower (8.06 ± 2.65 pA) than that for intact Mbs. Importantly, during a second ramp, which was delivered with at least 2.5 min delay, Ca^{2+} spikes were triggered earlier in axotomized Mb terminals (Fig. 3.1Bi, Bii) in a similar fashion to that observed in intact Mbs. In other words, a significant reduction in depolarizing current threshold for initiation of Ca^{2+} spikes was seen (4.84 ± 2.07 pA, $p=0.02$, paired Student's *t* test) (Fig. 3.1Biii) without a change in I_{hold} (23.7 ± 6.03 pA) compared to that recorded at patch break (ΔI_{hold} : 0.60 ± 0.15 pA).

Converting the depolarizing current threshold values into membrane potentials, the data showed that in axotomized Mb terminals, the initial Ca^{2+} spike threshold of -44.81 ± 2.37 mV measured during the first ramp dropped to -50.84 ± 3.33 mV during the second ramp and this reduction was statistically significant ($p=0.004$, paired Student's t test). The spike threshold values obtained in axotomized Mb terminals were lower than those obtained from intact Mbs for both the first and second ramps (-44.81 ± 2.37 mV vs. -38.66 ± 5.13 mV, and -50.84 ± 3.33 mV vs. -42.95 ± 5.92 mV, respectively) demonstrating that depolarizing current injections triggered Ca^{2+} spikes more efficiently in axotomized Mb terminals with more compact structure than in intact cells possessing complex morphology. However, when the corresponding spike thresholds were compared (i.e. spike threshold during first ramp in intact cells vs. spike threshold during first ramp in axotomized terminals and thresholds during the second ramps in a similar manner), we found no statistical difference between them ($p=0.3$ and $p=0.2$ for first and second ramp thresholds, respectively, unpaired Student's t test). These results also indicated that the observed reduction of Ca^{2+} spike threshold was independent of any process in the somatodendritic compartment of Mbs and/or the outer retinal circuitry.

Strong Depolarization Induced Modulation of Voltage-Gated Calcium (I_{Ca}) but not Voltage-Gated Potassium (I_{K}) Currents in Mb Terminals

In the next set of experiments, we tested whether the Ca^{2+} spike threshold shift we described above might have been caused by changes in the membrane currents mediating Ca^{2+} spikes. The ionic currents responsible for the spiking response of Mb terminals consist of rapidly activating (Mennerick and Matthews, 1998) voltage-gated influx of Ca^{2+} (I_{Ca}) through L-type voltage-gated Ca^{2+} channels (Heidelberger and Matthews, 1992; von Gersdorff and Matthews,

1996; Tachibana, 1999) that appear to be Cav1.3 type (Logiudice et al., 2006) and subsequent efflux of K⁺, made up by voltage-gated K⁺ (I_K) and big conductance (BK) Ca²⁺-dependent K⁺ (I_{K(Ca)}) currents (Kaneko and Tachibana, 1985; Sakaba et al., 1997; Palmer, 2006).

To study which one of these ionic currents might be responsible for the shift in spike initiation, we performed whole-cell voltage-clamp recordings on axotomized Mb terminals using pairs of consecutive voltage-clamp ramp protocols (from -100 mV to +50 mV, in 2 s) at least 3 min apart. First we isolated I_K using a K⁺ based internal solution (see Materials and Methods) and by complete blockade of I_{Ca} with 100 μM CdCl₂ in the external solution (Fig. 3.2Ai). Blockers of I_{Ca} have been shown to eliminate I_{K(Ca)} in Mbs as well (Kaneko and Tachibana, 1985; Palmer, 2006). Figure 3.2Ai shows a representative recording of I_K traces evoked by consecutive voltage ramps, applied 3 min apart. Holding potentials below -60 mV were excluded from the figure for expansion of the physiologically relevant membrane potential region, although the entire current trace was included in the analysis. Analysis was performed on leak subtracted I_K recordings fit with a Boltzmann function (see Materials and Methods). Once fit, kinetics of the control ramp I-V and second ramp I-V were reflected by the slope factor (S) of the I_K activation and the membrane potential resulting in 50% activation of I_K (V_(1/2)) (Griguer and Fuchs, 1996). No significant difference was found in the slope factors of control ramp I-Vs when compared to those of the second ramp I-Vs (0.66 ± 0.08 mV vs. 0.63 ± 0.09 mV, respectively, Fig. 3.2Aii; paired Student's *t* test, p=0.4, n=5) or between V_(1/2) values (control: -11.42 ± 1.13 mV vs. second ramp I-V: -11.01 ± 1.66 mV; Fig. 3.2Aiii; paired Student's *t* test, p=0.7, n=5).

I_{Ca}, in axotomized Mb terminals, was evoked by applying the same linear ramp protocol used for triggering I_K in voltage-clamp mode, but in the presence of Cs⁺-based internal solution containing TEA-Cl to block I_K and I_{K(Ca)} (Kaneko and Tachibana, 1985). When kinetics of I_{Ca} I-

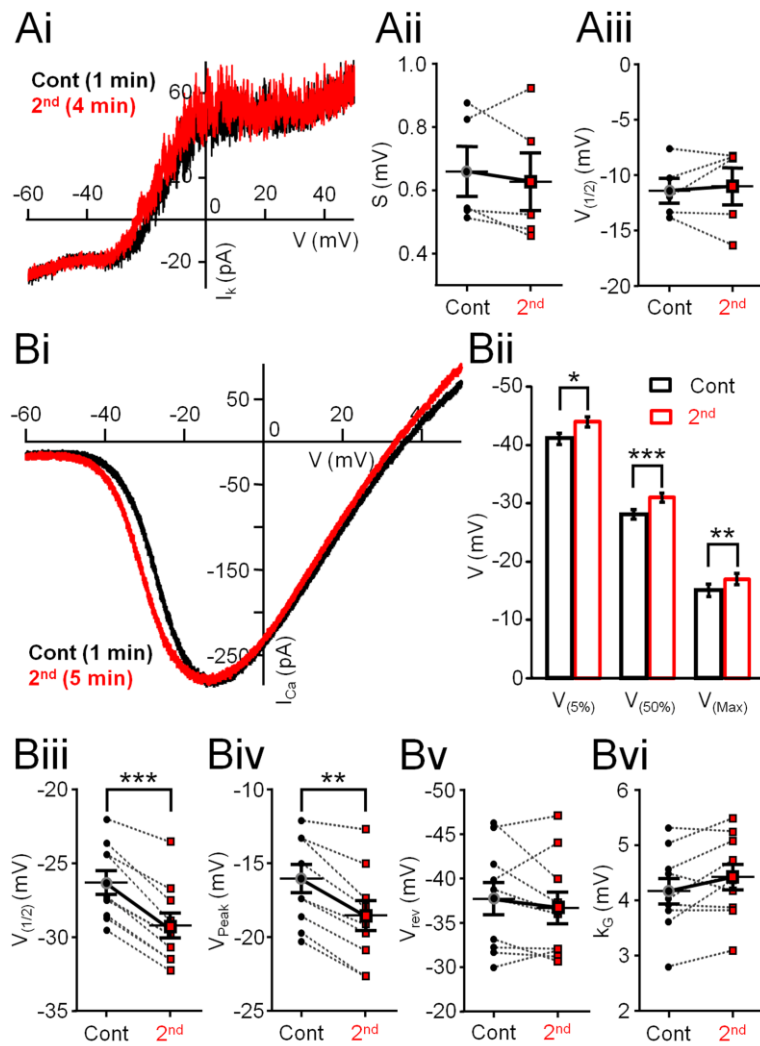


Figure 3.2. Strong depolarization induced modulation of I_{Ca} activation but not I_K kinetics. **Ai**, Potassium current (I_K) in axotomized Mb terminal evoked by a voltage ramp from -100 mV to $+50$ mV for 2 s. Points below -60 mV have been removed for illustration purposes. Black trace is 1 min after break-in and red trace is 4 min after break-in. I_K was isolated by blocking I_{Ca} with $100 \mu\text{M}$ CdCl_2 . The second trace (red) coincides with the control (black). **Aii**, No significant differences were observed between the slope factor (S) of control and second traces. Black circles: control; red squares: second; $n=5$. **Aiii**, The membrane potential at 50% of the maximal current ($V_{(50\%)}$) did not differ in the first and second recordings. Black circles: control; red squares: second; $n=6$. **Bi**, Consecutive I_{Ca} I-Vs generated from an axotomized terminal in slice preparation, in response to a 2 second voltage-ramp. Notice the shift in the trace recorded at 5 minutes after break-in (red) compared to the control trace recorded 1.5 minutes after break-in (black). **Bii**, Summary graph showing I_{Ca} activation ($V_{(5\%)}$), half-activation ($V_{(50\%)}$), and peak ($V_{(max)}$). Black: control; red: second; *: $p=0.00003$, ***: $p=0.000001$, **: $p=0.00001$, paired Student's t test, $n=10$. **Biii**, Summary graph showing half activation ($V_{1/2}$) parameter from Boltzmann fits is significantly less for the second

voltage-ramps when compared to control. Black circles: control; red squares: second; **: $p=0.000002$, paired Student's t test, $n=10$. **Biv**, Summary graph showing significant shift in peak parameter obtained from Boltzmann fits. Black circles: control; red squares: second; **: $p=0.00004$, paired Student's t test, $n=10$. **Bv**, Summary graph of pairwise comparisons displaying no difference in the reversal potential (V_{rev}) parameter obtained from Boltzmann fits. Black circles: control; red squares: second; $p=0.31$, paired Student's t test, $n=10$. **Bvi**, Summary graph showing no significant difference in the slope factor (k_G) parameter obtained from Boltzmann fits for control and second voltage ramps. Black circles: control; red squares: second; $p=0.052$, paired Student's t test, $n=10$. Data are mean \pm SEM.

V traces recorded under these conditions (Fig. 3.2Bi) were evaluated by obtaining measurements of the membrane potential relating to 5%, 50%, and peak I_{Ca} ($V_{(5\%)}$, $V_{(50\%)}$, and $V_{(Max)}$, respectively; see Materials and Methods), we found that on average, $V_{(5\%)}$ was -40.5 ± 0.86 mV, $V_{(50\%)}$ was -27.6 ± 0.80 mV and $V_{(max)}$ was -14.7 ± 1.00 mV for the I_{Ca} I-V curves evoked by the first (control) voltage ramp. These values, obtained in slice preparation, were in perfect agreement with earlier reports studying parameters of I_{Ca} in dissociated, solitary Mbs (Kaneko

and Tachibana, 1985; Heidelberger and Matthews, 1992). However, when we applied an identical second voltage-clamp ramp stimulus with at least 2.5 min delay, a portion of the resulted I_{Ca} did not overlap with that evoked by the first ramp protocol (Fig. 3.2Bi): I_{Ca} triggered by the second ramp activated at more negative membrane potentials. On average, for the second ramp evoked I_{Ca} I-V, $V_{(5\%)}$ was -43.5 ± 0.79 mV, $V_{(50\%)}$ was -30.35 ± 0.75 mV and $V_{(max)}$ was -17.2 ± 0.95 mV (Fig. 3.2Bii). The difference between the first and second ramp I-V parameters was -3.0 ± 0.39 mV for $V_{(5\%)}$, -2.75 ± 0.25 mV for $V_{(50\%)}$, and -2.5 ± 0.31 mV for $V_{(Max)}$, all proven to be statistically significant ($V_{(5\%)}$: $p=0.00003$; $V_{(50\%)}$: $p=0.000001$; $V_{(Max)}$: $p=0.00001$; paired Student's t test, $n=10$) (Fig. 3.2Bii). It is important to note that, once shifted, we found that (1) subsequent ramp I-Vs were insufficient to shift I_{Ca} activation kinetics further to the left and (2) shifted I_{Ca} I-Vs did not return to their initial control values within the timeframe of a recording (up to 20 min), set by $>10\%$ rundown of peak I_{Ca} (data not shown).

I_{Ca} I-V traces evoked by consecutive depolarizing voltage ramps were also analyzed by comparing the parameters of their modified Boltzmann function fits (Leuranguer et al., 2003). We found a difference in half-activation ($V_{(1/2)first}$: -26.34 ± 0.80 mV vs. $V_{(1/2)second}$: -29.24 ± 0.84 mV; Fig. 3.2Biii) and in the peak I_{Ca} ($V_{Peak1st}$: -16.03 ± 0.95 mV vs. $V_{Peak2nd}$: -18.55 ± 1.0 mV; Fig. 3.2Biv); the differences in both parameters were statistically significant ($V_{(1/2)}$: $p=0.000002$; V_{Peak} : $p=0.00004$; paired Student's t test, $n=10$). These results were entirely consistent with the results of analysis based on I-V characteristics obtained directly from the I-V curves. Although the half-activation ($V_{(50\%)}$ vs. $V_{(1/2)}$) and peak I_{Ca} membrane potential ($V_{(Max)}$ vs. V_{Peak}) values for the same I_{Ca} I-V curves obtained by the two methods were not identical, the differences between the corresponding values were not statistically significant ($V_{(50\%)}$ vs. $V_{(1/2)}$ first: $p=0.14$, second: $p=0.16$; $V_{(Max)}$ vs. V_{Peak} first: $p=0.35$, second: $p=0.34$; paired Student's t

test, n=10). There was no significant difference in the reversal potential (V_{rev}) of I_{Ca} between the first (control) and second ramp I-Vs (V_{rev1st} : 37.70 ± 1.84 mV vs. V_{rev2nd} : 36.65 ± 1.78 mV; $p=0.31$; paired Student's t test, n=10; Fig. 3.2Bv), which supported the view that the leftward shift in I_{Ca} activation did not originate from an artifact caused by a drift in electrode potential over the course of our experiments. Although the average slope factor (k_G) slightly increased between the corresponding first (control) and second I_{Ca} I-Vs (k_{Gfirst} : 4.18 ± 0.23 mV vs. $k_{Gsecond}$: 4.44 ± 0.23 mV), this increase was not statistically significant ($p=0.052$, paired Student's t test, n=10). This was consistent with the fact that the slope increased in only 6 of 10 recordings, whereas in the rest of the cases it decreased (3 of 10) or remained the same (1 of 10; Fig. 3.2Bvi). These results suggested that a change in voltage dependence of Ca^{2+} channel gating charges (Hille, 2001) was not a critical mediator of the leftward shift observed in I_{Ca} activation.

The threshold values for Ca^{2+} spikes in axotomized Mb terminals measured with current ramps and I_{Ca} activation ($V_{(5\%)}$) measured with voltage-clamp ramps were in great agreement suggesting that the leftward shift in I_{Ca} activation threshold was responsible for the reduction in Ca^{2+} spike threshold.

Although it was not tested, we considered direct contribution of (BK) $I_{K(Ca)}$ to the shift of Ca^{2+} spike threshold to be highly unlikely: to open (BK) $I_{K(Ca)}$ channels require large membrane depolarization (Vergara et al. 1998; Sah and Davies, 2000) and 10-20 μM $[Ca^{2+}]_i$ in Mb terminals (Sakaba et al., 1997). Thus, (BK) $I_{K(Ca)}$ channels are not active at membrane potentials below I_{Ca} activation.

The Depolarization Induced Shift in I_{Ca} Activation at Mb Terminals was Calcium-Dependent and Required Glutamate-Mediated Synaptic Signaling

Subjecting Mb terminals to 2-s-long depolarizing ramp protocols in retinal slice preparation changed the activation kinetics of I_{Ca} . To explore whether this change was related to the massive influx of Ca^{2+} triggered by these protocols, we generated consecutive I-V curves for I_{Ca} at least 2.5 min apart in a stepwise manner using 3-ms-long square pulse voltage steps between -80 and +60 mV (see Materials and Methods). This stepwise protocol dramatically reduced the total Ca^{2+} influx at the Mb terminal over the course of experiment: between -80 and 40 mV the cumulative step induced Ca^{2+} charge transfer (Q) was only ~0.02% of that triggered by a 2 s ramp (data not shown). In addition, the delay between consecutive short depolarizing steps presumably allowed mobile and fixed Ca^{2+} buffering systems of the Mb terminals (Burrone et al., 2002) to control the spatial and temporal parameters of intracellular Ca^{2+} microdomains (Neher, 1998), formed during each short depolarizing step, at higher efficacy than during a long ramp depolarization. It is important to emphasize that in our whole-cell recordings the standard internal solutions contained 2 mM EGTA (see Materials and Methods), which slightly overestimated the Ca^{2+} buffering capacity of mobile endogenous buffers of Mb terminals (Burrone et al., 2002).

Analysis of parameters obtained from a modified Boltzmann function fit of the data points was used to determine potential differences between the characteristics of consecutive stepwise I-V curves (Fig. 3.3A). On average, the slope factor (k_G) was 5.27 ± 0.29 mV for first (control) and 5.27 ± 0.31 mV for the second stepwise I-V, $V_{(1/2)}$ was -27.80 ± 1.00 mV for first (control) and -28.36 ± 0.95 mV for the second stepwise I-V, and V_{Peak} was -12.27 ± 0.93 mV for control and -12.87 ± 1.11 mV for the second stepwise I-V. No significant difference between the

parameters of control and second stepwise I-V was found (k_G : $p=0.96$; $V_{(1/2)}$: $p=0.27$ and V_{Peak} : $p=0.11$, paired Student's t test, $n=13$). The lack of change in I_{Ca} activation kinetics under these conditions indicated that the negative shift in I_{Ca} activation observed in Mbs in experiments using consecutive depolarizing linear ramp protocols was dependent upon (large) Ca^{2+} influx-mediated intracellular processes, specifically, those processes that could be triggered by ramp protocols but not by short depolarizing steps.

Supporting this notion, when the pipette solution was supplemented with 10 mM BAPTA in place of the regularly used 2 mM EGTA, I_{Ca} I-Vs generated by consecutive voltage-clamp ramp protocols (-100 mV to +50 mV, over 2 s, at least 2.5 min apart) overlapped (Fig. 3.3B). On average, $V_{(5\%)}$ was -39.0 ± 1.75 mV for control and -39.30 ± 1.95 mV for the second ramp I-V, $V_{(50\%)}$ was -23.95 ± 1.09 mV for control and -23.71 ± 2.11 mV for the second ramp I-V, and $V_{(max)}$ was -12.59 ± 1.17 mV for control and -12.18 ± 2.22 mV for the second ramp I-V. Statistical analysis revealed there was no difference between control and second ramp I-V for

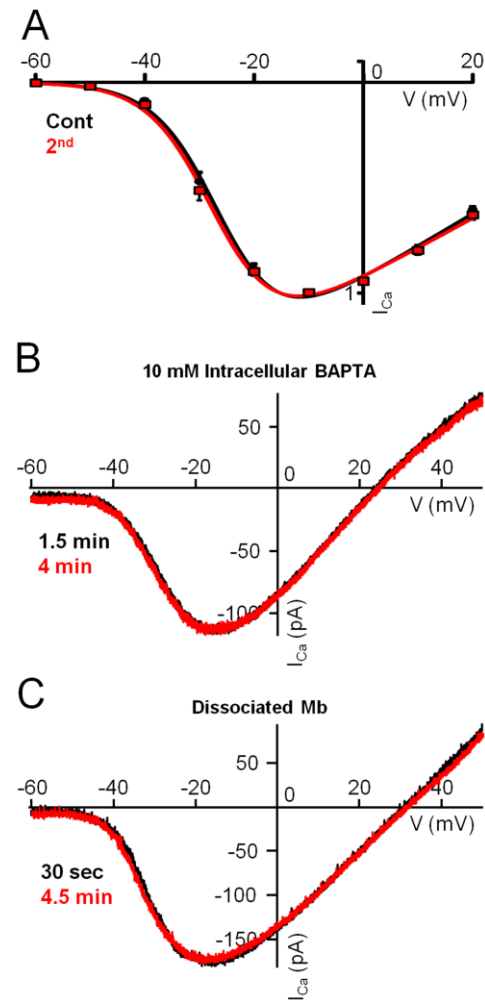


Figure 3.3. Modulation of I_{Ca} at the Mb terminal is Ca^{2+} dependent and required synaptic signaling. **A**, Average (leak subtracted and normalized) stepwise I-V curve from axotomized terminals in slice preparation ($n=13$ for steps to ≤ -10 mV, $n=9$ for steps to 0 mV and +20 mV). Consecutive I-V curves were generated 3 min apart by using 3 ms voltage steps. Data were fit with a modified Boltzmann equation, smooth line (black: first, control I-V; red: second I-V). **B**, Chelation of ramp evoked Ca^{2+} influx using BAPTA (10 mM) inhibited strong depolarization-induced modulation of I_{Ca} kinetics of axotomized terminals in retinal slice preparation. **C**, Consecutive I_{Ca} I-Vs recorded from the axon terminal of an enzymatically dissociated, solitary Mb. The voltage ramp protocol was the same used in slice preparation. No shift was observed between the control (black) and the second (red) I_{Ca} I-Vs.

$V_{(5\%)}$, $V_{(50\%)}$, and $V_{(Max)}$ ($p=0.8$, $p=0.9$, $p=0.8$ respectively, paired Student's t test, $n=5$). Taken together, these results suggested that modulation of I_{Ca} kinetics at the Mb axon terminal required a strong depolarization, resulting in a large influx of Ca^{2+} which initiated a Ca^{2+} -dependent presynaptic process that ultimately lead to modulation of I_{Ca} activation kinetics.

To test whether the I_{Ca} activation shift was indeed solely mediated by intracellular process triggered by the enormous Ca^{2+} influx during long ramp depolarizations, I_{Ca} I-Vs were generated by applying the previously used voltage-clamp ramp protocols (-100 mV to +50 mV, over 2 s, at least 2.5 min apart) to the axon terminals of enzymatically dissociated, solitary Mbs using our standard pipette solution containing 2 mM EGTA. We observed no shift in the I-V curves resulted by consecutive ramps (Fig. 3.3C): we found $V_{(5\%)}$ of -37.7 ± 2.04 mV for control and -37.14 ± 2.26 mV for the second ramp I-V, $V_{(50\%)}$ of -21.93 ± 1.84 mV for control and -22.71 ± 1.95 mV for the second ramp I-V, and $V_{(Max)}$ of -6.14 ± 1.75 mV for control and -8.29 ± 1.78 mV for the second ramp I-V, with no significant difference between control and second ramp I-Vs for $V_{(5\%)}$, $V_{(50\%)}$, and $V_{(Max)}$ ($p=0.6$, $p=0.4$, $p=0.4$ respectively, paired Student's t test, $n=7$). This was in concert with the fact that previous studies of I_{Ca} of cultured solitary Mbs using voltage ramps did not report apparent changes in the I_{Ca} activation (Kaneko and Tachibana, 1985; Heidelberger and Matthews, 1992). Taken together, these results suggested that the pathway that mediated large Ca^{2+} influx-evoked modulation of I_{Ca} kinetics at Mb terminals is likely to have synaptic components driven by the glutamate released from Mb terminals.

To investigate the role of glutamate release from the Mb terminal in I_{Ca} modulation further, we inhibited exocytosis pharmacologically by adding 50 μ M Exo1 (Feng et al., 2003) to the internal solution of the recording pipette. In the presence of Exo1 (50 μ M), the control and second whole-cell voltage-clamp ramp generated I_{Ca} I-Vs overlapped (Fig. 3.4A). With

depolarizing voltage ramps in the presence 50 μ M Exo1, for I_{Ca} we recorded an average $V_{(5\%)}$ of -41.3 ± 1.56 mV for control and -40.94 ± 1.70 mV for the second ramp I-V, $V_{(50\%)}$ of -28.73 ± 1.30 mV for control and -28.10 ± 1.36 mV for the second ramp I-V, and $V_{(Max)}$ of -16.68 ± 1.40 mV for control and -16.57 ± 1.33 mV for the second ramp I-V. Statistical analysis revealed no difference between control and second ramp I-Vs ($V_{(5\%)}$: $p=0.4$; $V_{(50\%)}$: $p=0.4$ and $V_{(Max)}$: $p=0.9$, paired Student's t test, $n=10$). The lack of leftward shift of I_{Ca} activation was consistent with the notion that inhibiting the ramp-evoked glutamate release from Mb terminals prevented the activation of processes responsible for the I_{Ca} modulation. We could not obtain direct evidence for the reduction of glutamate release in these experiments as membrane capacitance measurements triggered by our standard 2 s voltage-clamp ramp were unreliable due to the slowly decaying tail currents (Gillis, 2000) that often lasted for >10 s following the ramps. Nonetheless, in our hands, intracellular perfusion of axotomized Mb terminals with Exo1 (50 μ M) for at least 4 min in slice preparation reduced the control membrane capacitance increase in response to 250

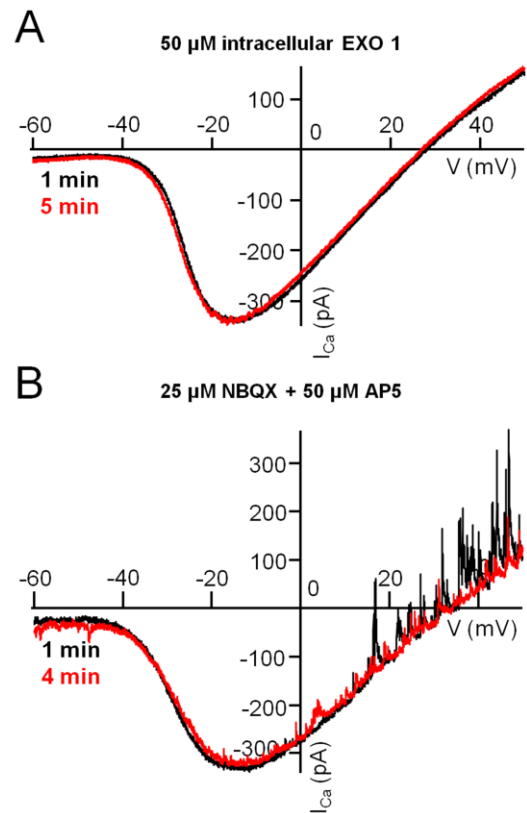


Figure 3.4. Exocytosis of glutamate and activation of neurons postsynaptic to the Mb terminal are required for modulation of I_{Ca} . **A**, Consecutive I_{Ca} traces recorded from an axotomized Mb terminal in slice preparation in response to voltage ramps 4 min apart in the presence of intracellular Exo1 (50 μ M). The exocytosis inhibitor Exo1 prevented the leftward shift of the second ramp I-V (red) as compared to the control ramp I-V (black). **B**, Consecutive I_{Ca} traces recorded from an axotomized Mb terminal in slice preparation, in response to voltage ramps 3 min apart in presence of iGluR antagonists NBQX (25 μ M) and D-AP5 (50 μ M). The antagonists prevented the leftward shift of the second trace (red) from control (black). Note the spontaneous outward GABAergic IPSCs at depolarized potentials in the absence of PTX.

ms depolarizing steps from -60 to -30 mV by $57.89 \pm 10.09\%$ (n=11) without altering the depolarization-evoked I_{Ca} charge transfer ($103.10 \pm 12.80\%$, data not shown).

These results collectively suggested that inhibition of glutamate release from Mb terminals by Exo 1 prevented the large depolarization-evoked modulation of their own I_{Ca} . This notion was also supported by two sets of results presented earlier showing lack of I_{Ca} modulation (1) when I_{Ca} I-Vs were generated by a series of short, stepwise depolarizations in an attempt to reduce Ca^{2+} influx into Mb terminals, but that protocol coincidentally also reduced overall glutamate release; and (2) in the presence of 10 mM intracellular BAPTA that was used to prevent Ca^{2+} triggered intracellular processes; BAPTA at this concentration was shown to effectively eliminate depolarization evoked exocytosis of glutamate from BC terminals (Singer and Diamond, 2003) including Mbs (Vigh and von Gersdorff, 2005).

Addition of the selective AMPA/kainate receptor antagonist NBQX (25 μ M) and NMDA receptor antagonist D-AP5 (50 μ M) to the external solution also prevented the characteristic leftward shift in I_{Ca} kinetics seen in response to the second voltage-clamp ramp (Fig. 3.4B). In these experiments, PTX was not present in the recording medium. Thus, spontaneous IPSCs, triggered by GABA release from amacrine cells (ACs), are superimposed on the I_{Ca} I-V although the reciprocal GABAergic feedback IPSCs, triggered by the depolarization-evoked glutamate release from Mb terminals, was blocked by ionotropic glutamate receptor (iGluR) antagonists NBQX and D-AP5 (Vigh et al., 2005). In the presence of NBQX (25 μ M) and D-AP5 (50 μ M) we found $V_{(5\%)}$ of -40.64 ± 0.67 mV for control and -40.53 ± 0.96 mV for the second ramp I-V, $V_{(50\%)}$ of -27.05 ± 0.49 mV for control and -27.09 ± 0.75 mV for the second ramp I-V, and $V_{(Max)}$ of -13.46 ± 0.76 mV for control and -13.66 ± 0.65 mV for the second ramp I-V. Statistical

analysis indicated no significant difference between control and second ramp I-V ($V_{(5\%)}$: $p=0.5$; $V_{(50\%)}$: $p=0.9$; $V_{(Max)}$: $p=0.4$, paired Student's t test, $n=9$).

As these recordings were obtained exclusively from axotomized Mb terminals that do not express either presynaptic AMPA/kainate- or NMDA receptors, the site of action of iGluR antagonists by which they prevented a shift in I_{Ca} I-V, can be attributed to neurons postsynaptic to the Mb terminals. Together, these data suggested that modulation of I_{Ca} kinetics at the Mb terminal required large depolarization of Mb terminals, followed by exocytosis of a large amount of glutamate to activate postsynaptic neurons, thereby initiating a feedback signal that positively modulated I_{Ca} in Mb terminals.

We tested further whether iGluR activation can trigger modulation of I_{Ca} in axotomized Mb terminals. Specifically, we recorded I_{Ca} from axotomized Mb terminals in response to a 10 ms depolarizing step from the holding potential of -60 mV to -40 mV, the membrane potential associated with threshold of L-type I_{Ca} in Mbs (Tachibana, 1999) (also see control $V_{(5\%)}$ Fig. 3.2Bi, Bii). As expected, upon depolarization, a tiny inward I_{Ca} was seen (Fig. 3.5A, black I_{Ca} trace) which was associated with a barely detectable (if any) increase in the membrane capacitance (4.09 ± 1.72 fF, $n=8$) of the Mb terminals (Fig. 3.5A, black C_m trace), indicating negligible glutamate release at this membrane potential (Tachibana, 1999). We then mimicked a large glutamate release from the Mb terminal by superfusing the retinal slices with the iGluR agonist KA (10 μ M) for 3 min. The repeated 10 ms depolarizing step to -40 mV after KA application triggered a substantially larger I_{Ca} (Fig. 3.5A, red I_{Ca} trace): the peak I_{Ca} increased from an average value of -20.66 ± 5.38 pA under control conditions to -46.95 ± 12.19 pA after KA application (Fig. 3.5B), which was statistically significant ($p=0.04$, paired Student's t test, $n=8$). Importantly, the elevated I_{Ca} triggered a clear increase in the membrane capacitance (Fig.

3.5A, red C_m trace) indicating glutamate release. For the tested Mb terminals, ΔC_m after KA increased to 12.49 ± 4.08 fF ($p=0.02$, paired Student's t test, $n=8$; Fig. 3.5A, C).

KA did not trigger any membrane currents in axotomized Mb terminals in the presence of PTX; therefore, these results suggested that KA depolarized neurons postsynaptic to the Mb terminal and initiated a feedback pathway. The increase in the depolarizing step evoked I_{Ca} , associated with a significant increase in the glutamate release from Mb terminals at a physiologically relevant membrane potential in the presence of KA was consistent with the notion that KA might have triggered some endogenous feedback signal generation in the inner retina which then shifted I_{Ca} activation to more negative potentials.

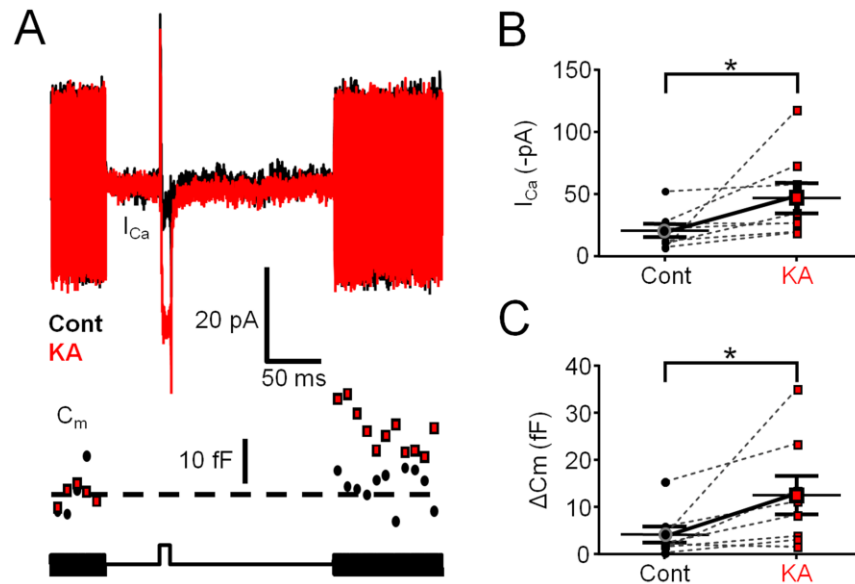


Figure 3.5. Activation of postsynaptic neurons potentiated I_{Ca} and exocytosis from Mb terminals. **A**, Depolarization of an axotomized Mb terminal from the holding potential (HP) of -60 to -40 mV for 10 ms activated tiny calcium influx through voltage-gated calcium channels (I_{Ca}), which triggered no glutamate release, as evidenced by the absence of increase in C_m . The protocol used is shown in the bottom trace. Bath application of 10 μ M Kainic Acid (KA) facilitated I_{Ca} and enhanced exocytosis (C_m) from the axotomized Mb terminals in response to a depolarizing step from -60 mV to -40 mV. Black: control; red: KA treatment. **B**, Summary figure displaying KA (10 μ M) effect on peak I_{Ca} in response to 10 ms step from -60 mV to -40 mV. Black circles: control; red squares: KA; *: $p=0.04$ paired Student's t test, $n=8$. **C**, Summary figure displaying KA (10 μ M) effect on ΔC_m in response to 10 ms step from -60 mV to -40 mV. Black circles: control; red squares: KA; *: $p=0.02$, paired Student's t test, $n=8$. Data are presented as mean \pm SEM.

NO, as a Retrograde Messenger, Modulated I_{Ca} at Mb Terminals

Our data presented so far implicated the presence of a retrograde signal that plays critical role in (strong) stimulation evoked modulation of I_{Ca} at Mb axon terminals. A prime candidate for such a retrograde signaling molecule is NO as it has been shown to shift I_{Ca} activation to more negative potentials in both rod photoreceptors (Kurenny et al., 1994) and cultured GCs (Hirooka et al., 2000) and is known to be released from inner retinal neurons by light (Eldred and Blute, 2005; Giove et al., 2009) or by glutamate (Tsumamoto et al., 2002).

First we tested whether the NO donor DETA/NO could alter I_{Ca} activation in dissociated Mbs. We found that bath application of DETA/NO (1 mM) resulted in a leftward shift in ramp-evoked I_{Ca} I-V (Fig. 3.6A) similar to that seen under control conditions for the second ramp-evoked I_{Ca} I-V of axotomized Mb terminals in slice preparation (Fig. 3.2Bi, Bii). On average, $V_{(5\%)}$ was -41.2 ± 1.01 mV for control and -47.5 ± 2.16 mV for the second ramp I-V, $V_{(50\%)}$ was -23.6 ± 0.74 mV for control and -28.9 ± 1.36 mV for the second ramp I-V, and $V_{(Max)}$ was -6.1 ± 0.99 mV for control and -10.4 ± 1.55 mV for the second ramp I-V. On average, the second ramp I-V exhibited an average difference of -6.3 ± 1.49 mV for $V_{(5\%)}$, -5.3 ± 0.84 mV for $V_{(50\%)}$, and -4.3 ± 0.73 mV for $V_{(Max)}$. Statistical analysis determined a significant difference in $V_{(5\%)}$, $V_{(50\%)}$ and $V_{(Max)}$ for the ramp I-V obtained in DETA/NO as compared to the control ($p=0.002$, $p=0.0001$ and $p=0.0002$, respectively, paired Student's t test, $n=10$).

Next, we examined whether endogenous NO generation and release, triggered by synaptic activity, contributes to the modulation of I_{Ca} at Mb terminals in retinal slice preparation. Specifically, we tested whether pharmacological inhibition of NO production by a nonselective inhibitor of both inducible and neuronal nitric oxide synthase (iNOS and nNOS, respectively),

TRIM, can reduce the negative shift in I_{Ca} activation following depolarizing ramps applied to the Mb terminals.

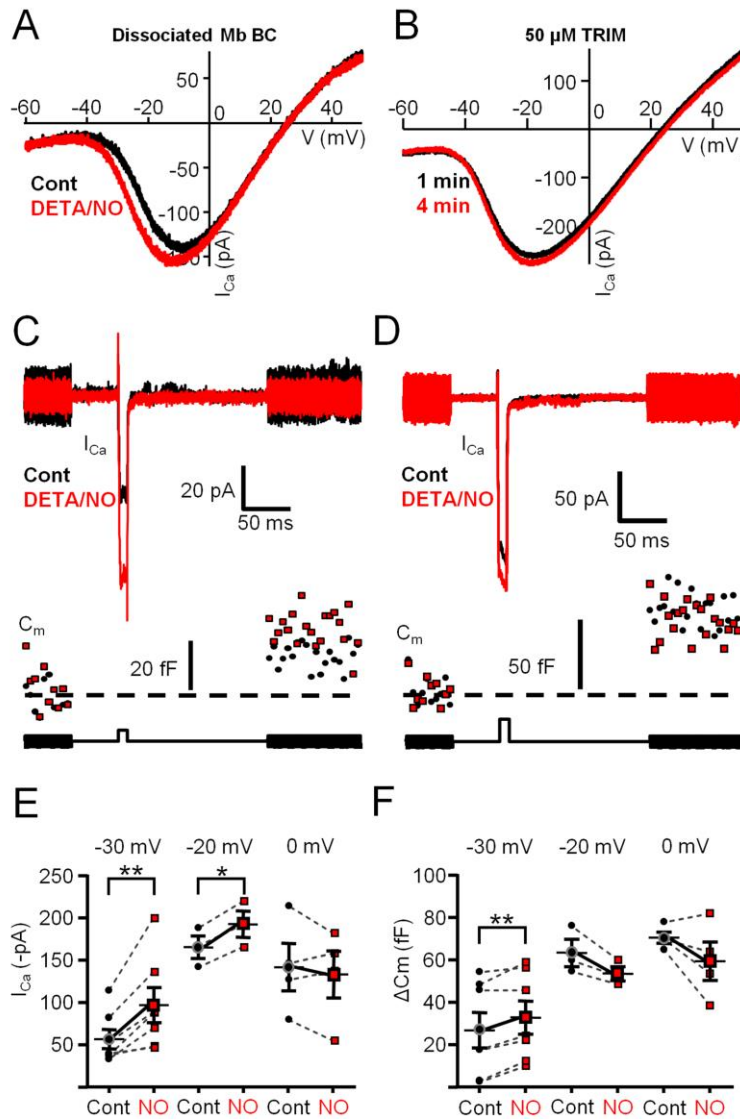


Figure 3.6. The NO donor-mediated shift of I_{Ca} caused weighted potentiation of Mb output selectively in response to weak stimuli. **A**, Application of NO donor DETA/NO (1 mM) for 1.5 min shifted the ramp-evoked I_{Ca} activation to more negative potentials in enzymatically dissociated Mbs (black: control; red: DETA/NO). **B**, Inhibition of endogenous nitric oxide synthases by TRIM (50 μ M) prevented the leftward shift of I_{Ca} activation in axotomized Mb terminals in slice preparation during consecutive ramp stimulations (black: control; red: second ramp I-V). **C**, Bath application of DETA/NO (1 mM) facilitated I_{Ca} and enhanced exocytosis (C_m) from the axotomized Mb terminals in response to a depolarizing step from -60 mV to -30 mV (HP: holding potential, bottom trace). Black: control; red: DETA/NO treatment. **D**, Bath application of DETA/NO (1 mM) slightly increased I_{Ca} , but this increase was not associated with increased exocytosis from axotomized Mb terminals in response to a depolarizing step from -60 mV to -20 mV (bottom trace). Black: control; red: DETA/NO treatment. **E**, Summary figure displaying DETA/NO (1 mM) effect on peak I_{Ca} in response to 10 ms step from -60 mV to -30, -20, or 0 mV. Black circles: control; red squares: DETA/NO; **: $p=0.004$, $n=7$; *: $p=0.008$, $n=3$; paired Student's t test. **F**, Summary figure displaying DETA/NO (1 mM) effect on ΔC_m evoked

by 10 ms step from -60 mV to -30, -20, or 0 mV. Black circles: control; red squares: DETA/NO; **: $p=0.003$, paired Student's t test, $n=7$, $n=3$ for -20 mV, $n=4$ for 0 mV. Every terminal was tested at one depolarization level in control then in the presence of DETA/NO, thus each pair of measurements shown originated from different cells. Data are presented as mean \pm SEM.

We found that continuous bath application of TRIM (50 μ M) eliminated the leftward shift in I_{Ca} activation kinetics following ramp depolarization of axotomized Mb terminals (Fig. 3.6B). On average, $V_{(5\%)}$ was -42.1 ± 1.63 mV for control and -42.5 ± 2.01 mV for the second ramp I-V, $V_{(50\%)}$ was -27.9 ± 1.57 mV for control and -28.63 ± 1.92 mV for the second ramp I-V,

and $V_{(Max)}$ was -13.75 ± 1.58 mV for control and -14.8 ± 1.90 mV for the second ramp I-V. In the presence of TRIM, there was no significant difference in $V_{(5\%)}$, $V_{(50\%)}$ and $V_{(Max)}$ between control and second ramp evoked I_{Ca} I-Vs ($p=0.6$, $p=0.3$ and $p=0.07$, respectively, paired Student's t test, $n=8$).

Together, these data suggested that the endogenous retinal retrograde messenger responsible for modulation of I_{Ca} at Mb terminals could be NO. The NO donor-evoked shift of I_{Ca} activation predicted an increase of I_{Ca} amplitude in the membrane potential range between -50 mV and -20 mV, which is physiologically relevant for Mb function (Saito et al., 1979; Wong et al., 2005). To test this notion directly we measured depolarization evoked I_{Ca} in response to a 10 ms depolarizing step from -60 mV to -30 mV, -20 mV or 0 mV along with the depolarization-evoked increase in the membrane capacitance (ΔC_m) of axotomized Mb terminals under control conditions and after at least 3 min of continuous bath application of DETA/NO (1 mM). We found that bath application of DETA/NO increased the peak I_{Ca} in response to a depolarizing step to -30 mV (Fig. 3.6C) from -56.61 ± 11.47 pA to -96.81 ± 20.62 pA (Fig. 3.6E, $p=0.004$; paired Student's t test, $n=7$). The NO-mediated increase of I_{Ca} at -30 mV was associated with enhanced exocytosis (Fig. 3.6C; C_m traces) from an average ΔC_m of 26.80 ± 8.31 fF under control conditions to 32.73 ± 7.79 fF after application of DETA/NO (Fig. 3.6F; $p=0.003$, paired Student's t test, $n=7$). Treatment with the NO donor also increased the peak I_{Ca} in response to steps to -20 mV (Fig. 3.6D) from -165.33 ± 13.27 pA to -192.59 ± 15.62 pA (Fig. 3.5E, $p=0.008$; paired Student's t test, $n=3$). However in these terminals, the I_{Ca} increase was not associated with an increase in exocytosis (ΔC_m : 63.27 ± 6.45 fF vs. 53.46 ± 3.37 fF in control and in DETA/NO, respectively, Fig. 3.6F, $p=0.09$; paired Student's t test, $n=3$). Neither the control I_{Ca} amplitude (-117.69 ± 17.15 pA) nor the corresponding membrane capacitance increase (ΔC_m : 67.99 ± 1.67

fF) was increased by DETA/NO (I_{Ca} : -116.69 ± 31.56 pA; ΔC_m : 59.31 ± 10.54 fF) significantly (I_{Ca} : $p=0.5$; ΔC_m : $p=0.2$, paired Student's t test, $n=4$) in response to depolarizing steps from -60 mV to 0 mV (Fig. 3.6E, F). These results were in perfect agreement with the NO donor evoked leftward shift in I_{Ca} activation (Fig. 3.6A) in that the weaker depolarization evoked voltage-gated I_{Ca} amplitude was enhanced more. Importantly, these results demonstrated that the NO-induced I_{Ca} modulation was reflected in weighted potentiation of glutamate output from Mb terminals.

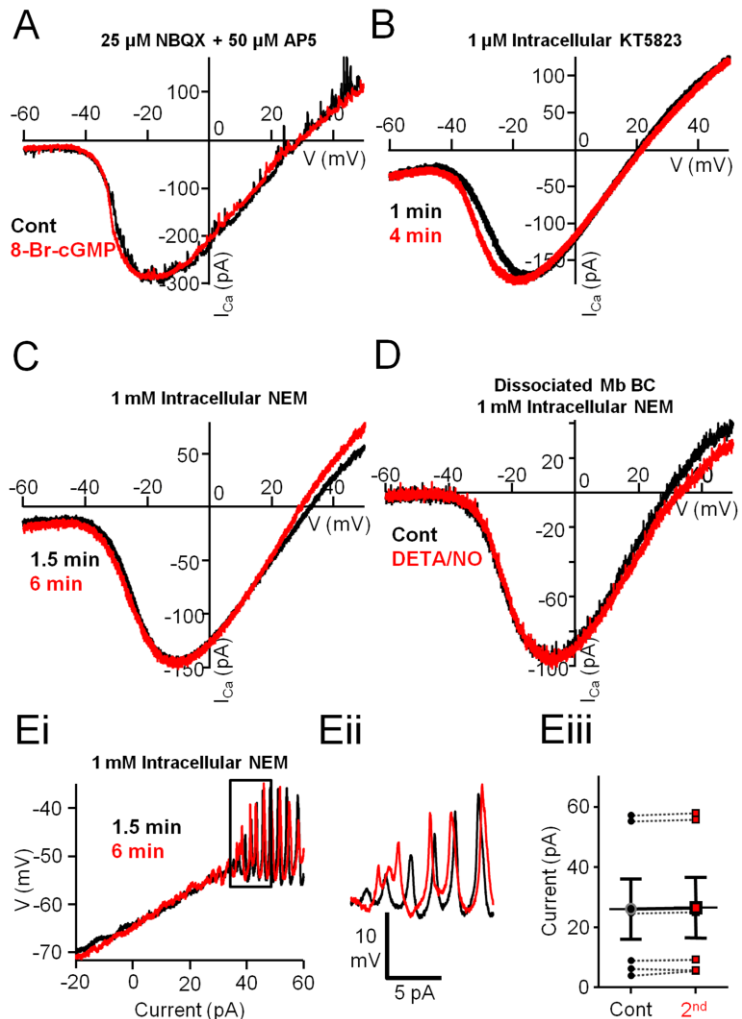
NO Modulated I_{Ca} Activation Threshold Through S-nitrosylation in Mb Terminals

Within recent years, NO's role as a retinal signaling molecule has been expanding rapidly (Vielma et al., 2012). The classical intracellular signaling cascade that underlies the effects of NO involves NO detection by soluble guanylate cyclase (sGC) which stimulates the production of cGMP. The increased levels of cGMP, in turn, stimulate protein kinase G (PKG), resulting in increased transmitter release in cones (Savchenko et al., 1997) and increased sensitivity of cone BCs (Snellman and Nawy, 2004).

In order to parse out the intracellular pathway associated with modulation of I_{Ca} in Mb terminals by NO, first we attempted to simulate the NO effect in enzymatically dissociated Mbs using the membrane permeable form of cGMP, 8-Br-cGMP. Application of an external solution containing 8-Br-cGMP (100-500 μ M) induced a large ("leak") current in 2 of 5 intact Mbs at -60 mV holding potential, making voltage-ramp evoked I_{Ca} I-Vs unreliable and inconsistent in the presence of 8-Br-cGMP (data not shown). These results were consistent with the expression of cyclic nucleotide-gated channels (CNGCs) in Mbs (Henry et al., 2003) that mediate a cation current when activated by focal application of 8-Br-cGMP onto the dendrites of Mbs in retinal slice (Ping et al., 2008). In the rest of the dissociated Mbs (3 of 5), the leak was not increased

during 8-Br-cGMP application, which we interpreted as a consequence of potentially damaged dendritic CNGCs. Nonetheless, in those Mbs 8-Br-cGMP did not alter I_{Ca} activation ($V_{(5\%)}$: $p=0.9$; $V_{(50\%)}$: $p=0.6$; $V_{(Max)}$: $p=0.7$, paired Student's t test, $n=3$). In our hands 8-Br-cGMP (500 μ M) did not induce a current in axotomized Mb terminals in slice preparation either (I_{hold} control: -26.45 ± 9.67 pA vs. cGMP: -36.92 ± 16.11 pA, $p=0.4$, paired Student's t test, $n=4$) further suggesting that functional CNGCs in Mbs might be restricted to the somatodendritic compartment. More importantly, in the presence of NBQX (25 μ M) and D-AP5 (50 μ M) or, in other words, under conditions when the reciprocal endogenous retinal pathway mediating the

Figure 3.7. Nitric oxide (NO) modulated I_{Ca} in Mb terminals through a cGMP-independent pathway that involved S-nitrosylation reactions. **A**, In the presence of NBQX and D-AP5, bath application of the membrane permeable cGMP analog 8-Br-cGMP (500 μ M) for 3 minutes failed to shift I_{Ca} activation of axotomized Mb terminals in slice preparation. **B**, KT5823 (1 μ M), a selective inhibitor of PKG, was unable to prevent the shift in I_{Ca} activation seen during consecutive ramp stimulations of Mb terminals in slice preparation. **C**, The leftward shift of the I_{Ca} I-V seen during consecutive ramp stimulations of Mb terminals in slice preparation was occluded by intracellular application of NEM (1 mM). **D**, In the presence of NEM (1 mM) in the intracellular solution, the NO donor, DETA/NO (1 mM), did not induce a leftward shift in the I_{Ca} activation threshold of dissociated, solitary Mbs. **Ei**, In the slice preparation, with NEM (1 mM) in the intracellular solution, no reduction in Ca^{2+} spike threshold was noticed during consecutive current ramp protocols applied to the axon terminal of Mbs. **Eii**, enlargement of boxed area in **Ei** illustrating that initiation threshold for Ca^{2+} spikes remained similar to that of control when S-nitrosylation reactions were prevented by NEM. **Eiii**, Summary diagram showing that, in the presence of NEM, no significant change was observed in the depolarizing current threshold of Ca^{2+} ramp-evoked responses. Black circles: control; red squares: second; $n=6$; 4 intact cells, 2 axotomized pooled.



shift in I_{Ca} activation was blocked (Fig. 3.4B), 8-Br-cGMP (500 μ M) did not alter the kinetics of voltage ramp-evoked I_{Ca} I-Vs (Fig. 3.7A). Statistical analysis revealed no significant difference between the control and subsequent ramp I-Vs recorded in the presence of 8-Br-cGMP ($V_{(5\%)}$: $p=0.9$, $V_{(50\%)}$: $p=0.7$ and $V_{(Max)}$: $p=0.4$, paired Student's t test, $n=4$).

KT5823 was shown to block the NO signaling cascade in retinal neurons by inhibiting PKG (Hirooka et al., 2000; Snellman and Nawy, 2004). Nonetheless, in the presence of 1 μ M KT5823 in the pipette solution, consecutive depolarizing ramps shifted the I_{Ca} activation to the left in axotomized Mb terminals in slice preparation (Fig. 3.7B) similar to what was found under control conditions (Fig. 3.2Bi, 2Bii). On average, $V_{(5\%)}$ was -44.0 ± 1.58 mV for control and -47.2 ± 1.77 mV for the second ramp I-V, $V_{(50\%)}$ was -29.5 ± 1.71 mV for control and -32.6 ± 1.73 mV for the second ramp I-V, and $V_{(Max)}$ was -15.0 ± 1.95 mV for control and -18.0 ± 1.84 mV for the second ramp I-V. The difference in I_{Ca} I-V curve parameters ($V_{(5\%)}$: -3.2 ± 0.37 mV; $V_{(50\%)}$: -3.1 ± 0.19 mV and $V_{(Max)}$: -3.0 ± 0.32 mV) was statistically significant ($V_{(5\%)}$: $p=0.001$; $V_{(50\%)}$: $p=0.00007$; $V_{(Max)}$: $p=0.0006$, paired Student's t test, $n=5$).

These findings discounted the role of an NO-stimulated cGMP-dependent pathway in altering I_{Ca} activation at Mb terminals and are in concert with the report showing that NO donor (SNAP) application failed to trigger cGMP elevation in Mbs in the goldfish retina (Baldrige and Fischer, 2001). An alternative mechanism of action by which NO can influence cellular function is through direct nitrosylation; in which NO covalently binds to the thiol side-chains of cysteine residues of various proteins to form S-nitrosothiols (S-nitrosylation) (for review, see Ahern et al., 2002). To assess whether NO-mediated S-nitrosylation played a role in the observed leftward shift of I_{Ca} activation in response to ramp I-Vs of axotomized Mb terminals, we introduced N-ethylmaleimide (NEM, 1 mM) into the intracellular solution. NEM is a potent inhibitor of S-

nitrosylation as it irreversibly reacts with and binds to sulfhydryl groups thereby preventing NO from engaging in an S-nitrosylation reaction. NEM prevented the leftward shift of I_{Ca} during consecutive voltage ramps in axotomized Mb terminals in retinal slice (Fig. 3.7C). On average, $V_{(5\%)}$ was -43.2 ± 0.92 mV for control and -44.0 ± 1.14 mV for the second ramp I-V, $V_{(50\%)}$ was -28.5 ± 0.71 mV for control and -27.6 ± 0.54 mV for the second ramp I-V, and $V_{(Max)}$ was -12.6 ± 0.68 mV for control and -11.6 ± 1.12 mV for the second ramp I-V. Statistical analysis determined no significant difference in $V_{(5\%)}$, $V_{(50\%)}$, and $V_{(Max)}$ between the control and second ramp evoked I_{Ca} I-Vs ($p=0.7$, $p=0.9$, and $p=0.4$, respectively, paired Student's t test, $n=5$). Similarly, in the presence of NEM (1 mM) in the pipette solution, bath application of 1 mM DETA/NO (Fig. 3.7D) failed to alter the parameters of voltage ramp evoked I_{Ca} I-V in enzymatically dissociated Mbs. On average, $V_{(5\%)}$ was -41.5 ± 1.26 mV for control and -41.8 ± 0.87 mV for the second ramp I-V, $V_{(50\%)}$ was -25.3 ± 1.45 mV for control and -25.7 ± 1.41 mV for the second ramp I-V, and $V_{(Max)}$ was -9.2 ± 2.32 mV for control and -9.7 ± 2.54 mV for the second ramp I-V. Statistical analysis revealed no difference between control and second ramp I-V parameters ($V_{(5\%)}$: $p=0.8$; $V_{(50\%)}$: $p=0.7$ and $V_{(Max)}$: $p=0.6$, paired Student's t test, $n=6$)

Last, we assessed whether preventing S-nitrosylation in Mb terminals also prevents the shift in Ca^{2+} spike threshold observed during stimulation of Mb terminals with consecutive depolarizing current ramps (Fig. 3.1). We found that blocking S-nitrosylation of proteins within the Mb terminal with NEM prevented a change in the threshold for Ca^{2+} spike initiation (Fig. 3.7Ei). An enlargement of the region of the trace where the spikes begin to originate shows no obvious difference in the threshold for initiation (Fig. 3.7Eii). On average, initiation of spikes during the first (control) ramp required 25.92 ± 9.98 pA, almost identical to that required during the second ramp applied 3 min later (26.47 ± 10.03 pA), and no significant difference between

the thresholds of calcium spikes were detected ($p=0.1$, paired Student's t test, $n=6$; 4 intact cells, 2 axotomized terminals, Fig. 3.7Eiii). Further, there was no shift in the membrane potential associated with the spike threshold. With 1 mM NEM in the internal solution, on average, spikes initiated at -45.35 ± 2.46 mV for control and at -44.82 ± 2.73 mV for the second trace ($p=0.4$, paired Student's t test, $n=6$; 4 intact cells, 2 axotomized terminals).

Light Induced NEM-sensitive Modulation of Mbs Response to Scotopic, Rod-Mediated Inputs in an Intensity Dependent Manner

Although direct nitrosylation of thiol side-chains of cysteine residues by NO plays an important role in numerous physiological processes (Ahern et al., 2002), it is a particularly important process in neurodegenerative diseases (Nakamura et al., 2013). Our results presented until this point show that this pathway can be triggered by endogenous, synaptically released glutamate which initiates retrograde modulation of I_{Ca} at the same presynaptic BC axon terminals. Nonetheless, the depolarizing ramp protocols that were shown to trigger this pathway consistently in our experiments were far from physiologically relevant depolarizations for Mbs. To study if our findings have functional consequences for normal visual processing or if this NO-mediated process can only exist under experimental conditions in retina, we designed a set of experiments where depolarizations of Mbs were evoked by light stimulations, based on (1) the observation that NO release in the retina is triggered by increasing light intensity (Eldred and Blute, 2005; Giove et al., 2009), (2) our preceding experiments suggesting that small depolarizations of Mb terminals might be preferentially potentiated by endogenous NO which appeared to be released in our prep by large synaptic depolarizations of inner retinal neurons (Figures 3.2Bi, 3.5) and that (3) magnitude of depolarization in ON BCs is related to strength

and wavelength of illumination (Joselevitch and Kamermans, 2007; Jarsky et al, 2011). Although we did not intend to simulate Mb responses to natural underwater visual scenes, the wavelength and intensity of light stimulations were selected to match those behaviorally relevant in shallow water (Munz and McFarland, 1973; McFarland and Munz, 1975; Loew and McFarland, 1990). Additionally, the light stimulations were chosen in accordance with the observations that Mbs in the fish retina receive direct inputs from both rods and cones (Wong et al., 2005; Joselevitch and Kamermans, 2007) similar to many BCs in cold blooded vertebrate retinas (Wu, 1994) and certain mammalian BCs (Protti et al., 2005; Haverkamp et al., 2008; Pang et al., 2010a).

In these experiments, light-evoked responses of intact Mbs were recorded directly from their axon terminals in current-clamp mode from dark-adapted retinal slices. Mbs were slightly hyperpolarized to keep their membrane potential at about -51 mV, which prevented spontaneous Ca^{2+} spike firing in the dark. Figure 3.8Ai shows representative control responses recorded from the axon terminal of an intact Mb, evoked by two sets of 3 consecutive dim (1.6×10^7 photons/cm²/s) green flashes ($\lambda=505$ nm, 500 ms) applied 5 s apart and with 4 minutes between the two sets of light stimuli. The responses to the same light stimulation showed great variability in the number and amplitude of the Ca^{2+} spikes (Fig. 3.8Ai) but they were rather consistent in terms of the latency within sets as well as across consecutive sets (Fig. 3.8Aii): for the Mb shown, the latency of first light-evoked spikes varied between 245 ms and 258 ms, averaging at 251.33 ± 3.76 ms for the first set and varied between 249 ms and 250 ms averaging at 249.67 ± 0.3 ms for the second set of stimulations (Fig. 3.8Aiii). When latencies of these dim green light (1.6×10^7 photons/cm²/s, $\lambda=505$ nm, 500 ms) evoked spikes between the first and second sets (248.6 ± 14.6 ms vs. 247.02 ± 13.8 ms, respectively) were compared across multiple cells (n=6), we found no significant statistical difference ($p=0.6$, paired Student's *t* test).

In the next set of experiments, we devised a protocol with the intent to determine whether the Mb spiking response could be sensitized by light. The general framework of the light stimulation consisted of an initial light flash, followed by a brighter, “sensitizing” light flash, and then a repeat presentation of the initial flash. This paradigm allowed us to compare the light evoked spiking response of the Mb terminal before and after a sensitizing light stimulus and use the observed differences as a metric for whether or not the terminal had been “sensitized.” Specifically, the retina was exposed to a series of full field green ($\lambda=505$ nm) light flashes (500 ms) with increasing intensities ranging from scotopic (7×10^6 photons/cm²/s) to dim photopic (1.2×10^{11} photons/cm²/s) intensities (Busskamp et al., 2010). Then a 500 ms bright red light (sensitizing) stimulus ($\lambda=660$ nm, 5×10^{13} photons/cm²/s) was delivered. With a minimum delay of 5 min after the red light flash, the series of (initial) green light flashes were repeated. Figure 3.8Bi shows a representative recording where we found that the second dim green flash (1.6×10^7 photons/cm²/s), applied after sensitizing red stimulation, triggered a spiking response from the Mb axon terminal with shorter delay compared to that evoked by the same intensity before the red flash (Fig. 3.8Bi, 3.8Bii) as if the terminal was “sensitized” by the bright red light stimulation. Similar shortening of first spike delay was seen in every cell tested (9/9, Fig. 3.8Biii) at this green light intensity and was found to be statistically significant ($p=0.006$, paired Student’s *t* test). Interestingly, the delay of light responses to bright (1.2×10^{11} photons/cm²/s) green light of the same Mb were not different before and after the bright red stimulation (Fig. 3.8Ci, 3.8Cii). Across cells, the latency to first spike increased in 7/17 Mbs, decreased in 6/17 and remained virtually unaltered in 4/17 cells (Fig. 3.8Ciii), and when summed, no statistically significant difference was detected ($p=0.1$, paired Student’s *t* test, $n=17$). Of the six different intensities of green light presented in this set of experiments, a significant decrease in latency

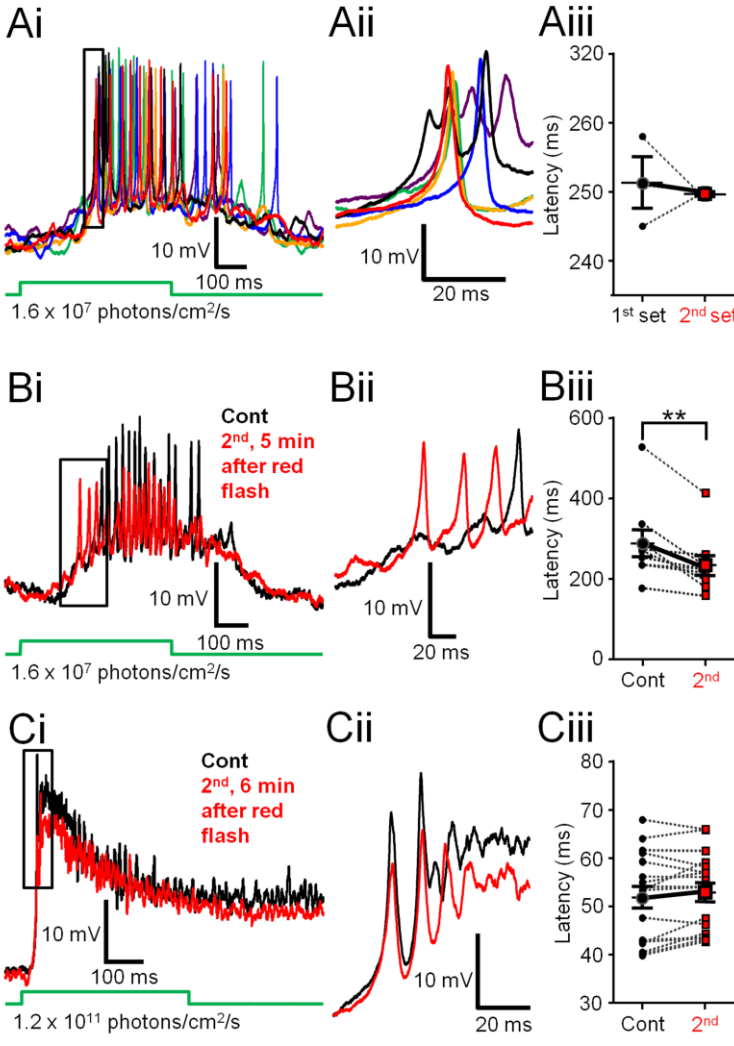
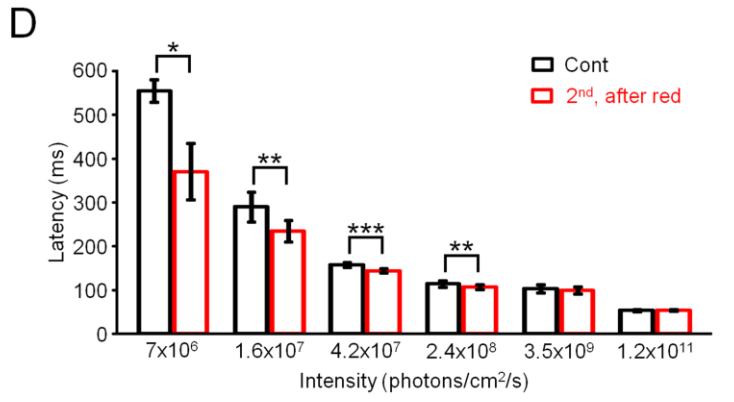


Figure 3.8. Photopic light stimulation modulated scotopic light responses of Mb axon terminals.

Ai, Repeated scotopic green light flashes (500ms, $\lambda=505$ nm, 1.6×10^7 photons/cm²/s) did not significantly alter the latency of evoked Ca²⁺ spikes from the axon terminal of an intact Mb. The first set of responses (black, blue, and green traces) were evoked by three distinct flashes of dim green light with a 5 s delay between flashes. After a 4 min delay, a second set of responses (purple, red, and orange traces) was evoked by three distinct flashes of dim green light. Membrane potentials at the beginning of the traces: -51.8 mV (black), -48.9 mV (blue), -52.4 mV (green), -47.9 mV (purple), -50.8 mV (red), and -52.1 mV (orange). **Aii**, Enlargement of boxed area in Ai. Membrane potentials at the beginning of the traces are -44.6 mV (black), -44.7 mV (blue), -43.3 mV (green), -41.9 mV (purple), -44.6 mV (red), and -46.6 mV (orange). **Aiii**, Summary graph comparison of latency to first spikes of responses triggered by the first and second set of dim green (505 nm, 1.6×10^7 photons/cm²/s) light flashes. Black circles: first set; red squares: second set. **Bi**, Rod-mediated scotopic green (505 nm, 1.6×10^7 photons/cm²/s, 500 ms) evoked responses from the axon terminal of an intact Mb, in dark-adapted retina slice preparation, (black) were modulated by bright red light stimulation (500 ms, 660 nm, 5×10^{13} photons/cm²/s) 5 min after bright red flash, the repeated dim green stimulus evoked spiking response with decreased latency (red trace). Membrane potential at the beginning of both traces was -51 mV. **Bii**, Enlargement of boxed area in Bi. Membrane potentials at the beginning of traces are -50.5 mV (red) and -52.8 mV (black). **Biii**, Summary graph showing paired comparison of latency to first spike triggered by dim green flash before and after bright red. The latency to first spike was significantly reduced for the second stimulus, on average by 55.18 ± 14.98 ms. Black circles: control; red squares: second,



p=0.006 (paired Student's t test) n=9. **Ci, Responses of Mb terminal to mesopic green (500 ms, 505 nm, 1.2×10^{11} photons/cm²/s) light, before (black) and 5 min after (red) the bright red flash. Membrane potential at the beginning of traces was -52 mV. **Cii**, Enlargement of boxed area in Ci. Membrane potentials at the beginning of traces are -50.25 mV (red) and -50.1 mV (black). **Ciii**, Summary graph of paired comparison of mesopic green light response latency before and after red light; n=17. **D**, Average latency to first spike from green light responses triggered by 6 intensities before (black) and 5 min after (red) bright red stimulation. A significant decrease in latency was observed in response to dim, scotopic intensities known to stimulate rods, but not cones ($\leq 3.5 \times 10^9$ ph/cm²/s): 7×10^6 ph/cm²/s; n=3, *p=0.04. 1.6×10^7 ph/cm²/s; n=9, **p=0.006. 4.2×10^7 ph/cm²/s; n=17 ***p=0.0001. 2.4×10^8 ph/cm²/s; n=17, **p=0.02; 3.5×10^9 ph/cm²/s: n=17; 1.2×10^{11} ph/cm²/s: n=17. (Paired Student's t test). Data are mean \pm SEM.

was observed in those under intensities known to stimulate only rods ($\leq 10^8$ photons/cm²/s) and was not observed in intensities above cone threshold ($\sim 10^9$ photons/cm²/s in the goldfish retina, Joselevitch and Kamermans, 2009). The dimmest green light stimulus used in our experiments (7×10^6 photons/cm²/s) produced a spiking response with an average latency of 553.50 ± 25.74 ms in control (first) and with 369.37 ± 63.80 ms after the red flash (second); in response to a 1.6×10^7 photons/cm²/s flash, the average latency was 288.71 ± 33.36 ms in control (first) and 233.54 ± 24.44 after the red flash (second); in response to a 4.2×10^7 photons/cm²/s flash the average latency was 156.92 ± 5.12 ms in control (first) and 142.55 ± 4.69 after the red flash (second); in response to a 2.4×10^8 photons/cm²/s flash, the average latency was 112.99 ± 7.19 ms in control (first) and 105.93 ± 5.97 after the red flash (second); in response to a 3.5×10^9 photons/cm²/s flash the average latency was 101.57 ± 8.59 ms in control (first) and 98.85 ± 7.99 after the red flash (second); in response to a 1.2×10^{11} photons/cm²/s flash the latency was 51.89 ± 2.24 ms in control (first) and 52.93 ± 1.97 after the red flash (second) (Fig. 3.8D). Note that the latency, as well as the variability in latency across cells, decays as light intensity increases. These results are consistent with the observation that temporal precision of spikes produced by BCs, evoked by high contrast light stimulation, is in the millisecond range, which correlates with that of AC and GC spikes in the fish retina (Baden et al., 2011).

The intensity of sensitizing light stimulus used in the previous experiment was sufficient to activate both rod and cone inputs to Mbs (Joselevitch and Kamermans, 2007). In the next set of experiments, we sought to parse out the contribution of rod- and cone-mediated signaling in triggering the light-induced sensitization of dim scotopic light ($\lambda=505$ nm, 500 ms, 1.6×10^7 photons/cm²/s) responses. This particular scotopic intensity was selected as it reliably evoked spiking responses in Mbs with relatively high temporal precision (Fig. 3.8Ai, 8Aii) and exhibited

a latency that did not change over the time course (~5 min) of these experiments (Fig. 3.8Aiii). However, the latency of responses to this scotopic intensity showed significant reduction, after bright red sensitizing light stimulation, consistently across cells (Fig. 3.8Biii). We found that a full field green flash ($\lambda=505$ nm, 500 ms) with an intensity of 2.4×10^8 photons/cm²/s, which is just below cone threshold in the fish retina (Joselevitch and Kamermans, 2009), could also reduce the latency of consecutive light responses evoked by the dim scotopic green flash. On average, the latencies of the spiking response were reduced from 281.12 ± 11.28 ms to 249.86 ± 10.75 ms (Fig. 3.9Ai, 3.9Aii) reliably (in 11/11 experiments, Fig. 3.9Aiii) and the reduction was proven statistically significant ($p=0.0001$, paired Student's *t* test, $n=11$). In the next experiments, we increased the sensitizing green flash ($\lambda=505$ nm, 500 ms) stimulus intensity to 10^{10} photons/cm²/s. This mesopic intensity saturates rods (Sterling, 2003; Busskamp et al., 2010) and starts to activate cones (Joselevitch and Kamermans, 2009). As expected, flashes at this intensity also reduced the latency of consecutive dim green, flash-evoked responses in every cell tested (Fig. 3.9Bi, 3.9Bii) (control: 275.29 ± 9.41 ms vs. second: 230.84 ± 10.17 ms) in a statistically significant manner ($p=0.00008$, paired Student's *t* test, $n=7$, Fig. 3.9Biii). When compared across experiments, we found that the reduction of dim scotopic green ($\lambda=505$ nm, 500 ms, 1.6×10^7 photons/cm²/s) response latencies triggered by the sensitizing light was intensity dependent: it was the largest (55.18 ± 14.98 ms, $n=9$) for bright photopic red ($\lambda=660$ nm, 500 ms, 5×10^{13} photons/cm²/s), followed by the reduction of (44.44 ± 4.71 ms, $n=7$) caused by rod-saturating mesopic green ($\lambda=505$ nm, 500 ms, 10^{10} photons/cm²/s) flashes and was the smallest (31.25 ± 3.12 ms, $n=11$) for bright scotopic green ($\lambda=505$ nm, 500 ms, 2.4×10^8 photons/cm²/s) stimuli. However, when the latency changes caused by these three sensitizing light stimulations were statistically analyzed, no significant difference was detected among them (One-way ANOVA,

with Tukey's multiple comparison test). These results indicated that bright scotopic signals, which are processed and conveyed to the inner retina by Mbs, were sufficient to potentiate processing of consecutive weak rod inputs by Mbs. Light stimuli bright enough to activate cones might trigger further activity-dependent weighted potentiation of Mb signaling. Together, the data demonstrated that the strength of Mb depolarization drove the retrograde, NO-mediated modulation of Mb terminal signaling.

Next we tested whether similar modulatory mechanism affects photopic signals processed by Mbs; specifically, we tested whether weak photopic responses of Mb terminals evoked by red flashes ($\lambda=660$ nm, 500 ms, 1.2×10^{11} photons/cm²/s) can be also sensitized by bright photopic stimulation ($\lambda=660$ nm, 500 ms, 5×10^{13} photons/cm²/s) in a similar manner. When delivered on a dark background, the weak photopic red ($\lambda=660$ nm, 500 ms, 1.2×10^{11} photons/cm²/s) and the rod-saturating green ($\lambda=505$ nm, 10^{10} photons/cm²/s) stimulation evoked identical responses in Mb terminals (Fig. 3.9Ci and 3.9Cii, respectively): the spikes merged into a transient initial depolarization that was followed by a depolarized plateau with superimposed small spikes/membrane potential oscillations, which exceeded the length of the illumination. The membrane potential of the plateau varied between -33.25 mV and -40.05 mV and averaged at -37.22 ± 2.41 mV (n=7). To isolate cone responses, red flashes were delivered on a rod-saturating green background ($\lambda=505$ nm, 10^{10} photons/cm²/s) which was turned on 4 s before the first red stimulations. Neither weak (1.2×10^{11} photons/cm²/s) nor strong (5×10^{13} photons/cm²/s) photopic red stimulation ($\lambda=660$ nm, 500 ms), when superimposed on the rod-saturating green background, evoked detectable responses (Fig. 3.9Ciii). These results remain consistent with the observation that Mbs process rod-dominant visual signals and nearly saturate at intensities of 10^{10} photons/cm²/s (Joselevitch and Kamermans, 2009).

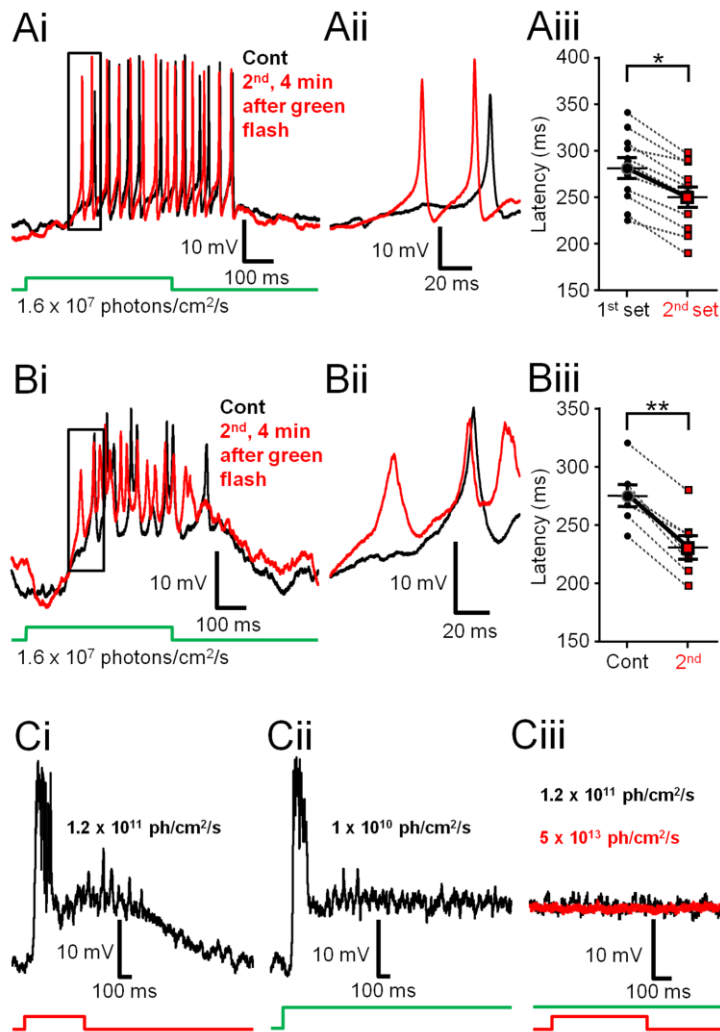


Figure 3.9. Scotopic light responses of Mb axon terminals can be modulated by light through rod specific pathways. **Ai**, Rod-mediated responses recorded from the axon terminal of an intact Mb to a full-field light flash (500 ms) of scotopic green ($\lambda=505$ nm, 1.6×10^7 photons/cm²/s) before (black) and 4 min after (red) a bright scotopic green ($\lambda=505$ nm, 2.4×10^8 photons/cm²/s) full-field light flash (500 ms). Following stimulation with the bright scotopic green light, the repeated dim green stimulus evoked a spiking response with decreased latency when compared to control. Membrane potentials at the beginning of the traces are -51.9 mV (red) and -49.2 mV (black). **Aii**, Enlargement of boxed area in **Ai** illustrating the decreased latency of rod-mediated light induced Ca²⁺ spikes when the green scotopic stimulus is increased by one order of magnitude. Membrane potentials at the beginning of the traces are -49.5 mV (red) and -48.9 mV (black). **Aiii**, Summary graph showing paired comparison of latency to first spike triggered by dim green (505 nm, 1.6×10^7 photons/cm²/s) flash before and after presentation of sensitizing green light (505 nm, 2.4×10^8 photons/cm²/s) recorded from different Mb terminals. The latency to first spike was significantly reduced for the second stimulus, on average by 31.25 ± 3.12 ms. Black circles: control; red squares: second; **: $p=0.0001$, paired Student's *t* test, $n=11$. **Bi**, Responses of an Mb terminal

evoked by a scotopic green (505 nm, 1.6×10^7 photons/cm²/s) light flash (500 ms) of a dark-adapted retina (black) were modulated by a rod-saturating bright green (500 ms, 505 nm, 1.0×10^{10} photons/cm²/s) light flash. 4 minutes after the bright green flash, a repeated dim green stimulus evoked a spiking response with decreased latency (red) as compared to control. Membrane potential at the beginning of the trace was -47.14 mV (red) and -49.47 mV (black). **Bii**, Enlargement of boxed area in **Bi** illustrating the decrease in latency observed in scotopic green light-evoked Ca²⁺ spikes following rod saturating green light stimulation. Membrane potentials at the beginning of the traces are -48.79 mV (red) and -48.92 mV (black). **Biii**, Summary graph showing paired comparison of latency to first spike triggered by dim green (505 nm, 1.6×10^7 photons/cm²/s) flash before and after presentation of bright green light (505 nm, 1.0×10^{10} photons/cm²/s). The latency to first spike was significantly reduced for the second stimulus, on average by 44.44 ± 4.71 ms. Black circles: control; red squares: second; **: $p=0.00008$, paired Student's *t* test, $n=7$. **Ci**, Responses recorded from an Mb terminal evoked by a weak photopic red flash (500 ms, $\lambda=660$ nm, 1.2×10^{11} photons/cm²/s). Membrane potential at the beginning of the trace is -50.5 mV. **Cii**, Response from the same Mb axon terminal evoked by a sustained presentation of rod saturating green light ($\lambda=505$ nm, 1.0×10^{10} photons/cm²/s). Membrane potential at the beginning of the trace is -50.9 mV. **Ciii**, Neither weak photopic (1.2×10^{11} photons/cm²/s) nor brighter (5×10^{13} photons/cm²/s, applied 9 min later) red flash (500 ms, $\lambda=660$ nm) evoked measurable responses in Mb terminals (black and red traces, respectively) when applied on top of sustained rod-saturating green background illumination ($\lambda=505$ nm, 1.0×10^{10} photons/cm²/s). Membrane potentials at the beginning of traces: -40.3 mV (black), and -43.9 mV (red).

Collectively, these data suggested that the latency of light evoked Ca^{2+} spikes in Mb terminals is subject to plasticity; in our experimental protocol a flash of light with intensity $\geq 2.4 \times 10^8$ photons/cm²/s shortened the latency, especially for Ca^{2+} spikes evoked by scotopic light intensities. This pattern closely resembled what was reported for NO-mediated changes in cone BC sensitivity in mammalian retinas: NO increased BC sensitivity to weak inputs but did not alter strong ones (Snellman and Nawy, 2004). However, our results could also be explained by an NO-mediated effect localized to the Mb terminals, in which NO via S-nitrosylation reaction caused a shift in I_{Ca} activation that resulted in reduction of Ca^{2+} spike threshold, leading to shortened first spike delay in response to weak inputs.

To test this notion directly, we repeated previous experiments where we observed light induced changes in the Mb terminal's scotopic responses under conditions that prevented S-nitrosylation by including NEM (1 mM) in the recording pipette. We found that in the presence of NEM, the latency of dim scotopic green responses (1.6×10^7 photons/cm²/s) was slightly increased in 3 out of 4 experiments (Fig. 3.10Ai, 3.10Aii), and was reduced in 1 out of 4 experiment following a bright scotopic (2.4×10^8 photons/cm²/s) green flash (Fig. 3.10Aiii). On average, no significant change was detected (control: 243.04 ± 19.09 ms vs. second: 246.06 ± 16.05 ms, $n=4$, Fig. 3.10Aiii; $p=0.6$, paired Student's *t* test). To test whether a photopic sensitizing stimulus also alters the scotopic response latency in Mb terminals in a NEM-sensitive manner, we performed a similar experiment using 500 ms long flashes of bright red ($\lambda=660$ nm) light with intensity of 5×10^{13} photons/cm²/s to sensitize scotopic green flash (4.2×10^7 photons/cm²/s) responses. In the presence of intracellular NEM (1 mM), no reduction of spike latency was observed in response to scotopic green stimulations (Fig. 3.10Bi, 3.10Bii) in any tested cell ($n=3$, Fig. 3.10Biii; $p=0.1$, paired Student's *t* test).

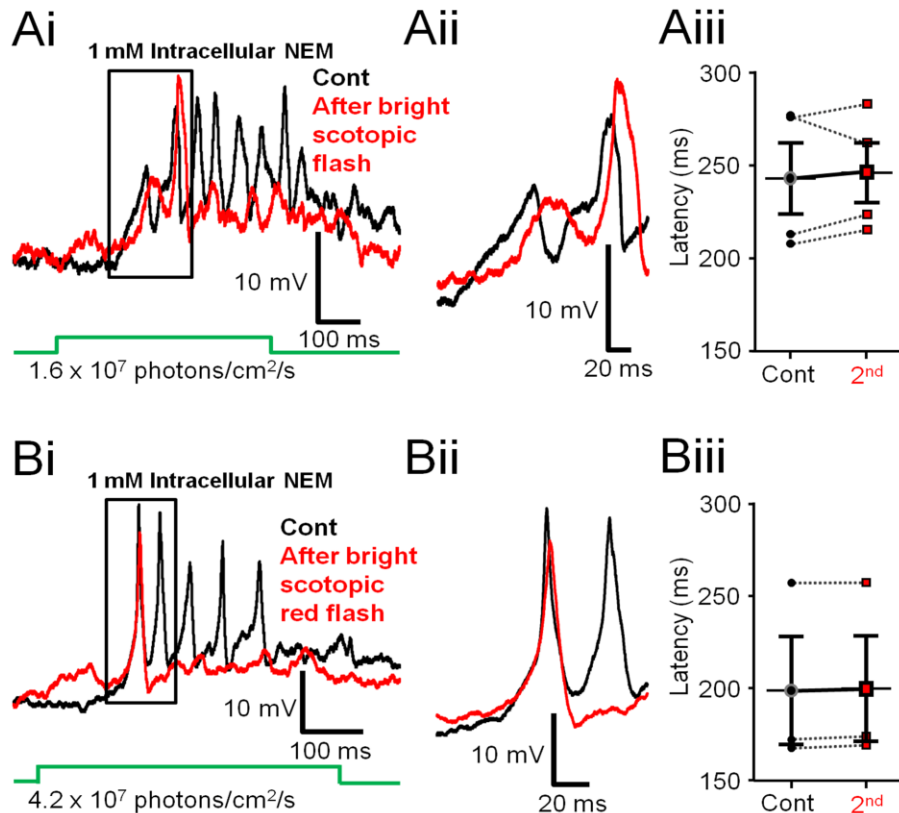


Figure 3.10. Both bright scotopic and photopic light induced modulation of scotopic light responses in Mb terminals in a NEM sensitive manner. **Ai**, Including NEM (1 mM) in the pipette solution prevented bright scotopic light stimulation (500 ms, $\lambda=505$ nm, 2.4×10^8 photons/cm²/s) from reducing the latency of dim scotopic green light (500 ms, $\lambda=505$ nm, 1.6×10^7 photons/cm²/s) responses of Mb terminals. Membrane potentials at the beginning of traces shown in **Ai** are -48.7 mV (black) and -48.4 mV (red). **Aii**, Enlargement of boxed area in **Ai** illustrating that the delay of dim scotopic green light-induced Ca²⁺ spikes, following the bright scotopic green stimulation, remained similar to that of control in the presence of NEM. Membrane potentials at the beginning of traces are -49.5 mV (black) and -47.6 mV (red). **Aiii**, Pairwise comparison showing no significant difference in latency of scotopic light responses (500 ms, $\lambda=505$ nm, 1.6×10^7 photons/cm²/s) compared before and 5 min after bright scotopic green flash (500 ms, $\lambda=505$ nm, 2.4×10^8 photons/cm²/s) in the presence of NEM. Black circles: control; red squares: second; n=4. **Bi**, When NEM (1 mM) was included in the pipette solution the bright red flash (500 ms, 660 nm, 5×10^{13} photons/cm²/s) did not induce a leftward shift in the latency to first spike triggered by scotopic green stimulation (505 nm, 4.2×10^7 photons/cm²/s). Membrane potential at the beginning of both traces shown in **Bi** is -52 mV. **Bii**, Enlargement of boxed area in **Bi** illustrating that the delay of scotopic green light-induced Ca²⁺ spikes, following the bright red stimulation, remained similar to that of control in the presence of NEM. Membrane potentials at the beginning of traces are -48 mV (red) and -50 mV (black). **Biii**, Pairwise comparison showing no significant difference in latency of scotopic light responses (505 nm, 4.2×10^7 photons/cm²/s) compared before and 5 min after bright red flash in the presence of NEM. Black circles: control; red squares: second; n=3. Data are Mean \pm SEM.

Note however, the reduction of light-evoked Ca²⁺ spikes in the presence of intracellular NEM in both sets of experiment (Fig. 3.10Ai, 3.10Bi) indicating a possible inhibitory NEM effect on dendritic signaling besides preventing S-nitrosylation in intact Mbs (Shapiro et al., 1994). It is important to note that light-induced modulation of rod-mediated dim light responses

recorded at the Mb terminals could be influenced by multiple upstream NO-mediated processes acting on (1) rods (Kurenny et al., 1994), (2) cones (Savchenko et al., 1997) and/or (3) horizontal cells (Baldrige and Fischer, 2001) making the use of NOS inhibitor TRIM in these experiments inappropriate. Nonetheless, it is unlikely that the NO-mediated, cGMP dependent increase in Mb sensitivity for weak inputs (Snellman and Nawy, 2004) played a role in modulation of dim light responses, because unlike in horizontal cells, NO donor failed to visibly increase cGMP levels in Mb terminals in the goldfish retina, even in the presence of PDE blocker (Baldrige and Fischer, 2001).

3.5 Discussion

The present study describes a novel NO-dependent modulatory mechanism that alters the output of Mb-type BCs. The major findings of this investigation were: (1) Ca^{2+} spike threshold in Mb terminals is subject to activity-dependent plasticity, (2) glutamate released by strong depolarization of a single Mb terminal is sufficient to trigger generation and delivery of NO, (3) NO can act in a retrograde manner to lower I_{Ca} threshold in strongly stimulated Mb terminals via a NEM-sensitive S-nitrosylation mechanism, (4) Mb terminals subjected to endogenous or exogenous NO show weighted potentiation: they respond to weak depolarizing inputs with enhanced glutamate output, while maintaining input-output ratio (gain) for strong stimuli and (5) exposure to light with intensity $\geq 2.4 \times 10^8$ photons/cm²/s induced weighted potentiation of scotopic responses in Mb terminals (expressed as reduced Ca^{2+} spike delay) in a NEM-sensitive manner.

Nitric Oxide Modulation of Retinal Signaling

In vertebrate retinas NO is synthesized mainly by the neuronal type NO synthase (Dawson et al., 1991; Tsumamoto et al., 2002), although endothelial (Haverkamp et al., 1999) as well as the inducible (Palamalai et al., 2006) types are also present. Extensive investigations using immunohistochemistry and *in situ* hybridization detected these enzymes in subtypes of all retinal cell classes with species-dependent patterns (Vielma et al., 2012). The best known retinal effect of NO is the uncoupling of gap junctions between horizontal cells in a variety of species (Daniels and Baldrige, 2011; De Vries and Schwartz, 1989; Lu and McMahon, 1997) that is mediated by increased intracellular cGMP via soluble guanylate cyclase (sGC). Similarly, gap junctions between AII ACs and BCs are regulated by NO in a cGMP-dependent manner (Mills and Massey, 1995). Indeed, a number of reports demonstrated increased retinal cGMP synthesis in response to NO donor application (Blute et al., 1998; Gotzes et al., 1998; Baldrige and Fischer, 2001; Saenz et al., 2002). In addition, NO triggered increases in cGMP can open CNGCs and in turn, trigger transmitter release from cones in salamander (Rieke and Schwartz, 1994) and lizard (Savchenko et al., 1997) retinas.

Not all actions of NO are mediated through cGMP-dependent pathways in the retina: NO was shown to modulate I_{Ca} of rods in salamander independent of cGMP (Kurenny et al., 1994). Most interestingly, the activation threshold of I_{Ca} in salamander rods was shifted to the left, resulting in a decrease of $V_{1/2}$ by -4.3 ± 0.6 mV (Kurenny et al., 1994). Those results are strikingly similar to our data (Fig. 3.6A, $V_{50\%}$: ~ -5.5 mV), thus our findings and conclusions support the speculation of Kurenny et al (1994) suggesting S-nitrosylation as a possible mechanism by which NO could alter I_{Ca} threshold in salamander rods. The similarities between

the results of the two studies suggest that I_{Ca} modulation through NO-triggered S-nitrosylation reactions could be a ubiquitous regulatory process in the vertebrate retina.

Can NO-Mediated S-nitrosylation in Mbs Occur Under Physiological Conditions?

Direct nitrosylation of thiol side-chains of cysteine residues by NO plays an important role in numerous physiological processes by triggering dynamic conformational changes which affect protein-protein interactions or influence protein location (Ahern et al., 2002). Yet, S-nitrosylation in the nervous system is particularly characteristic during periods of oxidative stress and in neurodegenerative diseases in which NO levels are elevated (Nakamura et al., 2013). We were able to trigger this NO pathway by endogenous synaptic glutamate, released from a single presynaptic terminal, which resulted in the retrograde modulation of I_{Ca} through S-nitrosylation reactions at the same presynaptic Mb terminals. However, the depolarizing ramp protocols that were proven to trigger this pathway, and in turn consistently shifted I_{Ca} threshold in a NEM-sensitive manner (Fig. 3.1, Fig. 3.2Bi, 3.2Bii) were robust and Mb terminals were depolarized far above their physiologically relevant maximal membrane potential (~ -20 mV, Saito and Kujiraoka, 1982; Protti et al., 2000). Importantly, we were able to trigger changes in dim ($\sim 10^7$ photons/cm²/s) light-evoked Ca^{2+} spike responses of Mb terminals by brighter ($\geq 2.4 \times 10^8$ photons/cm²/s) light: the sensitizing bright light decreased the latency of the first light-evoked Ca^{2+} spike in a NEM-sensitive manner (Fig. 3.10), consistent with a light-evoked decrease in I_{Ca} activation threshold through S-nitrosylation reactions.

Precise measurement of increases in membrane capacitance associated with our standard voltage ramp protocol was problematic because of the long tail currents (Gillis, 2000), but based on our best measurements (n=3) it was around ~ 350 fF. Direct measurement of light-evoked

membrane capacitance increase of intact Mbs is also complicated because of their complex morphology (Mennerick et al., 1997) and the slowly decaying light-evoked synaptic conductances (Saito and Kujiraoka, 1982). However, when membrane potential waveforms triggered by 500 ms bright red light flash (similar to the ones used to “sensitize” the Mb terminals, Fig. 3.8Bi, 3.8Bii, 3.8D) recorded from the axon terminal of intact Mbs were used as command potentials of voltage-clamp protocols in separate experiments, they triggered membrane capacitance increase of 275 ± 48 fF (n=10) in axotomized Mb terminals (Lipin and Vigh, 2013). Therefore, the magnitude of depolarizing ramp evoked glutamate release appears to be comparable to that triggered by bright light stimuli from Mbs.

Consequences of NO-Mediated Weighted Potentiation for Glutamate Release From Mb

Terminals

Numerous neurotransmitters inhibit presynaptic I_{Ca} via G-protein coupled receptors by inducing changes in the voltage-dependence of I_{Ca} , resulting in channel activation at more depolarized potentials (Bean, 1989). Shifting the activation threshold of I_{Ca} to more depolarized potentials is an extremely potent way of reducing transmitter release (Catterall and Few, 2008), because of the power law of synaptic transmission (Katz and Miledi, 1970). Less is known about positive modulation of I_{Ca} by transmitters; to this end only the neurosteroid pregnenolone sulfate was shown to potentiate presynaptic release at the Calyx of Held by a mechanism which involved shifting I_{Ca} activation to the left (Hige et al., 2006). Despite of the extensive literature published on activity-dependent short- and long term synaptic plasticity in the CNS, to date only one reference described activity dependent positive modulation of presynaptic I_{Ca} activation: at the Calyx of Held synapse, tetanic stimulation shifted the half-activation voltage ($V_{1/2}$) of the

presynaptic I_{Ca} by -4.1 mV (Cuttle et al., 1998), analogous to our results. Although the underlying mechanism was not identified beyond establishing that it was independent of G-proteins, Cuttle et al. (1998) showed that a small shift in I_{Ca} activation to more negative potentials can significantly increase transmitter output from the presynaptic Calyx, which is entirely consistent with our data (Fig. 3.6A, 3.6C, 3.6F).

Although Mb terminals release glutamate at ribbon synapses, which are specialized to release transmitters continuously over long period and capable to code changes in illumination rather quickly (Sterling and Matthews, 2005; Thoreson, 2007), they are subject to short term synaptic plasticity known as paired pulse depression of glutamate release (von Gersdorff and Matthews, 1997). Activity-dependent long term potentiation of the BC \rightarrow GC synapse has also been shown in the developing zebrafish retina (Wei et al., 2012), although this phenomenon disappears with maturation. Activity-dependent short term potentiation of release seen at central synapses (Habets and Borst, 2006) from Mb or other BCs has not been reported so far. Importantly, the effect of the left-shifted I_{Ca} activation on the input-output ratio of Mbs is very unique: this weighted potentiation not only enhanced I_{Ca} triggered by weak inputs, but the enhancement gradually decreased as the input strength increased, limiting the potentiation to the physiologically relevant membrane potentiation range. The power law of synaptic transmission (Katz and Miledi, 1970) and the particularly high level of Ca^{2+} cooperativity in mediating release from Mb terminals (Heidelberger et al., 1994) further magnifies this phenomenon at the level of glutamate output from Mb terminals: NO-mediated increase of I_{Ca} resulted in increased exocytosis at -30 mV; however, the small (yet significant) increase in I_{Ca} amplitude at -20 mV did not cause consequent ΔC_m increase (Fig. 3.6D, 3.6F).

Intrinsic adaptation to luminance is mediated through synaptic depression of glutamate release from rod BCs (Oesch and Diamond, 2011), resulted by Ca^{2+} channel inactivation and vesicle depletion (Jarsky et al., 2011). It is unclear if the rod driven circuitry in the mammalian retina is subject to NO-mediated or other types of synaptic potentiation. Nonetheless, mammalian ON cone BCs show NO-dependent, cGMP-mediated weighted sensitization: upon NO donor exposure, their response to weak stimuli increased whereas responses to strong inputs remained unaltered (Snellman and Nawy, 2004). We discovered a novel form of activity dependent, NO-mediated synaptic plasticity expressed at the axon terminal of the rod-dominated Mb-type bipolar cell: it is triggered by large depolarization and through synaptic communication it causes positive modulation of voltage-gated Ca^{2+} channels, particularly in response to consecutive weak inputs. Because Mbs in the fish retina make direct synaptic contacts with GCs (Witkovsky and Dowling, 1969; Marc and Liu, 2000; Palmer, 2010), we propose that this novel mechanism enhances the representation of weak rod signals at Mb→GC synapses under bright scotopic and mesopic light conditions. The selective potentiation of weak signals may counter use-dependent depression of glutamate release from BCs during light adaptation and prevent the loss of critical visual information carried by dim scotopic signals.

4. Conclusion

The visual world is a dynamic environment full of variation as drastic as the difference between night and day or as subtle as the outline of individual blades of grass in a field. As the main sensory organ designed to process and translate visual information into neuronal signals, our retina must have the ability to adjust to this variation and do so on a spatial and temporal scale appropriate for the visual input. However, because the range of possible inputs significantly exceeds the output capabilities, the retina must adjust how it handles and processes certain signals. For example, as morning light intensity increases, the retina accommodates for the more intense stimuli by decreasing overall sensitivity, ultimately avoiding saturation (“adaptation”; Smirnakis et al., 1997; Kim and Rieke, 2001). Although beneficial in preventing saturation, this modulation of retinal circuitry introduces a new problem: if the dynamic range of vision is shifted to accommodate brighter, more intense light, then the retina may lose the ability to detect visual information carried by dim, weak light. Thus, it stands to reason that certain mechanisms exist within the retina with purpose of combatting the potential information loss during adaptation.

Intuitively, if a neuromodulator is responsible for modulating the retinal circuitry in opposition to adaptation, its release must be highly dependent upon light stimulation. Along these lines, in the retina, dopamine and nitric oxide (NO) are released in a light-dependent manner (Witkovsky, 2004; Sekaran et al., 2005). However, it is abundantly clear that dopamine functions to promote classical adaptation and desensitization of the retina (Witkovsky, 2004), leading us to consider the role of NO in combatting information loss during adaptation. Importantly, while NO signaling in the retina has been studied for decades (Vielma et al., 2012),

only the effects mediated by cGMP have been explored in great detail. Whether endogenous NO results in S-nitrosylation of retinal proteins is entirely unknown. Therefore, the purpose of this study was twofold: 1) provide an initial, comprehensive description of retinal S-nitrosylation, via endogenous NO, and determine if it exhibits a light-dependent nature; and 2) explore whether S-nitrosylation functionally alters visual information processing in the retina. In this concluding chapter, we broaden our discussion of the key findings from each study and attempt to place them in the context of neurodegenerative diseases affecting the CNS and retina.

4.1 S-nitrosylation Occurs Under Physiological Conditions in the Retina

By using a physiologically relevant stimulus (light) to evoke endogenous NO release, we were able to show strong evidence for the presence of S-nitrosylation in the healthy adult retina (Chapter 2). Using quantitative mass spectrometry, we provided the first descriptive account of retinal proteins that are subjected to light-evoked S-nitrosylation in the mammalian retina. Several proteins that we identified to be nitrosylated via light-evoked NO were also identified in other studies using NO donors (compare Table 2 from Chapter 2 to Stamler et al., 2001; Chen et al., 2010; Seth and Stamler, 2011). This agreement in data sets suggests that certain proteins theoretically determined to be nitrosylated (using exogenous donors) are, in fact, S-nitrosylated by endogenous NO under physiological conditions. Again, it must be reiterated that, although implied, protein nitrosylation does not necessarily result in a change in function. Nonetheless, for retinal neurobiologists, this descriptive account may open the door for new, functional studies that explore the role of S-nitrosylation on signal processing in the retina.

A foundational observation of this study was that there is significantly more S-nitrosylation in light-adapted retinas than in dark-adapted retinas. This observation was

supported by two strong lines of evidence: 1) in both mouse and goldfish retinas, SNI levels were dramatically increased in the light-adapted state when compared to the dark-adapted retinas; 2) the number of identified S-nitrosylated proteins was over 2 times greater in light-adapted retinas than in dark-adapted retinas (light: 351 proteins vs. dark: 154 proteins, via MS). This drastic difference in SNI between light-adapted states was completely in line with the fact that NO synthesis and release is highly coordinated with light stimulation (Donati et al., 1995; Neal et al., 1998; Sekaran et al., 2005; Eldred and Blute, 2005; Walter et al., 2014).

While we focused the majority of our attention on characterizing the light-evoked *increases* of S-nitrosylation as a function of light stimulation, it is important to note these increases were relative to the amount of S-nitrosylation that was present in the dark-adapted retina. The dark-adapted retina is not entirely void of activity and, in fact, NO production does not completely cease in the absence of light stimulation. Instead, NO synthesis remains at a constant, albeit minimal, rate that maintains a low, tonic level of NO in the retina (Sekaran et al., 2005; Walter et al., 2014). This sustained activity in the dark is most likely a result of glutamatergic input from OFF BCs (which depolarize and release glutamate in the absence of light) onto nNOS⁺ ACs (Pang et al., 2010). Even at minimal rates of NO production in the dark, we observed low levels of S-nitrosocysteine immunofluorescence in the dark-adapted retina. In the classical sense, dark-adaptation is viewed as a process that allows for recovery of retinal sensitivity in the absence of light stimulation (Hecht et al., 1937). Our results indicate that S-nitrosylation of select proteins in the dark-adapted retina may contribute to the process of dark adaptation and may influence overall retinal sensitivity. However, whether S-nitrosylation in the dark-adapted retina serves a significant cellular function is unknown and should be the focus of future studies.

Regulation of S-nitrosylation by Denitrosylation

As a reversible post-translational modification, the extent and duration that a protein is S-nitrosylated depends upon the interplay between nitrosylation and denitrosylation. Once a protein is nitrosylated, the nitrosothiol bond may be cleaved via enzymatic and/or non-enzymatic means. Very little is known about the physiological mechanisms of denitrosylation, but the effectiveness of denitrosylation appears to be determined by the accessibility of the nitrosothiol (Paige et al., 2008). Non-enzymatic means for the decomposition of nitrosothiols include exposure to UV light (Forrester et al., 2007), reducing agents (Jaffrey et al., 2001; Paige et al., 2008), or transition metal ions such as copper (Dicks and Williams, 1996). Additionally, two enzyme systems have emerged as the key players in enzymatic denitrosylation: the S-nitrosoglutathione reductase (GSNOR) system (which includes GSNOR and glutathione, GSH) and the thioredoxin (TRX) system (comprised of thioredoxin, Trx and thioredoxin reductase, TrxR) (Benhar et al., 2009). There is a noticeable lack of information regarding enzymatic denitrosylation in the retina, and our study (Chapter 2) focused on the formation of S-nitrosylation but not its removal. However, preliminary evidence indicates that in the mammalian retina, enzymatic denitrosylation is regulated by light stimulation (i.e. when the need for denitrosylation is at its peak).

Retinal homogenates from light- and dark-adapted mice (n=2 samples from 2 animals, each condition), containing equal amounts of protein, were analyzed using a global proteomics approach as described in the Methods section of Chapter 2, with the only difference being that we did not enrich the samples for S-nitrosylated proteins using the biotin-switch assay. Interestingly, we observed detectable levels of thioredoxin-1 (Trx1) protein only in the light-adapted mouse retina (peptide score for Trx1: light-adapted=5 vs. dark-adapted=0), providing the

initial observation of the light-dependent nature of denitrosylase expression. Furthermore, when dark-adapted eyecups were incubated in 200 nM auranofin (Tocris Biosciences) for 3 h to inhibit TrxR and prevent denitrosylation (Choi et al., 2011), we did not observe increased SNI above dark-adapted, baseline conditions (Fig. 4.1, compare with Fig. 2.2 from Chapter 2). These data indicate that the TRX system is not regulating S-nitrosylation in the absence of

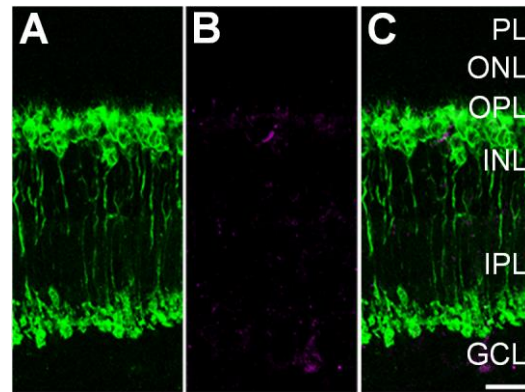


Figure 4.1. Inhibition of denitrosylation does not alter dark-adapted levels of SNI. 40X vertical cryostat section of a dark-adapted mouse retina animal treated with 200 nM auranofin for 3 hrs. **A:** PKC α + (green) RBCs. **B:** S-nitrosocysteine (magenta), **B, C:** Merged confocal image showing minimal S-nitrosocysteine immunofluorescence, similar to the control dark-adapted mouse retina (**Fig. 2.2, bottom panel**). Scale bar=20 μ m.

light. Interestingly, expression of Trx has been shown to be upregulated in response to NO (Andoh et al., 2003; Hromatka et al., 2005) and activity of the TRX system has been correlated with NMDA receptor activity (Papadia et al., 2008) that triggers NOS-dependent S-nitrosylation (Fang et al., 2000). Considering the inducible nature of the TRX system, these preliminary data suggest that mechanisms of denitrosylation, in the mammalian retina, are activated following light stimulation when the levels of S-nitrosylated proteins are elevated. Further studies exploring the role and mechanism of denitrosylation in the vertebrate retina could add significantly to our understanding of how S-nitrosylation is modulating visual information processing.

4.2 S-nitrosylation Mediates Weighted Potentiation of Mb Output in the Goldfish Retina

In Chapter 3, we described a novel NO-dependent modulatory mechanism that alters glutamate release from the Mb terminal in the goldfish retina. We show that activity-dependent

retrograde transmission of NO enhances the output of Mbs in a selective manner so that only weak or dim responses are potentiated. However, the lingering question remains: what is the target of S-nitrosylation in the Mb terminal that results in the observed effects of NO? Here we present preliminary evidence suggesting a putative target of S-nitrosylation in the Mb terminal and discuss the potential implications.

GAPDH: Potential Target of S-nitrosylation in the Mb Terminal

Although nearly a thousand proteins with potential S-nitrosylation sites have been identified (Seth and Stamler, 2011), one particular protein that is known to alter cellular function upon S-nitrosylation is the glycolytic enzyme glyceraldehyde-3-phosphate dehydrogenase (GAPDH; Jaffery et al., 2001; Hara and Snyder, 2006). In the CNS, GAPDH is nitrosylated via NO from NMDA-dependent activation of nNOS (Hara and Snyder, 2006). Interestingly, S-nitrosylated GAPDH (SNO-GAPDH) can engage in transnitrosylation, a process characterized by direct thiol to thiol transfer of the NO molecule to other proteins (Kornberg et al., 2010), and can alter protein function in the cytosol (Nakamura et al., 2013). Based on these reports and the wide array of functions that continue to be attributed to S-nitrosylation of GAPDH, we were curious to determine if SNO-GAPDH was playing a role in modulating Mb terminal I_{Ca} dynamics.

Using similar methods as described in Chapter 3, we recorded ramp-evoked I_{Ca} I-Vs from axotomized Mb terminals in goldfish retinal slice preparation. To address whether S-nitrosylation of GAPDH was involved in mediating the leftward shift in the activation threshold of I_{Ca} (See Fig. 3.2), we included CGP3466B (10 nM, Tocris Bioscience), a potent inhibitor of GAPDH nitrosylation (Xu et al., 2013), in the recording solution. CGP3466B prevented the

leftward shift of I_{Ca} during consecutive voltage ramps in axotomized Mb terminals in retinal slice (Fig. 4.2). On average, $V_{(5\%)}$ was -37.5 ± 1.44 mV for control and -38.0 ± 2.04 mV for the second ramp I-V, $V_{(50\%)}$ was -21.3 ± 1.38 mV for control and -21.4 ± 0.83 mV for the second ramp I-V, and $V_{(Max)}$ was -6.0 ± 2.68 mV for control and -4.8 ± 2.32 mV for the second ramp I-V. Statistical analysis determined no significant difference in $V_{(5\%)}$, $V_{(50\%)}$, and $V_{(Max)}$ between the control and second ramp evoked I_{Ca} I-Vs ($p=0.3$, $p=0.3$, and $p=0.4$, respectively, paired Student's t test, $n=4$).

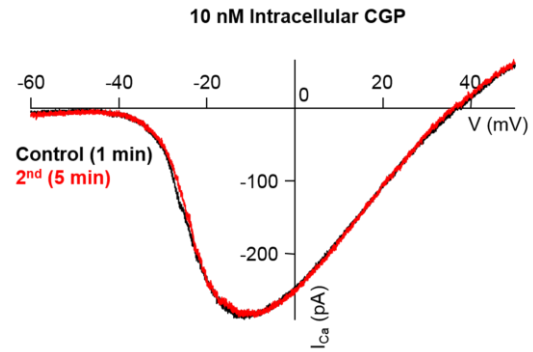


Figure 4.2. S-nitrosylation of GAPDH appears to be required for modulation of I_{Ca} . Consecutive I_{Ca} traces recorded from an axotomized Mb terminal in slice preparation in response to voltage ramps 4 min apart in the presence of intracellular CGP3466B (10 nM). CGP prevents GAPDH S-nitrosylation and subsequently prevented the leftward shift of the second ramp I-V (red) as compared to the control ramp I-V (black).

Recently, GAPDH has been included in a classification of proteins called nitrosylases that appear to facilitate the S-nitrosylation of other proteins, primarily through transnitrosylation (Anand and Stamler, 2012). Nitrosylases play an important role in modulating protein and cellular function by transporting and delivering NO in a directed manner to specific proteins. In this way, it appears that there is some sort of regulation over the S-nitrosylation of proteins. With this in mind, our preliminary data may indicate that GAPDH is playing a role as a nitrosylase within the Mb terminal and directing S-nitrosylation of a specific protein (or proteins) that in turn, modulates the function of the L-type calcium channel. If GAPDH is acting as a nitrosylase, this may account for why the observed results, on I_{Ca} , happen on a time scale of minutes. The exact route by which GAPDH is modulating I_{Ca} is still unknown, however, it may be transnitrosylating the L-type calcium channel itself. Importantly, evidence has implicated direct

S-nitrosylation of L-type calcium channels, independent of any influence by cGMP, kinases, and/or phosphatases, resulting in modulation of I_{Ca} similar to our results (Campbell et al., 1996; Jian et al., 2007). However, these conclusions of “direct nitrosylation” are based on process of elimination of other contributing factors and, to date, no study has definitively shown direct S-nitrosylation of L-type calcium channels along with associated functional changes. To that point, in our MS data, we did not identify any calcium channel subunits among the S-nitrosylated proteins from light-adapted retinas.

4.3 S-nitrosylation in Neurodegenerative Diseases

Under physiological conditions, clear and precise detection of endogenously S-nitrosylated proteins has been relatively difficult, until recently, due to their low abundance and the sensitivity of the detection methods (Jaffrey et al., 2001; Chapter 2). However, S-nitrosylated proteins are abundant in several neurodegenerative disorders and therefore were easily detectable (Nakamura et al., 2013), which inevitably led to S-nitrosylation being primarily associated with pathological conditions within the CNS. Accumulating evidence in recent years suggests that aberrant S-nitrosylation is playing a role in the progression of neurodegenerative diseases, such as Parkinson’s and Alzheimer’s (Forrester et al., 2006; Foster et al., 2009; Anand and Stamler, 2012). Furthermore, aberrant S-nitrosylation may influence the progression of both the sporadic and genetic forms of certain neurodegenerative disorders (Nakamura et al., 2013). While we have presented strong evidence for a physiological role for S-nitrosylation in “healthy” nervous tissue, this final concluding section will focus on the contribution of S-nitrosylation to the pathogenesis of neurodegenerative diseases in the CNS and in the retina.

Whether NO exhibits neuroprotective or neurodegenerative effects is relatively controversial, although it appears to be entirely dependent on the immediate NO concentration. For instance, at low or moderate levels NO is neuroprotective, but it becomes toxic at higher concentrations (Nakamura et al., 2013). For example, NO can mediate neuroprotective effects via S-nitrosylation of the NR2 subunit of NMDA receptors (NMDARs, Choi et al., 2000). Here, S-nitrosylation inhibits current flow through NMDARs, which can protect the cell from excessive activity and the system from further NMDA-dependent NO production (Choi et al., 2000). However, the concentration of NO that facilitates neuroprotective S-nitrosylation is still unclear. Importantly in our MS data, we did not detect the NR2 NMDAR subunit (or any other NMDAR subunit, for that matter) in our identified S-nitrosylated proteins (Table 2.2; Appendix II), indicating that physiological levels of NO are not sufficient to induce neuroprotective S-nitrosylation.

Neurodegenerative effects, on the other hand, are associated with persistent activation of NOS, which leads to aberrantly high levels of NO and S-nitrosylation of proteins involved in neuronal cell death (Forrester et al., 2006; Anand and Stamler, 2012). For example, excessive NO production and the subsequent S-nitrosylation of GAPDH, Parkin, peroxiredoxin 2 and protein disulfide isomerase have all been implicated in the etiology of Parkinson's disease (Forrester et al., 2006; Foster et al., 2009; Nakamura et al., 2013). Furthermore, disruption of the denitrosylation system may accompany neurodegenerative diseases, which in combination with excessive NO production, would lead to extensive, unregulated protein S-nitrosylation (Benhar et al., 2009; Anand and Stamler et al., 2012). Thus, at low or even moderate levels, NO may be neuroprotective, but when the concentration of NO surpasses an unknown threshold, unregulated S-nitrosylation can induce neuronal cell death and contribute to neurodegenerative diseases.

The Role of NO in Retinal Degeneration

In the retina, aberrantly high levels of NO are associated with devastating, sight-threatening diseases, such as glaucoma and diabetic retinopathy (Toda and Toda, 2007; Cavet et al., 2014), as well as general conditions of retinal excitotoxicity (Vorwerk et al., 1997). Glaucoma, diabetic retinopathy and retinal excitotoxicity are associated with GC death and optic nerve damage which ultimately leads to the loss of vision (Kern and Barber, 2008; Cavet et al., 2014). While the mechanism is not yet known, high levels of NO appear to correlate directly with GC death: in mammalian models of glaucoma, inhibition of iNOS, which is upregulated under pathological conditions and contributes to the elevated levels of NO (Neufeld, 1999), and nNOS significantly reduced GC death (Neufeld et al., 1999; Chen et al., 2013). Furthermore, intravitreal injection of an NO donor induced retinal neurotoxicity and GC death in rats (Takahata et al., 2003). The connection between elevated levels of NO and GC death is unknown, recently however, S-nitrosylation has been shown to mediate GC death following NMDA induced excitotoxicity (Manabe et al., 2005).

In the diseased retina, aberrant levels of NO could contribute to GC death by nitrosylating a number of proteins that ultimately lead to neurodegeneration. In addition to functioning as a nitrosylase under normal, physiological conditions, GAPDH can also participate in neuronal degeneration when aberrantly nitrosylated, as mentioned above. GAPDH, upon S-nitrosylation, binds with an E3 ubiquitin ligase siah-1 and the two proteins translocate into the nucleus and initiate apoptosis (Hara and Snyder, 2006; Xu et al., 2013). While in the nucleus, GAPDH can act as a transnitrosylase and elicit nitrosylation of nuclear proteins such as deacetylating enzyme sirtuin-1 (SIRT1), histone deacetylase-2 (HDAC2) and DNA-activated protein kinase (DNA-PK) (Kornberg et al., 2010), which may lead to neurodegeneration

(Nakamura et al., 2013). In the retina, nuclear translocation of GAPDH has been observed as a result of streptozotocin-induced diabetic retinopathy (Kanwar and Kowluru, 2009) and furthermore, hyperglycemic conditions have induced retinal cell death due to translocation of the GAPDH/siah-1 complex to the nucleus of mouse and human Müller (glial) cells (Yego and Mohr, 2010). However, these studies did not explicitly show S-nitrosylation of GAPDH, the required step prior to GAPDH interacting with siah-1 and nuclear translocation (Hara and Snyder, 2006). Thus, a key link between elevated levels of NO and retinal cell degeneration may be S-nitrosylation of GAPDH, or similar proteins, which ultimately results in apoptosis of ganglion cells. An important area for future research is determining if GC death associated with elevated levels of NO in retinal diseases, like glaucoma, is a result of S-nitrosylated GAPDH.

4.4 Final Remarks

In this study, we have provided the first, comprehensive account of S-nitrosylation under physiological conditions in the retina and described a mechanism by which it alters visual information processing. We propose that these findings will not only lead to a greater understanding as to the complexity of retinal circuit modulation but will also provide the framework for future studies to explore the role of S-nitrosylation in retinal degenerative diseases. Finally, exploring the therapeutic potential of agents that affect S-nitrosylation could lead to innovative treatments for retinal diseases like glaucoma and diabetic retinopathy as well as other neurodegenerative diseases associated with aberrant S-nitrosylation.

References

- Ahern GP, Klyachko VA, Jackson MB (2002) cGMP and S-nitrosylation: two routes for modulation of neuronal excitability by NO. *Trends Neurosci* 25:510-517.
- Akopian A, Atlasz T, Pan F, Wong S, Zhang Y, Volgyi B, Paul DL, Bloomfield SA (2014) Gap Junction-Mediated Death of Retinal Neurons Is Connexin and Insult Specific: A Potential Target for Neuroprotection. *J Neurosci* 34:10582-10591.
- Alderton WK, Cooper CE, Knowles RG (2001) Nitric oxide synthases: structure, function and inhibition. *Biochem J* 357:593-615.
- Anand P, Stamler JS (2012) Enzymatic mechanisms regulating protein S-nitrosylation: implications in health and disease. *J Mol Med* 90:233-244.
- Andoh T, Chiueh CC, Chock PB (2003) Cyclic GMP-dependent protein kinase regulates the expression of thioredoxin and thioredoxin peroxidase-1 during hormesis in response to oxidative stress-induced apoptosis. *J Bio Chem* 278:885-890.
- Asari H, Meister M (2012) Divergence of visual channels in the inner retina. *Nat Neurosci* 15:1581-1589.
- Ayoub GS, Matthews G (1992) Substance-P modulates calcium current in retinal bipolar neurons. *Vis Neurosci* 8:539-544.
- Baccus SA, Meister M (2002) Fast and slow contrast adaptation in retinal circuitry. *Neuron* 36:909-919.
- Baden T, Berens P, Bethge M, Euler T (2013a) Spikes in mammalian bipolar cells support temporal layering of the inner retina. *Curr Biol* 23:48-52.

- Baden T, Esposti F, Nikolaev A, Lagnado L (2011) Spikes in retinal bipolar cells phase-lock to visual stimuli with millisecond precision. *Curr Biol* 21:1859-1869.
- Baden T, Euler T, Weckström M, Lagnado L (2013b) Spikes and ribbon synapses in early vision. *Trends Neurosci* 36:480-488.
- Baylor DA, Lamb TD, Yau KW (1979) Responses of retinal rods to single photons. *J Physiol (Lond)* 288:613-634.
- Baldrige WH, Fischer AJ (2001) Nitric oxide donor stimulated increase of cyclic GMP in the goldfish retina. *Vis Neurosci* 18:849-856.
- Bean BP (1989) Neurotransmitter inhibition of neuronal calcium currents by changes in channel voltage dependence. *Nature* 340:153-156.
- Benhar M, Forrester MT, Stamler JS (2009) Protein denitrosylation: enzymatic mechanisms and cellular functions. *Nat Rev Mol Cell Bio* 10:721-732.
- Bing YE, Du JL, Yang XL (1997) Differential effects of nitric oxide on rod and cone pathways in carp retina. *Sci China C Life Sci* 40:71-78.
- Blom JJ, Blute TA, Eldred WD (2009) Functional localization of the nitric oxide/cGMP pathway in the salamander retina. *Vis Neurosci* 26:275-286.
- Bloomfield SA, Dacheux RF (2001) Rod vision: Pathways and processing in the mammalian retina. *Prog Retinal Eye Res* 20:351-384.
- Blute TA, Mayer B, Eldred WD (1997) Immunocytochemical and histochemical localization of nitric oxide synthase in the turtle retina. *Vis Neurosci* 14:717-729.
- Blute TA, Velasco P, Eldred WD (1998) Functional localization of soluble guanylate cyclase in turtle retina: Modulation of cGMP by nitric oxide donors. *Vis Neurosci* 15:485-498.

- Bolotina VM, Najibi S, Palacino JJ, Pagano PJ, Cohen RA (1994) Nitric-oxide directly activates calcium-dependent potassium channels in vascular smooth-muscle. *Nature* 368:850-853.
- Bolte S, Cordelières FP (2006) A guided tour into subcellular colocalization analysis in light microscopy. *J Microsc-Oxford* 224:213-232.
- Boycott BB, Kolb H (1973) Connections between bipolar cells and photoreceptors in retina of domestic cat. *J Comp Neurol* 148:91-114.
- Boycott BB, Dowling JE, Kolb H (1969) Organization of primate retina - light microscopy - a second type of midget bipolar cell in primate retina. *Philos Trans R Soc Lond B Biol Sci* 255:109-184.
- Burrone J, Neves G, Gomis A, Cooke A, Lagnado L (2002) Endogenous calcium buffers regulate fast exocytosis in the synaptic terminal of retinal bipolar cells. *Neuron* 33:101-112.
- Busskamp V, Duebel J, Balya D, Fradot M, Viney TJ, Siegert S, Groner AC, Cabuy E, Forster V, Seeliger M, Biel M, Humphries P, Paques M, Mohand-Said S, Trono D, Deisseroth K, Sahel JA, Picaud S, Roska B (2010) Genetic reactivation of cone photoreceptors restores visual responses in retinitis pigmentosa. *Science* 329:413-417.
- Campbell DL, Stamler JS, Strauss HC (1996) Redox modulation of L-type calcium channels in ferret ventricular myocytes - Dual mechanism regulation by nitric oxide and S-nitrosothiols. *J Gen Phys* 108:277-293.
- Catterall WA, Few AP (2008) Calcium channel regulation and presynaptic plasticity. *Neuron* 59:882-901.
- Cavet ME, Vittitow JL, Impagnatiello F, Ongini E, Bastia E (2014) Nitric Oxide (NO): An Emerging Target for the Treatment of Glaucoma. *Invest Ophth Vis Sci* 55:5005-5015.

- Chakrabarti S, Lekontseva O, Peters A, Davidge ST (2010) 17 beta-Estradiol induces protein S-nitrosylation in the endothelium. *Cardiovasc Res* 85:796-805.
- Chen C, Xu Y, Zhang J, Zhu J, Zhang J, Hu N, Guan H (2013) Altered Expression of nNOS/NIDD in the Retina of a Glaucoma Model of DBA/2J Mice and the Intervention by nNOS Inhibition. *J Mol Neurosci* 51:47-56.
- Choi YB, Tenneti L, Le DA, Ortiz J, Bai G, Chen HSV, Lipton SA (2000) Molecular basis of NMDA receptor-coupled ion channel modulation by S-nitrosylation. *Nat Neurosci* 3:15-21.
- Chun MH, Oh SJ, Kim IB, Kim KY (1999) Light and electron microscopical analysis of nitric oxide synthase-like immunoreactive neurons in the rat retina. *Vis Neurosci* 16:379-389.
- Chung KK, Thomas B, Li XJ, Pletnikova O, Troncoso JC, Marsh L, Dawson VL, Dawson TM (2004) S-nitrosylation of Parkin regulates ubiquitination and compromises Parkin's protective function. *Science* 304:1328-1331.
- Cuttle MF, Tsujimoto T, Forsythe ID, Takahashi T (1998) Facilitation of the presynaptic calcium current at an auditory synapse in rat brainstem. *J Physiol (Lond)* 512:723-729.
- Damodaran VB, Place LW, Kipper MJ, Reynolds MM (2012) Enzymatically degradable nitric oxide releasing S-nitrosated dextran thiomers for biomedical applications. *J Mater Chem* 22:23038-23048.
- Daniels BA, Baldrige WH (2011) The light-induced reduction of horizontal cell receptive field size in the goldfish retina involves nitric oxide. *Vis Neurosci* 28:137-144.
- Dawson TM, Brecht DS, Fotuhi M, Hwang PM, Snyder SH (1991) Nitric-oxide synthase and neuronal NADPH diaphorase are identical in brain and peripheral-tissues. *Proc Natl Acad Sci U S A* 88:7797-7801.

- Demb JB (2002) Multiple mechanisms for contrast adaptation in the retina. *Neuron* 36:781-783.
- Demb JB (2008) Functional circuitry of visual adaptation in the retina. *J Physiol (Lond)* 586:4377-4384.
- DeVries SH (2000) Bipolar cells use kainate and AMPA receptors to filter visual information into separate channels. *Neuron* 28:847-856.
- Devries SH, Schwartz EA (1989) Modulation of an electrical synapse between solitary pairs of catfish horizontal cells by dopamine and second messengers. *J Physiol (Lond)* 414:351-375.
- Dicks AP, Williams DLH (1996) Generation of nitric oxide from S-nitrosothiols using protein-bound Cu^{2+} sources. *Chem Biol* 3:655-659.
- Donati G, Pournaras CJ, Munoz JL, Poitry S, Poitryamate CL, Tsacopoulos M (1995) Nitric oxide controls arteriolar tone in the retina of the miniature pig. *Invest Ophth Vis Sci* 36:2228-2237.
- Dowling JE (1987) *The retina: an approachable part of the brain*. Cambridge, MA: Belknap Press.
- Dreosti E, Esposti F, Baden T, Lagnado L (2011) In vivo evidence that retinal bipolar cells generate spikes modulated by light. *Nat Neurosci* 14:951-952.
- Eldred WD, Blute TA (2005) Imaging of nitric oxide in the retina. *Vision Res* 45:3469-3486.
- Euler T, Schneider H, Wassle H (1996) Glutamate responses of bipolar cells in a slice preparation of the rat retina. *J Neurosci* 16:2934-2944.
- Euler T, Haverkamp S, Schubert T, Baden T (2014) Retinal bipolar cells: elementary building blocks of vision. *Nat Rev Neurosci* 15:507-519.

- Fang M, Jaffrey SR, Sawa A, Ye KQ, Luo XJ, Snyder SH (2000) Dexas1: A G protein specifically coupled to neuronal nitric oxide synthase via CAPON. *Neuron* 28:183-193.
- Feng Y, Yu S, Lasell TKR, Jadhav AP, Macia E, Chardin P, Melancon P, Roth M, Mitchison T, Kirchhausen T (2003) Exo1: A new chemical inhibitor of the exocytic pathway. *Proc Natl Acad Sci USA* 100:6469-6474.
- Forrester MT, Benhar M, Stamler JS (2006) Nitrosative stress in the ER: A new role for S-nitrosylation in Neurodegenerative diseases. *Acs Chem Bio* 1:355-358.
- Forrester MT, Foster MW, Stamler JS (2007) Assessment and application of the biotin switch technique for examining protein S-nitrosylation under conditions of pharmacologically induced oxidative stress. *J Biol Chem* 282:13977-13983.
- Foster MW, Hess DT, Stamler JS (2009) Protein S-nitrosylation in health and disease: a current perspective. *Trends Mol Med* 15:391-404.
- Gallagher SK, Witkovsky P, Roux MJ, Low MJ, Otero-Corchon V, Hentges ST, Vigh J (2010) beta-Endorphin Expression in the Mouse Retina. *J Comp Neurol* 518:3130-3148.
- Gillis KD (2000) Admittance-based measurement of membrane capacitance using the EPC-9 patch-clamp amplifier. *Pflugers Arch* 439:655– 664.
- Garthwaite J (1985) Cellular uptake disguises action of l-glutamate on n-methyl-d-aspartate receptors - with an appendix - diffusion of transported amino-acids into brain-slices. *Brit J Pharmacol* 85:297-307.
- Garthwaite J (2008) Concepts of neural nitric oxide-mediated transmission. *European J Neurosci* 27:2783-2802.

- Garthwaite J, Charles SL, Chesswilliams R (1988) Endothelium-derived relaxing factor release on activation of nmda receptors suggests role as intercellular messenger in the brain. *Nature* 336:385-388.
- Giove TJ, Deshpande MM, Eldred WD (2009) Identification of alternate transcripts of neuronal nitric oxide synthase in the mouse retina. *J Neurosci Res* 87:3134-3142.
- Gollisch T, Meister M (2008) Rapid neural coding in the retina with relative spike latencies. *Science* 319:1108-1111.
- Gotzes S, de Vente J, Muller F (1998) Nitric oxide modulates cGMP levels in neurons of the inner and outer retina in opposite ways. *Vis Neurosci* 15:945-955.
- Goureau O, Regnier-Ricard F, Courtois Y (1999) Requirement for nitric oxide in retinal neuronal cell death induced by activated Muller glial cells. *J Neurochem* 72:2506-2515.
- Greferath U, Grunert U, Wassle H (1990) Rod bipolar cells in the mammalian retina show protein kinase-c-like immunoreactivity. *J Comp Neurol* 301:433-442.
- Griguer C, Fuchs PA (1996) Voltage-dependent potassium currents in cochlear hair cells of the embryonic chick. *J Neurophysiol* 75:508-513.
- Gyurko R, Leupen S, Huang PL (2002) Deletion of exon 6 of the neuronal nitric oxide synthase gene in mice results in hypogonadism and infertility. *Endocrinology* 143:2767-2774.
- Habets RLP, Borst JGG (2006) An increase in calcium influx contributes to post-tetanic potentiation at the rat calyx of held synapse. *J Neurophysiol* 96:2868-2876.
- Handy RL, Harb HL, Wallace P, Gaffen Z, Whitehead KJ, Moore PK (1996) Inhibition of nitric oxide synthase by 1-(2-trifluoromethylphenyl) imidazole (TRIM) in vitro: Antinociceptive and cardiovascular effects. *Brit J Pharmacol* 119:423-431.

- Hardingham N, Dachtler J, Fox K (2013) The role of nitric oxide in pre-synaptic plasticity and homeostasis. *Front Cell Neurosci* 7.
- Hara MR, Snyder SH (2006) Nitric oxide-GAPDH-Siah: A novel cell death cascade. *Cell Mol Neurobiol* 26:527-538.
- Haverkamp S, Kolb H, Cuenca N (1999) Endothelial nitric oxide synthase (eNOS) is localized to Müller cells in all vertebrate retinas. *Vision Res* 39:2299-2303.
- Haverkamp S, Specht D, Majumdar S, Zaidi NF, Brandstätter JH, Wasco W, Wässle H, Tom Dieck S (2008) Type 4 OFF cone bipolar cells of the mouse retina express calsenilin and contact cones as well as rods. *J Comp Neurol* 507:1087-1101.
- Haverkamp S, Wässle H (2000) Immunocytochemical analysis of the mouse retina. *J Comp Neurol* 424:1-23.
- Hayashida Y, Rodríguez CV, Ogata G, Partida GJ, Oi H, Stradleigh TW, Lee SC, Colado AF, Ishida AT (2009) Inhibition of adult rat retinal ganglion cells by D1-type dopamine receptor activation. *J Neurosci* 29:15001-15016.
- Hecht S, Haig C, Chase AM (1937) The influence of light adaptation on subsequent dark adaptation of the eye. *J Gen Phys* 20:831-850.
- Heidelberger R, Heinemann C, Neher E, Matthews G (1994) Calcium-dependence of the rate of exocytosis in a synaptic terminal. *Nature* 371:513-515.
- Heidelberger R, Matthews G (1992) Calcium influx and calcium current in single synaptic terminals of goldfish retinal bipolar neurons. *J Physiol* 447:235-256.
- Henry D, Burke S, Shishido E, Matthews G (2003) Retinal bipolar neurons express the cyclic nucleotide-gated channel of cone photoreceptors. *J Neurophysiol* 89:754-761.

- Hess DT, Matsumoto A, Kim SO, Marshall HE, Stamler JS (2005) Protein S-nitrosylation: Purview and parameters. *Nat Rev Mol Cell Bio* 6:150-166.
- Hige T, Fujiyoshi Y, Takahashi T (2006) Neurosteroid pregnenolone sulfate enhances glutamatergic synaptic transmission by facilitating presynaptic calcium currents at the calyx of Held of immature rats. *European J Neurosci* 24:1955-1966.
- Hille B (2001) Voltage-dependent gates have gating charge and gating current. In: *Ion channels of excitable membranes*. pp 56-59. Sunderland, MA: Sinauer Associates, Inc.
- Hirasawa H, Kaneko A (2003) pH changes in the invaginating synaptic cleft mediate feedback from horizontal cells to cone photoreceptors by modulating Ca²⁺ channels. *J Gen Physiol* 122:657-671.
- Hirooka K, Kourennyi DE, Barnes S (2000) Calcium channel activation facilitated by nitric oxide in retinal ganglion cells. *J Neurophysiol* 83:198-206.
- Hoffpauir B, McMains E, Gleason E (2006) Nitric oxide transiently converts synaptic inhibition to excitation in retinal amacrine cells. *J Neurophys* 95:2866-2877.
- Hrabie JA, Klose JR, Wink DA, Keefer LK (1993) New nitric oxide-releasing zwitterions derived from polyamines. *J Org Chem* 58:1472-1476.
- Hromatka BS, Noble SM, Johnson AD (2005) Transcriptional response of *Candida albicans* to nitric oxide and the role of the YHB1 gene in nitrosative stress and virulence. *Mol Biol Cell* 16:4814-4826.
- Hu S-Q, Ye J-S, Zong Y-Y, Sun C-C, Liu D-H, Wu Y-P, Song T, Zhang G-Y (2012) S-Nitrosylation of Mixed Lineage Kinase 3 Contributes to Its Activation after Cerebral Ischemia. *J Bio Chem* 287:2364-2377.

- Jaffrey SR, Erdjument-Bromage H, Ferris CD, Tempst P, Snyder SH (2001) Protein S-nitrosylation: a physiological signal for neuronal nitric oxide. *Nat Cell Bio* 3:193-197.
- Jarsky T, Cembrowski M, Logan SM, Kath WL, Riecke H, Demb JB, Singer JH (2011) A synaptic mechanism for retinal adaptation to luminance and contrast. *J Neurosci* 31:11003-11015.
- Jeon CJ, Strettoi E, Masland RH (1998) The major cell populations of the mouse retina. *J Neurosci* 18:8936-8946.
- Jian K, Chen M, Cao X, Zhu X-H, Fung M-L, Gao T-M (2007) Nitric oxide modulation of voltage-gated calcium current by S-nitrosylation and cGMP pathway in cultured rat hippocampal neurons. *Biochem Biophys Res Comm* 359:481-485.
- Joselevitch C, Kamermans M (2007) Interaction between rod and cone inputs in mixed-input bipolar cells in goldfish retina. *J Neurosci Res* 85:1579-1591.
- Joselevitch C, Kamermans M. (2009) Retinal parallel pathways: seeing with our inner fish. *Vision Res* 49:943-959.
- Kaneko A, Tachibana M (1985) A voltage-clamp analysis of membrane currents in solitary bipolar cells dissociated from *Carassius auratus*. *J Physiol* 358:131-152.
- Kastner DB, Baccus SA (2011) Coordinated dynamic encoding in the retina using opposing forms of plasticity. *Nat Neurosci* 14:1317-1135.
- Katz B, Miledi R (1970) Further study of the role of calcium in synaptic transmission. *J Physiol* 207:789-801.
- Kawai F, Sterling P. 2002. cGMP modulates spike responses of retinal ganglion cells via a cGMP-gated current. *Vis Neurosci* 19:373-380.
- Kern TS, Barber AJ (2008) Retinal ganglion cells in diabetes. *J Phys(Lond)* 586:4401-4408.

- Kim IB, Lee EJ, Kim KY, Ju WK, Oh SJ, Joo CK, Chun MH (1999) Immunocytochemical localization of nitric oxide synthase in the mammalian retina. *Neurosci Lett* 267:193-196.
- Kim KJ, Rieke F (2001) Temporal contrast adaptation in the input and output signals of salamander retinal ganglion cells. *J Neurosci* 21:287-299.
- Klumpp DJ, Song EJ, Ito S, Sheng MH, Jan LY, Pinto LH (1995) The shaker-like potassium channels of the mouse rod bipolar cell and their contributions to the membrane current. *J Neurosci* 15:5004-5013.
- Knowles RG, Moncada S (1994) Nitric-oxide synthases in mammals. *Biochem J* 298:249-258.
- Kornberg MD, Sen N, Hara MR, Juluri KR, Nguyen JVK, Snowman AM, Law L, Hester LD, Snyder SH (2010) GAPDH mediates nitrosylation of nuclear proteins. *Nat Cell Bio* 12:1094-U1089.
- Krizaj D (2000) Mesopic state: Cellular mechanisms involved in pre- and post-synaptic mixing of rod and cone signals. *Microsc Res Tech* 50:347-359.
- Kurenny DE, Moroz LL, Turner RW, Sharkey KA, Barnes S (1994) Modulation of ion channels in rod photoreceptors by nitric-oxide. *Neuron* 13:315-324.
- Lasansky A (1973) Organization of outer synaptic layer in retina of larval tiger salamander. *Philos Trans R Soc Lond B Biol Sci* 265:471-89.
- Lee SJ, Lee JR, Kim YH, Park YS, Park SI, Park HS, Kim KP (2007) Investigation of tyrosine nitration and nitrosylation of angiotensin II and bovine serum albumin with electrospray ionization mass spectrometry. *Rapid Commun Mass Spectrom* 21:2797-2804.
- Leuranguer V, Dirksen RT, Beam KG (2003) Potentiated L-type Ca²⁺ channels rectify. *J Gen Physiol* 121:541-550.
- Li Y, Schlamp CL, Nickells RW (1999) Experimental induction of retinal ganglion cell death in adult mice. *Invest Ophthalmol Vis Sci* 40:1004-1008.

- Liepe BA, Stone C, Koistinaho J, Copenhagen DR. (1994) Nitric-oxide synthase in müller cells and neurons of salamander and fish retina. *J Neurosci* 14:7641-7654.
- Lipin M and Vigh J (2013) Quantifying the effect of light activated outer and inner retinal inhibitory pathways on exocytosis from mixed bipolar cells. ARVO meeting, Seattle WA, Invest Ophthalmol Vis Sci; 540: E-Abstract 6155.
- Loew ER and McFarland WN (1990) The underwater visual environment. In: *The visual system of fish* (Douglas RH and Djamgoz MBA, eds.), pp1-43. New York, NY: Chapman and Hall.
- Logiudice L, Henry D, Matthews G (2006) Identification of calcium channel alpha1 subunit mRNA expressed in retinal bipolar neurons. *Mol Vis* 12:184-189.
- Lu CB, McMahon DG (1997) Modulation of hybrid bass retinal gap junctional channel gating by nitric oxide. *J Physiol* 499:689-699.
- Manabe S, Gu ZZ, Lipton SA (2005) Activation of matrix metalloproteinase-9 via neuronal nitric oxide synthase contributes to NMDA-induced retinal ganglion cell death. *Invest Ophth Vis Sci* 46:4747-4753.
- Manookin MB, Demb JB (2006) Presynaptic mechanism for slow contrast adaptation in mammalian retinal ganglion cells. *Neuron* 50:453-464.
- Maragos CM, Morley D, Wink DA, Dunams TM, Saavedra JE, Hoffman A, Bove AA, Isaac L, Hrabie JA, Keefer LK (1991) Complexes of .NO with nucleophiles as agents for the controlled biological release of nitric oxide. Vasorelaxant effects. *J Med Chem* 34:3242-4247.

- Marc RE, Liu W (2000) Fundamental GABAergic amacrine cell circuitries in the retina: nested feedback, concatenated inhibition, and axosomatic synapses. *J Comp Neurol* 425: 560-582.
- Marty A and Neher E (1995) Tight-seal whole-cell recording. In: *Single-channel recording* (Sakmann B and Neher E eds.) pp.31-52. New York, NY: Plenum Press.
- Masland RH (2001) The fundamental plan of the retina. *Nat Neurosci* 4:877-886.
- Masland RH (2012a) The Neuronal Organization of the Retina. *Neuron* 76:266-280.
- Masland RH (2012b) The tasks of amacrine cells. *Vis Neurosci* 29:3-9.
- Masu M, Iwakabe H, Tagawa Y, Miyoshi T, Yamashita M, Fukuda Y, Sasaki H, Hiroi K, Nakamura Y, Shigemoto R, Takada M, Nakamura K, Nakao K, Katsuki M, Nakanishi S (1995) Specific deficit of the on response in visual transmission by targeted disruption of the mGluR6 gene. *Cell* 80:757-765.
- McFarland WN, Munz FW (1975) Part II: The photic environment of clear tropical seas during the day. *Vision Res* 15:1063-1070.
- McMahon DG, Ponomareva LV (1996) Nitric oxide and cGMP modulate retinal glutamate receptors. *J Neurophysiol* 76:2307-2315.
- Mennerick S, Matthews G (1998) Rapid calcium-current kinetics in synaptic terminals of goldfish retinal bipolar neurons. *Vis Neurosci* 15:1051-1056.
- Mennerick S, Zenisek D, Matthews G (1997) Static and dynamic membrane properties of large-terminal bipolar cells from goldfish retina: experimental test of a compartment model. *J Neurophysiol* 78:51-62.
- Mills SL, Massey SC (1995) Differential properties of 2 gap junctional pathways made by AII amacrine cells. *Nature* 377:734-737.

- Miyagi M, Sakaguchi H, Darrow RM, Yan L, West KA, Aulak KS, Stuehr DJ, Hollyfield JG, Organisciak DT, Crabb JW (2002) Evidence that light modulates protein nitration in rat retina. *Mol Cell Proteomics* 1:293-303.
- Munz FW, McFarland WN (1973) The significance of spectral position in the rhodopsins of tropical marine fishes. *Vision Res* 13:1829-1874.
- Murakoshi H, Trimmer JS (1999) Identification of the Kv2.1 K⁺ channel as a major component of the delayed rectifier K⁺ current in rat hippocampal neurons. *J Neurosci* 19:1728-1735.
- Nakamura T, Tu S, Akhtar MW, Sunico CR, Okamoto S, Lipton SA (2013) Aberrant protein s-nitrosylation in neurodegenerative diseases. *Neuron* 78:596-614.
- Neal M, Cunningham J, Matthews K (1998) Selective release of nitric oxide from retinal amacrine and bipolar cells. *Invest Ophth Vis Sci* 39:850-853.
- Negishi K, Kato S, Teranishi T (1988) Dopamine cells and rod bipolar cells contain protein-kinase c-like immunoreactivity in some vertebrate retinas. *Neurosci Lett* 94:247-252.
- Neher E (1998) Vesicle pools and Ca²⁺ microdomains: New tools for understanding their roles in neurotransmitter release. *Neuron* 20:389-399.
- Nesvizhskii AI, Keller A, Kolker E, Aebersold R (2003) A statistical model for identifying proteins by tandem mass spectrometry. *Anal Chem* 75:4646-4658.
- Neufeld AH, Sawada A, Becker B (1999) Inhibition of nitric-oxide synthase 2 by aminoguanidine provides neuroprotection of retinal ganglion cells in a rat model of chronic glaucoma. *Proc Nat Acad Sci USA* 96:9944-9948.
- Nikolaev A, Leung K, Odermatt B, and Lagnado L (2013) Synaptic mechanisms of adaptation and sensitization in the retina. *Nat Neurosci* 16:934-941.

- Oesch NW, Diamond JS (2011) Ribbon synapses compute temporal contrast and encode luminance in retinal rod bipolar cells. *Nat Neurosci* 14:1555-1584.
- Oltedal L, Morkve SH, Veruki ML, Hartveit E (2007) Patch-clamp investigations and compartmental modeling of rod bipolar axon terminals in an in vitro thin-slice preparation of the mammalian retina. *J Neurophys* 97:1171-1187.
- Paige JS, Xu G, Stancevic B, Jaffrey SR (2008) Nitrosothiol Reactivity Profiling Identifies S-Nitrosylated Proteins with Unexpected Stability. *Chem Biol* 15:1307-1316.
- Palamalai V, Darrow R, Organisciak DT, Miyagi M (2006) Light-induced changes in protein nitration in photoreceptor rod outer segments. *Mol Vis* 12:1543-1551.
- Palmer MJ (2006) Modulation of Ca²⁺-activated K⁺ currents and Ca²⁺-dependent action potentials by exocytosis in goldfish bipolar cell terminals. *J Physiol* 572:747-762.
- Palmer MJ (2010) Characterization of bipolar cell synaptic transmission in goldfish retina using paired recordings. *J Physiol* 588:1489-1498.
- Palmer MJ, Taschenberger H, Hull C, Tremere L, von Gersdorff H (2003) Synaptic activation of presynaptic glutamate transporter currents in nerve terminals. *J Neurosci* 23:4831-4841.
- Palmer ZJ, Duncan RR, Johnson JR, Lian LY, Mello LV, Booth D, Barclay JW, Graham ME, Burgoyne RD, Prior IA, Morgan A (2008) S-nitrosylation of syntaxin 1 at Cys(145) is a regulatory switch controlling Munc18-1 binding. *Biochem J* 413:479-491.
- Pang JJ, Gao F, Lem J, Bramblett DE, Paul DL, Wu SM (2010a) Direct rod input to cone BCs and direct cone input to rod BCs challenge the traditional view of mammalian BC circuitry. *Proc Natl Acad Sci U S A* 107:395-400.
- Pang JJ, Gao F, Wu SM. 2010b. Light Responses and Morphology of bNOS-Immunoreactive Neurons in the Mouse Retina. *J Comp Neurol* 518:2456-2474.

- Papadia S, Soriano FX, Leveille F, Martel M-A, Dakin KA, Hansen HH, Kaindl A, Sifringer M, Fowler J, Stefovskaja V, McKenzie G, Craighan M, Corriveau R, Ghazal P, Horsburgh K, Yankner BA, Wyllie DJA, Ikonomidou C, Hardingham GE (2008) Synaptic NMDA receptor activity boosts intrinsic antioxidant defenses. *Nat Neurosci* 11:476-487.
- Park JH, Straub VA, O'Shea M (1998) Anterograde signaling by nitric oxide: Characterization and in vitro reconstitution of an identified nitroergic synapse. *J Neurosci* 18:5463-5476.
- Pascual JM, Shieh CC, Kirsch GE, Brown AM (1997) Contribution of the NH₂ terminus of Kv2.1 to channel activation. *Am J Phys-Cell Phys* 273:C1849-C1858.
- Piehl L, Capani F, Facorro G, Lopez EM, de Celis ER, Pustovrh C, Hager A, Coirini H, Lopez-Costa JJ (2007) Nitric oxide increases in the rat retina after continuous illumination. *Brain Res* 1156:112-119.
- Ping Y, Huang H, Zhang XJ, Yang XL (2008) Melatonin potentiates rod signals to ON type bipolar cells in fish retina. *J Physiol* 586:2683-2694.
- Pinto LH, Klumpp DJ (1998) Localization of potassium channels in the retina. *Prog Retinal Eye Res* 17:207-230.
- Protti DA, Flores-Herr N, Li W, Massey SC, Wässle H (2005) Light signaling in scotopic conditions in the rabbit, mouse and rat retina: a physiological and anatomical study. *J Neurophysiol* 93:3479-3488.
- Protti DA, Flores-Herr N, von Gersdorff H (2000) Light evokes Ca²⁺ spikes in the axon terminal of a retinal bipolar cell. *Neuron* 25:215-227.
- Qu J, Nakamura T, Cao G, Holland EA, McKercher SR, Lipton SA (2011) S-Nitrosylation activates Cdk5 and contributes to synaptic spine loss induced by beta-amyloid peptide. *P Natl Acad Sci USA* 108:14330-14335.

- Rieke F (2001) Temporal contrast adaptation in salamander bipolar cells. *J Neurosci* 21:9445-9454.
- Rieke F, Rudd ME (2009) The challenges natural images pose for visual adaptation. *Neuron* 64:605-616.
- Rieke F, Schwartz EA (1994) A cGMP-gated current can control exocytosis at cone synapses. *Neuron* 13:863-873.
- Rossi-George A, Gow AJ (2013) Immunofluorescent detection of S-nitrosoproteins in cell culture. *Methods* 62:161-164.
- Roy B, Halvey EJ, Garthwaite J (2008) An enzyme-linked receptor mechanism for nitric oxide-activated guanylyl cyclase. *J Biol Chem* 283:18841-18851.
- Saenz DA, Turjanski AG, Sacca GB, Marti M, Doctorovich F, Sarmiento MIK, Estrin DA, Rosenstein RE (2002) Physiological concentrations of melatonin inhibit the nitridergic pathway in the Syrian hamster retina. *J Pineal Res* 33:31-36.
- Sah P, Davies P (2000) Calcium-activated potassium currents in mammalian neurons. *Clin Exp Pharmacol Physiol* 27:657-663.
- Saito T, Kondo H, Toyoda J (1979) Ionic mechanisms of 2 types of on-center bipolar cells in the carp retina .1. responses to central illumination. *J Gen Physiol* 73:73-90.
- Saito T, Kujiraoka T (1982) Physiological and morphological identification of 2 types of on-center bipolar cells in the carp retina. *J Comp Neurol* 205:161-170.
- Sakaba T, Ishikane H, Tachibana M (1997) Ca²⁺-activated K⁺ current at presynaptic terminals of goldfish retinal bipolar cells. *Neurosci Res* 27:219-228.
- Saszik S, DeVries SH (2012) A mammalian retinal bipolar cell uses both graded changes in membrane voltage and all-or-nothing Na⁺ spikes to encode light. *J Neurosci* 32:297-307.

- Savchenko A, Barnes S, Kramer RH (1997) Cyclic-nucleotide-gated channels mediate synaptic feedback by nitric oxide. *Nature* 390:694-698.
- Schauer KL, Freund DM, Prenni JE, Curthoys NP (2013) Proteomic profiling and pathway analysis of the response of rat renal proximal convoluted tubules to metabolic acidosis. *Am J Phys-Renal Phys* 305:F628-F640.
- Schneeweis DM, Schnapf JL (1995) Photovoltage of rods and cones in the macaque retina. *Science* 268:1053-1056.
- Sekaran S, Cunningham J, Neal MJ, Hartell NA, Djamgoz MBA (2005) Nitric oxide release is induced by dopamine during illumination of the carp retina: serial neurochemical control of light adaptation. *Eur J Neurosci* 21:2199-2208.
- Sennlaub F, Courtois Y, Goureau O (2002) Inducible nitric oxide synthase mediates retinal apoptosis in ischemic proliferative retinopathy. *J Neurosci* 22:3987-3993.
- Seth D, Stamler JS (2011) The SNO-proteome: causation and classifications. *Curr Opin Chem Biol* 15:129-136.
- Shapiro MS, Wollmuth LP, Hille B (1994) Modulation of Ca²⁺ channels by PTX-sensitive G-proteins is blocked by n-ethylmaleimide in rat sympathetic neurons. *J Neurosci* 14:7109-7116.
- Shiells RA, Falk G. 2002. Potentiation of 'on' bipolar cell flash responses by dim background light and cGMP in dogfish retinal slices. *J Physiol* 542:211-220.
- Siliprandi R, Canella R, Carmignoto G, Schiavo N, Zanellato A, Zanoni R, Vantini G (1992) N-Methyl-D-Aspartate-induced neurotoxicity in the adult-rat retina. *Vis Neurosci* 8:567-573.

Singer JH, Diamond JS (2003) Sustained Ca²⁺ entry elicits transient postsynaptic currents at a retinal ribbon synapse. *J Neurosci* 23:10923-10933.

Smirnakis SM, Berry MJ, Warland DK, Bialek W, Meister M (1997) Adaptation of retinal processing to image contrast and spatial scale. *Nature* 386:69-73.

Smyth DG, Nagamatsu A, Fruton JS (1960) Some reactions of N-Ethylmaleimide. *J Am Chem Soc* 82:4600-4604.

Snellman J, Nawy S (2004) cGMP-dependent kinase regulates response sensitivity of the mouse On bipolar cell. *J Neurosci* 24:6621-6628.

Southam E, Garthwaite J (1993) The nitric oxide-cyclic gmp signaling pathway in rat-brain. *Neuropharmacology* 32:1267-1277.

Stamler JS, Lamas S, Fang FC (2001) Nitrosylation: The prototypic redox-based signaling mechanism. *Cell* 106:675-683.

Stamler JS, Toone EJ, Lipton SA, Sucher NJ (1997) (S)NO signals: Translocation, regulation, and a consensus motif. *Neuron* 18:691-696.

Stamler JS (1994) Redox signaling - nitrosylation and related target interactions of nitric-oxide. *Cell* 78:931-936.

Steinert JR, Kopp-Scheinflug C, Baker C, Challiss RAJ, Mistry R, Haustein MD, Griffin SJ, Tong H, Graham BP, Forsythe ID (2008) Nitric Oxide Is a Volume Transmitter Regulating Postsynaptic Excitability at a Glutamatergic Synapse. *Neuron* 60:642-656.

Sterling P (2003) How retinal circuits optimize the transfer of visual information. In: *The visual neurosciences* (Chalupa LM and Werner JS, eds.), pp234-259. Cambridge, MA: MIT Press.

- Sterling P, Matthews G (2005) Structure and function of ribbon synapses. *Trends Neurosci* 28:20-29.
- Suzuki S, Kaneko A (1990) Identification of bipolar cell subtypes by protein-kinase c-like immunoreactivity in the goldfish retina. *Vis Neurosci* 5:223-230.
- Tachibana M (1999) Regulation of transmitter release from retinal bipolar cells. *Prog Biophys Mol Biol* 72:109-133.
- Tachibana M, Kaneko A (1987) Gamma-aminobutyric-acid exerts a local inhibitory-action on the axon terminal of bipolar cells - evidence for negative feedback from amacrine cells. *Proc Natl Acad Sci U S A* 84:3501-3505.
- Takahata K, Katsuki H, Kume T, Nakata D, Ito K, Muraoka S, Yoneda F, Kashii S, Honda Y, Akaike A (2003) Retinal neuronal death induced by intraocular administration of a nitric oxide donor and its rescue by neurotrophic factors in rats. *Invest Ophthalmol Vis Sci* 44:1760-1766.
- Tanimoto N, Sothilingam V, Euler T, Ruth P, Seeliger MW, Schubert T (2012) BK Channels Mediate Pathway-Specific Modulation of Visual Signals in the In Vivo Mouse Retina. *J Neurosci* 32:4861-4866.
- Tekmen-Clark M, Gleason E (2013) Nitric oxide production and the expression of two nitric oxide synthases in the avian retina. *Vis Neurosci* 30:91-103.
- Thoreson WB (2007) Kinetics of synaptic transmission at ribbon synapses of rods and cones. *Mol Neurobiol* 36:205-223.
- Thoreson WB, Mangel SC (2012) Lateral interactions in the outer retina. *Prog Retinal Eye Res* 31:407-441.

- Tian M, Zhao JW, Yang XL, Xie JX (2003) Voltage-gated K⁺ channel subunits on cholinergic and dopaminergic amacrine cells. *Neuroreport* 14:1763-1766.
- Toda N, Nakanishi-Toda M (2007) Nitric oxide: Ocular blood flow, glaucoma, and diabetic retinopathy. *Prog Retinal Eye Res* 26:205-238.
- Tooker RE, Lipin MY, Leuranguer V, Rozsa E, Bramley JR, Harding JL, Reynolds MM, Vigh J (2013) Nitric Oxide Mediates Activity-Dependent Plasticity of Retinal Bipolar Cell Output via S-Nitrosylation. *J Neurosci* 33:19176-19193.
- Tsumamoto Y, Yamashita K, Takumida M, Okada K, Mukai S, Shinya M, Yamashita H, Mishima HK (2002) In situ localization of nitric oxide synthase and direct evidence of NO production in rat retinal ganglion cells. *Brain Res* 933:118-129.
- Vergara C, Latorre R, Marrion NV, Adelman JP (1998) Calcium-activated potassium channels. *Curr Opin Neurobiol* 8:321-329.
- Vielma AH, Delgado L, Elgueta C, Osorio R, Palacios AG, Schmachtenberg O (2010) Nitric oxide amplifies the rat electroretinogram. *Exp Eye Res* 91:700-709.
- Vielma AH, Retamal MA, Schmachtenberg O (2012) Nitric oxide signaling in the retina: What have we learned in two decades? *Brain Res* 1430:112-125.
- Vigh J, Li GL, Hull C, von Gersdorff L (2005) Long-term plasticity mediated by mGluR1 at a retinal reciprocal synapse. *Neuron* 46:469-482.
- Vigh J, Vickers E, von Gersdorff H (2011) Light-Evoked Lateral GABAergic Inhibition at Single Bipolar Cell Synaptic Terminals Is Driven by Distinct Retinal Microcircuits. *J Neurosci* 31:15884-15893.
- Vigh J, von Gersdorff H (2005) Prolonged reciprocal signaling via NMDA and GABA receptors at a retinal ribbon synapse. *J Neurosci* 25:11412-11423.

- Villani L, Guarnieri T (1996) Localization of nitric oxide synthase in the goldfish retina. *Brain Res* 743:353-356.
- von Gersdorff H, Matthews G (1996) Calcium-dependent inactivation of calcium current in synaptic terminals of retinal bipolar neurons. *J Neurosci* 16:115-122.
- von Gersdorff H, Matthews G (1997) Depletion and replenishment of vesicle pools at a ribbon-type synaptic terminal. *J Neurosci* 17:1919-1927.
- Vorwerk CK, Hyman BT, Miller JW, Husain D, Zurakowski D, Huang PL, Fishman MC, Dreyer EB (1997) The role of neuronal and endothelial nitric oxide synthase in retinal excitotoxicity. *Invest Ophthalmol Vis Sci* 38:2038-2044.
- Walraven, J, Enroth-Cugell, C, Hood, DC, MacLeod, DIA, and Schnapf, JL (1990) In *Visual Perception: The Neurophysiological Foundations* (L. Spillman and J.Z. Werner, eds.), pp.53–101 San Diego, CA: Academic Press.
- Walter LT, Higa GS, Schmeltzer C, Sousa E, Kinjo ER, Rudiger S, Hamassaki DE, Cerchiaro G, Kihara AH (2014) Functional regulation of neuronal nitric oxide synthase expression and activity in the rat retina. *Exp Neurol* 261:510-517.
- Wang GY, Van der List DA, Nemargut JP, Coombs JL, Chalupa LM (2007) The sensitivity of light-evoked responses of retinal ganglion cells is decreased in nitric oxide synthase gene knockout mice. *J Vision* 7:1-13.
- Wang Y, Liu T, Wu C, Li H (2008) A strategy for direct identification of protein S-nitrosylation sites by quadrupole time-of-flight mass spectrometry. *J Am Soc Mass Spectrom* 19:1353-1360.
- Wässle H (2004) Parallel processing in the mammalian retina. *Nat Rev Neurosci* 5:747-757.

- Wei HP, Yao YY, Zhang RW, Zhao XF, Du JL (2012) Activity-induced long-term potentiation of excitatory synapses in developing zebrafish retina in vivo. *Neuron* 75:479-489.
- Werblin FS, Dowling JE (1969) Organization of retina of mudpuppy *necturus maculosus*. II. intracellular recording. *J Neurophysiol* 32:339-355.
- Witkovsky P (2004) Dopamine and retinal function. *Doc Ophthalmol* 108:17-40.
- Witkovsky P, Dowling JE (1969) Synaptic relationships in the plexiform layers of carp retina. *Z Zellforsch Mikrosk Anat* 100:60-82.
- Wong KY, Cohen ED, Dowling JE (2005) Retinal bipolar cell input mechanisms in giant danio. II. Patch-clamp analysis of ON bipolar cells. *J Neurophysiol* 93:94-107.
- Wood J, Garthwaite J (1994) Models of the diffusional spread of nitric-oxide - implications for neural nitric-oxide signaling and its pharmacological properties. *Neuropharmacology* 33:1235-1244.
- Wu SM (1994) Synaptic transmission in the outer retina. *Annu Rev Physiol* 56:141-168.
- Wulle I, Wagner HJ (1990) GABA and tyrosine-hydroxylase immunocytochemistry reveal different patterns of colocalization in retinal neurons of various vertebrates. *J Comp Neurol* 296:173-178.
- Xin DY, Bloomfield SA (1999) Comparison of the responses of AII amacrine cells in the dark- and light-adapted rabbit retina. *Vis Neurosci* 16:653-665.
- Yazulla S, Studholme KM (1992) Light-dependent plasticity of the synaptic terminals of Mb bipolar cells in goldfish retina. *J Comp Neurol* 320:521-530.
- Yazulla S, Studholme KM (1998) Differential distribution of Shaker-like and Shab-like K⁺-channel subunits in goldfish retina and retinal bipolar cells. *J Comp Neurol* 396:131-140.

- Yego ECK, Mohr S (2010) siah-1 Protein Is Necessary for High Glucose-induced Glyceraldehyde-3-phosphate Dehydrogenase Nuclear Accumulation and Cell Death in Muller Cells. *J Bio Chem* 285:3181-3190.
- Yu D, Eldred WD (2005) Nitric oxide stimulates gamma-aminobutyric acid release and inhibits glycine release in retina. *J Comp Neurol* 483:278-291.
- Zenisek D, Matthews G (1998) Calcium action potentials in retinal bipolar neurons. *Vis Neurosci* 15:69-75.
- Zhu YL, Xu J, Hauswirth WW, DeVries SH (2014) Genetically Targeted Binary Labeling of Retinal Neurons. *J Neurosci* 34:7845-7861.

Appendix I:

Journal of Comparative Neurology Permissions Policy: “**AUTHORS** - If you wish to reuse your own article (or an amended version of it) in a new publication of which you are the author, editor or co-editor, prior permission is not required (with the usual acknowledgements). However, a formal grant of license can be downloaded free of charge from RightsLink if required.”

[http://onlinelibrary.wiley.com/journal/10.1002/\(ISSN\)1096-9861/homepage/Permissions.html](http://onlinelibrary.wiley.com/journal/10.1002/(ISSN)1096-9861/homepage/Permissions.html)

JOHN WILEY AND SONS LICENSE TERMS AND CONDITIONS

Mar 31, 2015

This Agreement between Ryan E Tooker ("You") and John Wiley and Sons ("John Wiley and Sons") consists of your license details and the terms and conditions provided by John Wiley and Sons and Copyright Clearance Center.

License Number

3599580950830

License date

Mar 31, 2015

Licensed Content Publisher

John Wiley and Sons

Licensed Content Publication

Journal of Comparative Neurology

Licensed Content Title

Light-evoked S-nitrosylation in the retina

Licensed Content Author

Ryan E Tooker, Jozsef Vigh

Licensed Content Date

Mar 30, 2015

Pages

1

Type of use

Dissertation/Thesis

Requestor type

Author of this Wiley article

Format

Print and electronic

Portion

Full article

Will you be translating?

No

Title of your thesis / dissertation

S-NITROSYLATION MEDIATES SYNAPTIC PLASTICITY IN THE RETINA

Expected completion date

May 2015

Expected size (number of pages)

160

Requestor Location

Ryan E Tooker
1617 Campus Delivery

FORT COLLINS, CO 80521
United States
Attn: Ryan E Tooker

Billing Type

Invoice

Billing Address

Ryan E Tooker
1617 Campus Delivery



FORT COLLINS, CO 80521
United States
Attn: Ryan E Tooker

Total

0.00 USD

Terms and Conditions

TERMS AND CONDITIONS

This copyrighted material is owned by or exclusively licensed to John Wiley & Sons, Inc. or one of its group companies (each a "Wiley Company") or handled on behalf of a society with which a Wiley Company has exclusive publishing rights in relation to a particular work (collectively "WILEY"). By clicking  accept  in connection with completing this licensing transaction, you agree that the following terms and conditions apply to this transaction (along with the billing and payment terms and conditions established by the Copyright Clearance Center Inc., ("CCC's Billing and Payment terms and conditions"), at the time that you opened your Rightslink account (these are available at any time at <http://myaccount.copyright.com>).

Terms and Conditions

- The materials you have requested permission to reproduce or reuse (the "Wiley Materials") are protected by copyright.
- You are hereby granted a personal, non-exclusive, non-sub licensable (on a stand-alone basis), non-transferable, worldwide, limited license to reproduce the Wiley Materials for the purpose specified in the licensing process. This license is for a one-time use only and limited to any maximum distribution number specified in the license. The first instance of republication or reuse granted by this licence must be completed within two years of the date of the grant of this licence (although copies prepared before the end date may be distributed thereafter). The Wiley Materials shall not be used in any other manner or for any other purpose, beyond what is granted in the license. Permission is granted subject to an appropriate acknowledgement given to the author, title of the material/book/journal and the publisher. You shall also duplicate the copyright notice that appears in the Wiley publication in your use of the Wiley Material. Permission is also granted on the understanding that nowhere in the text is a previously published source acknowledged for all or part of this Wiley Material. Any third party content is expressly excluded from this permission.

- With respect to the Wiley Materials, all rights are reserved. Except as expressly granted by the terms of the license, no part of the Wiley Materials may be copied, modified, adapted (except for minor reformatting required by the new Publication), translated, reproduced, transferred or distributed, in any form or by any means, and no derivative works may be made based on the Wiley Materials without the prior permission of the respective copyright owner. You may not alter, remove or suppress in any manner any copyright, trademark or other notices displayed by the Wiley Materials. You may not license, rent, sell, loan, lease, pledge, offer as security, transfer or assign the Wiley Materials on a stand-alone basis, or any of the rights granted to you hereunder to any other person.
- The Wiley Materials and all of the intellectual property rights therein shall at all times remain the exclusive property of John Wiley & Sons Inc, the Wiley Companies, or their respective licensors, and your interest therein is only that of having possession of and the right to reproduce the Wiley Materials pursuant to Section 2 herein during the continuance of this Agreement. You agree that you own no right, title or interest in or to the Wiley Materials or any of the intellectual property rights therein. You shall have no rights hereunder other than the license as provided for above in Section 2. No right, license or interest to any trademark, trade name, service mark or other branding ("Marks") of WILEY or its licensors is granted hereunder, and you agree that you shall not assert any such right, license or interest with respect thereto.
- **NEITHER WILEY NOR ITS LICENSORS MAKES ANY WARRANTY OR REPRESENTATION OF ANY KIND TO YOU OR ANY THIRD PARTY, EXPRESS, IMPLIED OR STATUTORY, WITH RESPECT TO THE MATERIALS OR THE ACCURACY OF ANY INFORMATION CONTAINED IN THE MATERIALS, INCLUDING, WITHOUT LIMITATION, ANY IMPLIED WARRANTY OF MERCHANTABILITY, ACCURACY, SATISFACTORY QUALITY, FITNESS FOR A PARTICULAR PURPOSE, USABILITY, INTEGRATION OR NON-INFRINGEMENT AND ALL SUCH WARRANTIES ARE HEREBY EXCLUDED BY WILEY AND ITS LICENSORS AND WAIVED BY YOU**
- WILEY shall have the right to terminate this Agreement immediately upon breach of this Agreement by you.
- You shall indemnify, defend and hold harmless WILEY, its Licensors and their respective directors, officers, agents and employees, from and against any actual or threatened claims, demands, causes of action or proceedings arising from any breach of this Agreement by you.
- **IN NO EVENT SHALL WILEY OR ITS LICENSORS BE LIABLE TO YOU OR ANY OTHER PARTY OR ANY OTHER PERSON OR ENTITY FOR ANY SPECIAL, CONSEQUENTIAL, INCIDENTAL, INDIRECT, EXEMPLARY OR PUNITIVE DAMAGES, HOWEVER CAUSED, ARISING OUT OF OR IN CONNECTION WITH THE DOWNLOADING, PROVISIONING, VIEWING OR USE OF THE MATERIALS REGARDLESS OF THE FORM OF ACTION, WHETHER FOR BREACH OF CONTRACT, BREACH OF WARRANTY, TORT, NEGLIGENCE, INFRINGEMENT OR OTHERWISE (INCLUDING, WITHOUT LIMITATION, DAMAGES BASED ON**

LOSS OF PROFITS, DATA, FILES, USE, BUSINESS OPPORTUNITY OR CLAIMS OF THIRD PARTIES), AND WHETHER OR NOT THE PARTY HAS BEEN ADVISED OF THE POSSIBILITY OF SUCH DAMAGES. THIS LIMITATION SHALL APPLY NOTWITHSTANDING ANY FAILURE OF ESSENTIAL PURPOSE OF ANY LIMITED REMEDY PROVIDED HEREIN.

- Should any provision of this Agreement be held by a court of competent jurisdiction to be illegal, invalid, or unenforceable, that provision shall be deemed amended to achieve as nearly as possible the same economic effect as the original provision, and the legality, validity and enforceability of the remaining provisions of this Agreement shall not be affected or impaired thereby.
- The failure of either party to enforce any term or condition of this Agreement shall not constitute a waiver of either party's right to enforce each and every term and condition of this Agreement. No breach under this agreement shall be deemed waived or excused by either party unless such waiver or consent is in writing signed by the party granting such waiver or consent. The waiver by or consent of a party to a breach of any provision of this Agreement shall not operate or be construed as a waiver of or consent to any other or subsequent breach by such other party.
- This Agreement may not be assigned (including by operation of law or otherwise) by you without WILEY's prior written consent.
- Any fee required for this permission shall be non-refundable after thirty (30) days from receipt by the CCC.
- These terms and conditions together with CCC's Billing and Payment terms and conditions (which are incorporated herein) form the entire agreement between you and WILEY concerning this licensing transaction and (in the absence of fraud) supersedes all prior agreements and representations of the parties, oral or written. This Agreement may not be amended except in writing signed by both parties. This Agreement shall be binding upon and inure to the benefit of the parties' successors, legal representatives, and authorized assigns.
- In the event of any conflict between your obligations established by these terms and conditions and those established by CCC's Billing and Payment terms and conditions, these terms and conditions shall prevail.
- WILEY expressly reserves all rights not specifically granted in the combination of (i) the license details provided by you and accepted in the course of this licensing transaction, (ii) these terms and conditions and (iii) CCC's Billing and Payment terms and conditions.
- This Agreement will be void if the Type of Use, Format, Circulation, or Requestor Type was misrepresented during the licensing process.

- This Agreement shall be governed by and construed in accordance with the laws of the State of New York, USA, without regards to such state's conflict of law rules. Any legal action, suit or proceeding arising out of or relating to these Terms and Conditions or the breach thereof shall be instituted in a court of competent jurisdiction in New York County in the State of New York in the United States of America and each party hereby consents and submits to the personal jurisdiction of such court, waives any objection to venue in such court and consents to service of process by registered or certified mail, return receipt requested, at the last known address of such party.

WILEY OPEN ACCESS TERMS AND CONDITIONS

Wiley Publishes Open Access Articles in fully Open Access Journals and in Subscription journals offering Online Open. Although most of the fully Open Access journals publish open access articles under the terms of the Creative Commons Attribution (CC BY) License only, the subscription journals and a few of the Open Access Journals offer a choice of Creative Commons Licenses:: Creative Commons Attribution (CC-BY) license [Creative Commons Attribution Non-Commercial \(CC-BY-NC\) license](#) and [Creative Commons Attribution Non-Commercial-NoDerivs \(CC-BY-NC-ND\) License](#). The license type is clearly identified on the article.

Copyright in any research article in a journal published as Open Access under a Creative Commons License is retained by the author(s). Authors grant Wiley a license to publish the article and identify itself as the original publisher. Authors also grant any third party the right to use the article freely as long as its integrity is maintained and its original authors, citation details and publisher are identified as follows: [Title of Article/Author/Journal Title and Volume/Issue. Copyright (c) [year] [copyright owner as specified in the Journal]. Links to the final article on Wiley's website are encouraged where applicable.

The Creative Commons Attribution License

The [Creative Commons Attribution License \(CC-BY\)](#) allows users to copy, distribute and transmit an article, adapt the article and make commercial use of the article. The CC-BY license permits commercial and non-commercial re-use of an open access article, as long as the author is properly attributed.

The Creative Commons Attribution License does not affect the moral rights of authors, including without limitation the right not to have their work subjected to derogatory treatment. It also does not affect any other rights held by authors or third parties in the article, including without limitation the rights of privacy and publicity. Use of the article must not assert or imply, whether implicitly or explicitly, any connection with, endorsement or sponsorship of such use by the author, publisher or any other party associated with the article.

For any reuse or distribution, users must include the copyright notice and make clear to others that the article is made available under a Creative Commons Attribution license, linking to the relevant Creative Commons web page.

To the fullest extent permitted by applicable law, the article is made available as is and without representation or warranties of any kind whether express, implied, statutory or otherwise and including, without limitation, warranties of title, merchantability, fitness for a particular purpose, non-infringement, absence of defects, accuracy, or the presence or absence of errors.

Creative Commons Attribution Non-Commercial License

The [Creative Commons Attribution Non-Commercial \(CC-BY-NC\) License](#) permits use, distribution and reproduction in any medium, provided the original work is properly cited and is not used for commercial purposes.(see below)

Creative Commons Attribution-Non-Commercial-NoDerivs License

The [Creative Commons Attribution Non-Commercial-NoDerivs License](#) (CC-BY-NC-ND) permits use, distribution and reproduction in any medium, provided the original work is properly cited, is not used for commercial purposes and no modifications or adaptations are made. (see below)

Use by non-commercial users

For non-commercial and non-promotional purposes, individual users may access, download, copy, display and redistribute to colleagues Wiley Open Access articles, as well as adapt, translate, text- and data-mine the content subject to the following conditions:

- The authors' moral rights are not compromised. These rights include the right of "paternity" (also known as "attribution" - the right for the author to be identified as such) and "integrity" (the right for the author not to have the work altered in such a way that the author's reputation or integrity may be impugned).
- Where content in the article is identified as belonging to a third party, it is the obligation of the user to ensure that any reuse complies with the copyright policies of the owner of that content.
- If article content is copied, downloaded or otherwise reused for non-commercial research and education purposes, a link to the appropriate bibliographic citation (authors, journal, article title, volume, issue, page numbers, DOI and the link to the definitive published version on **Wiley Online Library**) should be maintained. Copyright notices and disclaimers must not be deleted.
- Any translations, for which a prior translation agreement with Wiley has not been agreed, must prominently display the statement: "This is an unofficial translation of an article that appeared in a Wiley publication. The publisher has not endorsed this translation."

Use by commercial "for-profit" organisations

Use of Wiley Open Access articles for commercial, promotional, or marketing purposes requires further explicit permission from Wiley and will be subject to a fee. Commercial purposes include:

- Copying or downloading of articles, or linking to such articles for further redistribution, sale or licensing;
- Copying, downloading or posting by a site or service that incorporates advertising with such content;
- The inclusion or incorporation of article content in other works or services (other than normal quotations with an appropriate citation) that is then available for sale or licensing, for a fee (for example, a compilation produced for marketing purposes, inclusion in a sales pack)
- Use of article content (other than normal quotations with appropriate citation) by for-profit organisations for promotional purposes
- Linking to article content in e-mails redistributed for promotional, marketing or educational purposes;
- Use for the purposes of monetary reward by means of sale, resale, licence, loan, transfer or other form of commercial exploitation such as marketing products
- Print reprints of Wiley Open Access articles can be purchased from: corporatesales@wiley.com

Further details can be found on Wiley Online

Library <http://olabout.wiley.com/WileyCDA/Section/id-410895.html>

Other Terms and Conditions:

v1.9

Questions? customercare@copyright.com or +1-855-239-3415 (toll free in the US) or +1-978-646-2777.

Gratis licenses (referencing \$0 in the Total field) are free. Please retain this printable license for your reference. No payment is required.

Appendix II:

Table 2.2. List of S-nitrosylated proteins identified *only* under light-adapted conditions.

Protein Name	Gene	Accession Number	Peptide Score
<u>Apoptosis/Cell Death</u>			
Bcl-2-like protein 13	Bcl2l13	B2L13_MOUSE	2
Isoform 2 of Band 4.1-like protein 3	Epb41l3	E41L3_MOUSE	10
Isoform 2 of Peptidyl-prolyl cis-trans isomerase FKBP8	Fkbp8	FKBP8_MOUSE	2
Isoform 8 of Band 4.1-like protein 3	Epb41l3	E41L3_MOUSE	2
MAP kinase-activating death domain protein	Madd	A2AGQ6_MOUSE	3
Mitochondrial fission 1 protein	Fis1	FIS1_MOUSE	2
NADH dehydrogenase [ubiquinone] 1 alpha subcomplex subunit 13	Ndufa13	NDUAD_MOUSE	3
<u>Calcium Ion Regulation</u>			
Calbindin	Calb1	CALB1_MOUSE	4
Isoform 3 of Disks large homolog 4	Dlg4	DLG4_MOUSE	6
Secretagogin	Scgn	SEGN_MOUSE	7
<u>Cardiovascular</u>			
Alpha actinin 1a	Actn1	A1BN54_MOUSE	2
Carbonic anhydrase 14	Ca14	CAH14_MOUSE	2
<u>Cell Adhesion</u>			
Cadherin-2	Cdh2	CADH2_MOUSE	2
Cell adhesion molecule 1	Cadm1	CADM1_MOUSE	8
Cell adhesion molecule 2 (Fragment)	Cadm2	CADM2_MOUSE	10
Cell adhesion molecule 3	Cadm3	CADM3_MOUSE	2
Contactin-1	Cntn1	CNTN1_MOUSE	7
Isoform 2 of Neuronal cell adhesion molecule	Nrcam	NRCAM_MOUSE	4

Limbic system-associated membrane protein	Lsamp	LSAMP_MOUSE	4
Neural cell adhesion molecule 1	Ncam1	E9QB01_MOUSE	2
Neuroplastin	Nptn	NPTN_MOUSE	3
Peripherin-2	Prph2	PRPH2_MOUSE	9
Rod outer segment membrane protein 1	Rom1	ROM1_MOUSE	6
Signal-regulatory protein alpha	Sirpa	Q6P618_MOUSE	3
Transforming protein RhoA	Rhoa	RHOA_MOUSE	3
<u>Cell Cycle/Cell Division</u>			
Casein kinase II subunit beta	Csnk2b	CSK2B_MOUSE	2
Cell cycle exit and neuronal differentiation protein 1	Cend1	CEND_MOUSE	3
Cell division control protein 42 homolog	Cdc42	CDC42_MOUSE	2
Cyclin-dependent kinase 5 OS=Mus musculus	Cdk5	CDK5_MOUSE	2
Histone H2AX	H2afx	H2AX_MOUSE	2
Isoform 2 of Septin-11	Sep11	SEP11_MOUSE	2
Isoform Gamma-2 of Serine/threonine-protein phosphatase PP1-gamma catalytic subunit	Ppp1cc	PP1G_MOUSE	3
Nuclear migration protein nudC	Nudc	NUDC_MOUSE	2
Platelet-activating factor acetylhydrolase IB subunit alpha	Pafah1b1	LIS1_MOUSE	4
Putative adenosylhomocysteinase 2	Ahcy1	SAHH2_MOUSE	2
Serine/threonine-protein phosphatase	Ppp3cb	E0CZ78_MOUSE	2
Serine-protein kinase ATM	Atm	ATM_MOUSE	2
<u>Cell Growth/Proliferation</u>			
Catenin beta-1	Ctnnb1	CTNB1_MOUSE	4
Isoform C1 of Heterogeneous nuclear ribonucleoproteins C1/C2	Hnrnpc	HNRPC_MOUSE	2
Membrane-associated progesterone receptor component 1	Pgrmc1	PGRC1_MOUSE	2
Membrane-associated progesterone receptor component 2	Pgrmc2	PGRC2_MOUSE	2
Myotrophin	Mtpn	MTPN_MOUSE	2
Neuromodulin	Gap43	NEUM_MOUSE	2
Neuronal growth regulator 1	Negr1	NEGR1_MOUSE	3

Neuronal membrane glycoprotein M6-a	Gpm6a	GPM6A_MOUSE	5
Prominin 1, isoform CRA_g	Prom1	PROM1_MOUSE	2
<u>Chaperone</u>			
10 kDa heat shock protein, mitochondrial	Hspe1	CH10_MOUSE	3
26S proteasome non-ATPase regulatory subunit 5	Psm5	PSMD5_MOUSE	2
Coactosin-like protein	Cotl1	COTL1_MOUSE	2
DnaJ homolog subfamily A member 2	Dnaja2	DNJA2_MOUSE	2
DnaJ homolog subfamily C member 5	Dnajc5	DNJC5_MOUSE	2
Isoform 3 of Putative tyrosine-protein phosphatase auxilin	Dnajc6	AUXI_MOUSE	4
Large proline-rich protein BAG6	Bag6	BAG6_MOUSE	3
Peptidyl-prolyl cis-trans isomerase B	Ppib	PIIB_MOUSE	3
Phosducin-like protein	Pdcl	PHLP_MOUSE	2
<u>Cytoskeleton</u>			
Actin-related protein 2/3 complex subunit 3	Arpc3	ARPC3_MOUSE	3
Alpha-adducin	Add1	ADDA_MOUSE	8
Alpha-centractin	Actr1a	ACTZ_MOUSE	2
Destrin	Dstn	DEST_MOUSE	4
Gephyrin	Gphn	GEPH_MOUSE	2
Glycoprotein m6b, isoform CRA_g	Gpm6b	GPM6B_MOUSE	3
IQ motif and SEC7 domain-containing protein 3	Iqsec3	IQEC3_MOUSE	2
Isoform 2 of Rootletin	Crocc	CROCC_MOUSE	2
Isoform 4 of Nesprin-1	Syne1	SYNE1_MOUSE	2
Myristoylated alanine-rich C-kinase substrate	Marcks	MARCS_MOUSE	3
Protein 4.1	Epb4.1	A2A841_MOUSE	12
Protein kinase C and casein kinase substrate in neurons protein 2	Pacsin2	PACN2_MOUSE	2
<u>DNA Metabolism/Regulation</u>			
Prohibitin	Phb	PHB_MOUSE	8
Prohibitin-2	Phb2	PHB2_MOUSE	7

Endocytosis

Adaptin ear-binding coat-associated protein 1	Necap1	NECP1_MOUSE	2
Dynamamin-3	Dnm3	DYN3_MOUSE	5
Dynamamin-like 120 kDa protein, mitochondrial	Opa1	OPA1_MOUSE	2
Isoform 3 of SH3-containing GRB2-like protein 3-interacting protein 1	Sgip1	SGIP1_MOUSE	3
Secretory carrier-associated membrane protein 1	Scamp1	SCAM1_MOUSE	2
Synaptophysin	Syp	SYPH_MOUSE	2

Energy Metabolism

6-phosphofructo-2-kinase/fructose-2, 6-bisphosphatase 2 variant 4	Pfkfb2	B2Z892_MOUSE	2
6-phosphofructokinase	Pfkm	Q8C605_MOUSE	8
6-phosphofructokinase, muscle type	Pfkm	K6PF_MOUSE	2
Adenine phosphoribosyltransferase	Aprt	APT_MOUSE	2
ADP/ATP translocase 2	Slc25a5	ADT2_MOUSE	3
ATP synthase F(0) complex subunit B1, mitochondrial	Atp5f1	AT5F1_MOUSE	6
ATP synthase subunit epsilon, mitochondrial	Atp5e	ATP5E_MOUSE	2
ATP synthase subunit f, mitochondrial	Atp5j2	ATPK_MOUSE	2
ATP synthase subunit g, mitochondrial	Atp5l	ATP5L_MOUSE	2
CDGSH iron-sulfur domain-containing protein 1	Cisd1	CISD1_MOUSE	3
Citrate synthase, mitochondrial	Cs	CISY_MOUSE	8
Creatine kinase M-type	Ckm	KCRM_MOUSE	2
Cytochrome b-c1 complex subunit 7	Uqcrb	Q9CQB4_MOUSE	4
Cytochrome b-c1 complex subunit 9	Uqcr10	QCR9_MOUSE	2
Cytochrome b-c1 complex subunit Rieske, mitochondrial	Uqcrrs1	UCRI_MOUSE	7
Cytochrome c oxidase subunit 4 isoform 1, mitochondrial	Cox4i1	COX41_MOUSE	4
Cytochrome c oxidase subunit 5A, mitochondrial	Cox5a	COX5A_MOUSE	7
Cytochrome c oxidase subunit 7A2, mitochondrial	Cox7a2	CX7A2_MOUSE	2
Dihydrolipoyllysine-residue acetyltransferase component of pyruvate dehydrogenase complex, mitochondrial	Dlat	ODP2_MOUSE	6
Electron transfer flavoprotein subunit alpha, mitochondrial	Etfa	ETFA_MOUSE	4

Electron transfer flavoprotein subunit beta	Etfb	ETFB_MOUSE	3
GTP:AMP phosphotransferase AK3, mitochondrial	Ak3	KAD3_MOUSE	2
Hexokinase-2	Hk2	HXK2_MOUSE	11
Isocitrate dehydrogenase [NAD] subunit alpha, mitochondrial	Idh3a	IDH3A_MOUSE	8
Isocitrate dehydrogenase [NAD] subunit gamma 1, mitochondrial	Idh3g	IDHG1_MOUSE	3
Isocitrate dehydrogenase [NADP], mitochondrial	Idh2	IDHP_MOUSE	4
Isocitrate dehydrogenase 3 (NAD+) beta	Idh3b	Q91VA7_MOUSE	6
Isoform 2 of Cytochrome c1, heme protein, mitochondrial	Cyc1	CY1_MOUSE	6
Isoform Short of Adenosine kinase	Adk	ADK_MOUSE	2
NADH dehydrogenase [ubiquinone] 1 alpha subcomplex subunit 10, mitochondrial	Ndufa10	NDUAA_MOUSE	5
NADH dehydrogenase [ubiquinone] 1 alpha subcomplex subunit 12	Ndufa12	NDUAC_MOUSE	2
NADH dehydrogenase [ubiquinone] 1 alpha subcomplex subunit 4	Ndufa4	NDUA4_MOUSE	4
NADH dehydrogenase [ubiquinone] 1 alpha subcomplex subunit 6	Ndufa6	NDUA6_MOUSE	2
NADH dehydrogenase [ubiquinone] 1 alpha subcomplex subunit 8	Ndufa8	NDUA8_MOUSE	4
NADH dehydrogenase [ubiquinone] 1 alpha subcomplex subunit 9, mitochondrial	Ndufa9	NDUA9_MOUSE	3
NADH dehydrogenase [ubiquinone] 1 beta subcomplex subunit 11, mitochondrial	Ndufb11	NDUBB_MOUSE	3
NADH dehydrogenase [ubiquinone] 1 beta subcomplex subunit 3	Ndufb3	NDUB3_MOUSE	2
NADH dehydrogenase [ubiquinone] 1 beta subcomplex subunit 4	Ndufb4	NDUB4_MOUSE	3
NADH dehydrogenase [ubiquinone] 1 beta subcomplex subunit 8, mitochondrial	Ndufb8	NDUB8_MOUSE	2
NADH dehydrogenase [ubiquinone] 1 beta subcomplex subunit 9	Ndufb9	NDUB9_MOUSE	2
NADH dehydrogenase [ubiquinone] flavoprotein 1, mitochondrial	Ndufv1	NDUV1_MOUSE	5
NADH dehydrogenase [ubiquinone] flavoprotein 2, mitochondrial	Ndufv2	NDUV2_MOUSE	2
NADH dehydrogenase [ubiquinone] iron-sulfur protein 2, mitochondrial	Ndufs2	NDUS2_MOUSE	2
NADH dehydrogenase [ubiquinone] iron-sulfur protein 3, mitochondrial	Ndufs3	NDUS3_MOUSE	6
NADH dehydrogenase [ubiquinone] iron-sulfur protein 7, mitochondrial	Ndufs7	NDUS7_MOUSE	2
NADH dehydrogenase [ubiquinone] iron-sulfur protein 8, mitochondrial	Ndufs8	NDUS8_MOUSE	5

NADH-ubiquinone oxidoreductase 75 kDa subunit, mitochondrial	Ndufs1	NDUS1_MOUSE	14
Phosphoglucosmutase-2	Pgm2	PGM2_MOUSE	2
Protein Ogdhl	Ogdhl	E9Q7L0_MOUSE	4
Pyruvate carboxylase	Pcx	PYC_MOUSE	2
Pyruvate dehydrogenase E1 component subunit alpha, somatic form, mitochondrial	Pdha1	ODPA_MOUSE	5
Pyruvate dehydrogenase E1 component subunit beta, mitochondrial	Pdhb	ODPB_MOUSE	7
Stomatin-like protein 2, mitochondrial	Stoml2	STML2_MOUSE	5
Succinate dehydrogenase [ubiquinone] flavoprotein subunit, mitochondrial	Sdha	DHSA_MOUSE	8
Succinate dehydrogenase [ubiquinone] iron-sulfur subunit, mitochondrial	Sdhb	DHSB_MOUSE	4
Succinyl-CoA ligase [ADP/GDP-forming] subunit alpha, mitochondrial	Suclg1	SUCA_MOUSE	2
Succinyl-CoA ligase [ADP-forming] subunit beta, mitochondrial	Sucla2	SUCB1_MOUSE	4
<u>Glycosylation</u>			
Alpha-1,3/1,6-mannosyltransferase ALG2	Alg2	ALG2_MOUSE	3
UDP-glucose:glycoprotein glucosyltransferase 1	Uggt1	UGGG1_MOUSE	5
<u>Immune Response</u>			
Neurotrimin	Ntm	NTRI_MOUSE	3
Parathymsin	Ptms	PTMS_MOUSE	2
Toll-interacting protein	Tollip	TOLIP_MOUSE	2
<u>Ion Channel/Transporter</u>			
Calcium-binding mitochondrial carrier protein Aralar1	Slc25a12	CMC1_MOUSE	15
cGMP-gated cation channel alpha-1	Cnga1	CNGA1_MOUSE	7
Excitatory amino acid transporter 1	Slc1a3	EAA1_MOUSE	5
Excitatory amino acid transporter 2	Slc1a2	EAA2_MOUSE	5
Isoform 2 of Protein tweety homolog 1	Ttyh1	TTYH1_MOUSE	2
Isoform 2 of Vesicular inhibitory amino acid transporter	Slc32a1	VIAAT_MOUSE	7
Mitochondrial 2-oxoglutarate/malate carrier protein	Slc25a11	M2OM_MOUSE	2

Mitochondrial carrier homolog 2	Mtch2	MTCH2_MOUSE	2
Mitochondrial glutamate carrier 1	Slc25a22	GHC1_MOUSE	4
Monocarboxylate transporter 1	Slc16a1	MOT1_MOUSE	3
Plasma membrane calcium-transporting ATPase 2	Atp2b2	AT2B2_MOUSE	3
Potassium voltage-gated channel subfamily B member 1	Kcnb1	KCNB1_MOUSE	2
Protein Cngb1	Cngb1	Q91WA8_MOUSE	3
Protein Cngb1	Cngb1	E9PXX0_MOUSE	2
Protein Slc24a1	Slc24a1	Q91WD8_MOUSE	2
Retinal-specific ATP-binding cassette transporter	Abca4	ABCA4_MOUSE	19
Sarcoplasmic/endoplasmic reticulum calcium ATPase 2	Atp2a2	AT2A2_MOUSE	6
Sideroflexin-1	Sfxn1	SFXN1_MOUSE	3
Sideroflexin-3	Sfxn3	SFXN3_MOUSE	4
Sideroflexin-5	Sfxn5	SFXN5_MOUSE	3
Sodium- and chloride-dependent GABA transporter 1	Slc6a1	SC6A1_MOUSE	3
Sodium- and chloride-dependent GABA transporter 3	Slc6a11	S6A11_MOUSE	4
Sodium/potassium-transporting ATPase subunit beta-1	Atp1b1	AT1B1_MOUSE	8
Sodium/potassium-transporting ATPase subunit beta-2	Atp1b2	AT1B2_MOUSE	9
Sodium/potassium-transporting ATPase subunit beta-3	Atp1b3	AT1B3_MOUSE	4
Sodium-coupled neutral amino acid transporter 3	Slc38a3	S38A3_MOUSE	2
Vesicular glutamate transporter 1	Slc17a7	VGLU1_MOUSE	2
Voltage-dependent anion-selective channel protein 3	Vdac3	VDAC3_MOUSE	7
<u>Lipid Transport/Synthesis/Metabolism</u>			
1-acyl-sn-glycerol-3-phosphate acyltransferase gamma	Agpat3	PLCC_MOUSE	2
3-hydroxyacyl-CoA dehydrogenase type-2	Hsd17b10	HCD2_MOUSE	2
3-ketoacyl-CoA thiolase A, peroxisomal	Acaa1a	THIKA_MOUSE	4
Acyl-CoA dehydrogenase family member 9, mitochondrial	Acad9	ACAD9_MOUSE	3
Enoyl-CoA delta isomerase 1, mitochondrial	Eci1	ECI1_MOUSE	4
Estradiol 17-beta-dehydrogenase 12	Hsd17b12	DHB12_MOUSE	2
Hydroxyacyl-coenzyme A dehydrogenase, mitochondrial	Hadh	HCDH_MOUSE	3

Inorganic pyrophosphatase 2, mitochondrial	Ppa2	D3Z636_MOUSE	2
Isoform 2 of Long-chain-fatty-acid--CoA ligase 6	Acsl6	ACSL6_MOUSE	6
Long-chain fatty acid transport protein 1	Slc27a1	S27A1_MOUSE	2
Long-chain specific acyl-CoA dehydrogenase, mitochondrial	Acadl	ACADL_MOUSE	2
Medium-chain specific acyl-CoA dehydrogenase, mitochondrial	Acadm	ACADM_MOUSE	4
Neutral cholesterol ester hydrolase 1	Nceh1	NCEH1_MOUSE	2
Trifunctional enzyme subunit alpha, mitochondrial	Hadha	ECHA_MOUSE	5
Trifunctional enzyme subunit beta, mitochondrial	Hadhb	ECHB_MOUSE	3
Very long-chain specific acyl-CoA dehydrogenase, mitochondrial	Acadvl	ACADV_MOUSE	2
Very-long-chain (3R)-3-hydroxyacyl-[acyl-carrier protein] dehydratase 3	ptplad1	HACD3_MOUSE	2
<u>Neurotransmitter Regulation and Synthesis</u>			
4-trimethylaminobutyraldehyde dehydrogenase	Aldh9a1	AL9A1_MOUSE	2
Glutamate decarboxylase 1	Gad1	DCE1_MOUSE	2
Glutaminase kidney isoform, mitochondrial	Gls	GLSK_MOUSE	10
Isoform 2 of 4-aminobutyrate aminotransferase, mitochondrial	Abat	GABT_MOUSE	7
Succinate-semialdehyde dehydrogenase, mitochondrial	Aldh5a1	SSDH_MOUSE	5
<u>Oxidation/Reduction</u>			
Alcohol dehydrogenase class-3	Adh5	ADHX_MOUSE	2
Aldehyde dehydrogenase, mitochondrial	Aldh2	ALDH2_MOUSE	4
Biliverdin reductase A	Blvra	BIEA_MOUSE	2
Carbonyl reductase [NADPH] 3	Cbr3	CBR3_MOUSE	2
D-beta-hydroxybutyrate dehydrogenase, mitochondrial	Bdh1	BDH_MOUSE	2
Glutathione peroxidase	Gpx4	GPX41_MOUSE	2
Isoform 2 of Alpha-amino adipic semialdehyde dehydrogenase	Aldh7a1	AL7A1_MOUSE	2
Isoform 4 of Oxidation resistance protein 1	Oxr1	OXR1_MOUSE	5
NAD-dependent malic enzyme, mitochondrial	Me2	MAOM_MOUSE	4
NADPH--cytochrome P450 reductase	Por	NCPR_MOUSE	3
Retinol dehydrogenase 12	Rdh12	RDH12_MOUSE	9
Saccharopine dehydrogenase-like oxidoreductase	Sccpdh	SCPDL_MOUSE	2

Serum paraoxonase/arylesterase 1	Pon1	PON1_MOUSE	2
Superoxide dismutase [Mn], mitochondrial	Sod2	SODM_MOUSE	7
Thioredoxin-dependent peroxide reductase, mitochondrial	Prdx3	PRDX3_MOUSE	2
Thioredoxin-related transmembrane protein 1	Tmx1	TMX1_MOUSE	2
Trans-1,2-dihydrobenzene-1,2-diol dehydrogenase	Dhdh	DHDH_MOUSE	2

Phospholipid Transport

Phosphatidylinositol transfer protein alpha isoform	Pitpna	PIPNA_MOUSE	2
---	--------	-------------	---

Protein Synthesis

40S ribosomal protein S10	Rps10	RS10_MOUSE	3
40S ribosomal protein S20	Rps20	RS20_MOUSE	2
40S ribosomal protein S26	Rps26	RS26_MOUSE	2
60S acidic ribosomal protein P2	Rplp2	RLA2_MOUSE	4
60S ribosomal protein L31	Rpl31	RL31_MOUSE	2
ATP-dependent RNA helicase A	Dhx9	E9QNN1_MOUSE	6
ATP-dependent RNA helicase DDX19A	Ddx19a	DD19A_MOUSE	2
Elongation factor Tu, mitochondrial	Tufm	EFTU_MOUSE	5
Eukaryotic initiation factor 4A-III	Eif4a3	IF4A3_MOUSE	2
Eukaryotic translation initiation factor 2 subunit 1	Eif2s1	IF2A_MOUSE	3

ProteinTransport

AP-1 complex subunit beta-1	Ap1b1	AP1B1_MOUSE	9
AP-3 complex subunit beta-2	Ap3b2	AP3B2_MOUSE	3
Coatomer subunit beta'	Copb2	COPB2_MOUSE	3
Conserved oligomeric Golgi complex subunit 3	Cog3	COG3_MOUSE	2
Cytoplasmic dynein 1 intermediate chain 2	Dync1i2	A2BFF5_MOUSE	4
Disks large homolog 1	Dlg1	E9Q9H0_MOUSE	3
Endoplasmic reticulum-Golgi intermediate compartment protein 1	Ergic1	ERGI1_MOUSE	2
Erlin-2	Erlin2	ERLN2_MOUSE	2
Exportin-1	Xpo1	XPO1_MOUSE	4

Importin-5	Ipo5	IPO5_MOUSE	3
Isoform 2 of MAGUK p55 subfamily member 2	Mpp2	MPP2_MOUSE	7
Isoform 2 of TOM1-like protein 2	Tom1l2	TM1L2_MOUSE	2
Isoform B of AP-2 complex subunit alpha-1	Ap2a1	AP2A1_MOUSE	2
Kinectin	Ktn1	F8VQC7_MOUSE	2
Mitochondrial import inner membrane translocase subunit TIM50	Timm50	TIM50_MOUSE	2
Mitochondrial import receptor subunit TOM70	Tomm70a	TOM70_MOUSE	3
Nuclear transport factor 2	Nutf2	NTF2_MOUSE	2
PRA1 family protein 2	Praf2	PRAF2_MOUSE	2
PRA1 family protein 3	Arl6ip5	PRAF3_MOUSE	2
Protein ERGIC-53	Lman1	LMAN1_MOUSE	5
Protein MGARP (Fragment)	Mgarp	D3Z134_MOUSE	2
Protein transport protein Sec23A	Sec23a	E9Q1S3_MOUSE	2
Transmembrane emp24 domain-containing protein 10	Tmed10	TMEDA_MOUSE	2
Transportin-1 (Fragment)	Tnpo1	Q3TKD0_MOUSE	4
<u>Proteasome Degradation/Protease</u>			
26S proteasome non-ATPase regulatory subunit 11	Psm11	PSD11_MOUSE	2
26S proteasome non-ATPase regulatory subunit 2	Psm2	PSMD2_MOUSE	5
Cathepsin B	Ctsb	CATB_MOUSE	2
Cathepsin D (Fragment)	Ctsd	F6Y6L6_MOUSE	4
Dipeptidyl peptidase 3	Dpp3	DPP3_MOUSE	4
E3 ubiquitin-protein ligase NEDD4	Nedd4	NEDD4_MOUSE	4
Isoform 2 of Protein phosphatase 1H	Ppm1h	PPM1H_MOUSE	2
Proteasome subunit alpha type-4	Psm4	PSA4_MOUSE	2
Proteasome subunit beta type-2	Psm2	PSB2_MOUSE	3
Proteasome subunit beta type-3	Psm3	PSB3_MOUSE	2
Protein DDI1 homolog 2	Ddi2	DDI2_MOUSE	2
Ubiquilin-2	Ubqln2	UBQL2_MOUSE	3
Ubiquitin carboxyl-terminal hydrolase	Usp7	UBP7_MOUSE	4

Ubiquitin thioesterase OTUB1	Otub1	OTUB1_MOUSE	6
<u>RNA Metabolism</u>			
60 kDa SS-A/Ro ribonucleoprotein	Trove2	RO60_MOUSE	2
Aspartate--tRNA ligase, cytoplasmic	Dars	SYDC_MOUSE	3
CCA tRNA nucleotidyltransferase 1, mitochondrial	Trnt1	TRNT1_MOUSE	3
Glycine--tRNA ligase	Gars	SYG_MOUSE	3
Heterogeneous nuclear ribonucleoprotein H2	Hnrnph2	HNRH2_MOUSE	2
Heterogeneous nuclear ribonucleoprotein U-like protein 2	Hnrnpul2	HNRL2_MOUSE	2
Isoleucine--tRNA ligase, mitochondrial	Iars2	SYIM_MOUSE	2
Poly(rC)-binding protein 4	Pcbp4	PCBP4_MOUSE	2
Pre-mRNA-processing-splicing factor 8	Prpf8	PRP8_MOUSE	2
Probable ATP-dependent RNA helicase DDX6	Ddx6	DDX6_MOUSE	3
Probable C->U-editing enzyme APOBEC-2	Apobec2	ABEC2_MOUSE	2
Ribonuclease inhibitor	Rnh1	RINI_MOUSE	3
RNA-binding protein 14	Rbm14	RBM14_MOUSE	2
Small nuclear ribonucleoprotein-associated protein B	Snrpb	RSMB_MOUSE	2
Splicing factor U2AF 35 kDa subunit	U2af1	U2AF1_MOUSE	2
<u>Signal Transduction</u>			
Diacylglycerol kinase epsilon	Dgke	DGKE_MOUSE	2
G protein-coupled receptor kinase 1	Grk1	RK_MOUSE	14
GTP-binding protein Di-Ras2	Diras2	DIRA2_MOUSE	2
Guanine nucleotide-binding protein G(i) subunit alpha-2	Gnai2	GNAI2_MOUSE	4
Guanine nucleotide-binding protein G(l)/G(s)/G(t) subunit beta-3	Gnb3	GBB3_MOUSE	2
Guanine nucleotide-binding protein G(q) subunit alpha	Gnaq	GNAQ_MOUSE	7
Guanine nucleotide-binding protein G(s) subunit alpha isoforms short	Gnas	GNAS2_MOUSE	3
Guanine nucleotide-binding protein G(t) subunit alpha-2	Gnat2	GNAT2_MOUSE	4
Guanine nucleotide-binding protein G(z) subunit alpha	Gnaz	GNAZ_MOUSE	4
Guanine nucleotide-binding protein subunit alpha-14	Gna14	GNA14_MOUSE	3
Guanine nucleotide-binding protein subunit beta-2-like 1	Gnb211	GBLP_MOUSE	3

Guanylyl cyclase GC-E	Gucy2e	GUC2E_MOUSE	15
Isoform 1 of Regulator of G-protein signaling 9	Rgs9	RGS9_MOUSE	11
Isoform 2 of Guanine nucleotide-binding protein subunit beta-5	Gnb5	GBB5_MOUSE	3
Isoform 2 of Neurochondrin	Ncdn	NCDN_MOUSE	2
Phosphodiesterase 6A, cGMP-specific, rod, alpha	Pde6a	Q8K0A8_MOUSE	26
Protein Rap1gap	Rap1gap	A2ALS5_MOUSE	2
Ras-related protein Rab-10	Rab10	RAB10_MOUSE	2
Ras-related protein Rab-11B	Rab11b	RB11B_MOUSE	4
Ras-related protein Rab-18	Rab18	RAB18_MOUSE	2
Ras-related protein Rab-1B	Rab1b	RAB1B_MOUSE	3
Ras-related protein Rab-3C	Rab3c	RAB3C_MOUSE	3
Ras-related protein Rab-5A	Rab5a	RAB5A_MOUSE	3
Ras-related protein Rab-5B	Rab5b	RAB5B_MOUSE	3
Ras-related protein Rab-5C	Rab5c	RAB5C_MOUSE	2
Ras-related protein Rab-6B	Rab6b	RAB6B_MOUSE	3
Ras-related protein Rap-1A	Rap1a	RAP1A_MOUSE	3
Regulator of G-protein signaling 9-binding protein	Rgs9bp	R9BP_MOUSE	3
Rho GTPase-activating protein 1	Arhgap1	A2AH25_MOUSE	6
Rod cGMP-specific 3',5'-cyclic phosphodiesterase subunit beta	Pde6b	PDE6B_MOUSE	10
Serine/threonine-protein phosphatase 2A 55 kDa regulatory subunit B alpha isoform	Ppp2r2a	2ABA_MOUSE	3
Short-wave-sensitive opsin 1	Opn1sw	OPSB_MOUSE	2
<u>Stress Response</u>			
Constitutive coactivator of PPAR-gamma-like protein 1	FAM120A	F120A_MOUSE	2
Heat shock 70 kDa protein 12A	Hspa12a	HS12A_MOUSE	6
Hypoxia up-regulated protein 1	Hyou1	HYOU1_MOUSE	6
<u>Synaptic Transmission</u>			
Isoform 2 of Solute carrier family 12 member 5	Slc12a5	S12A5_MOUSE	16

Protein lin-7 homolog A	Lin7a	LIN7A_MOUSE	4
Synaptic vesicle glycoprotein 2B	Sv2b	SV2B_MOUSE	4
Synaptic vesicle membrane protein VAT-1 homolog-like	Vat1l	VAT1L_MOUSE	2
Synaptopodin	Synpr	SYNPR_MOUSE	4
Syntaxin-1B	Stx1b	STX1B_MOUSE	10
Vesicle-associated membrane protein-associated protein A	Vapa	VAPA_MOUSE	5

Transcription Regulation

Alpha/beta hydrolase domain-containing protein 14B	Abhd14b	E9QN99_MOUSE	2
Coiled-coil-helix-coiled-coil-helix domain-containing protein 3, mitochondrial	Chchd3	CHCH3_MOUSE	3
Isoform 2 of Mitochondrial inner membrane protein	Immt	IMMT_MOUSE	19
Isoform Epsilon of Lamina-associated polypeptide 2, isoforms beta/delta/epsilon/gamma	Tmpo	LAP2B_MOUSE	7
Protein arginine N-methyltransferase 1	Prmt1	ANM1_MOUSE	2
Transcription elongation factor B polypeptide 2	Tceb2	ELOB_MOUSE	2

Transferase

Dihydrolipoyllysine-residue succinyltransferase component of 2-oxoglutarate dehydrogenase complex, mitochondrial	Dlst	ODO2_MOUSE	4
Farnesyl pyrophosphate synthase	Fdps	FPPS_MOUSE	4
Isoform 2 of NAD kinase 2, mitochondrial	Nadk2	NAKD2_MOUSE	2
Ornithine aminotransferase, mitochondrial	Oat	OAT_MOUSE	5
Phosphoserine aminotransferase	Psat1	SERC_MOUSE	4
Succinyl-CoA:3-ketoacid coenzyme A transferase 1, mitochondrial	Oxct1	SCOT1_MOUSE	12

Vesicle Transport

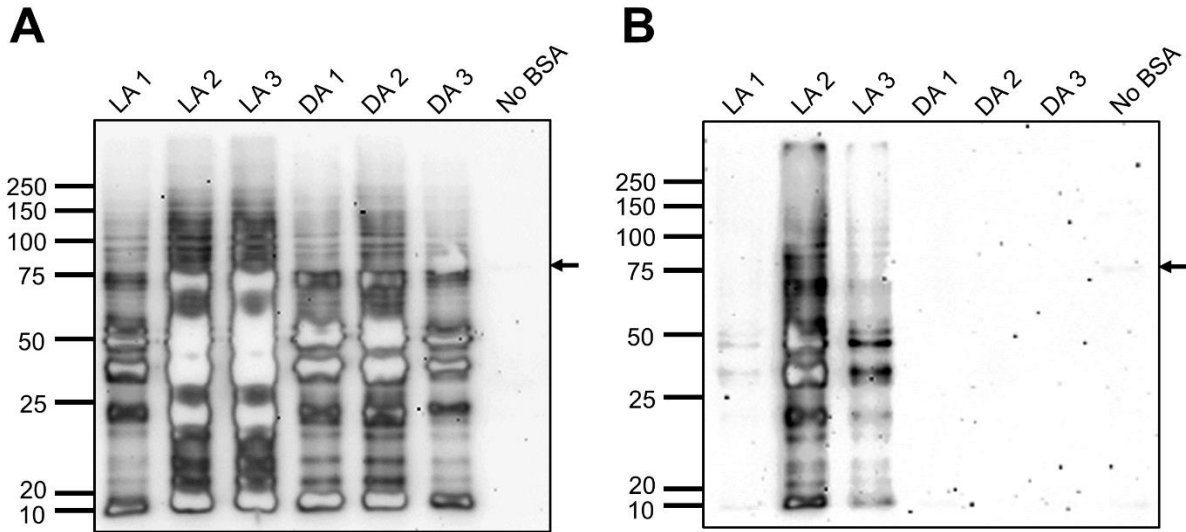
Protein NipSnap homolog 2	Gbas	NIPS2_MOUSE	3
Protein Sptbn2	Sptbn2	Q68FG2_MOUSE	3

Others

Adipocyte plasma membrane-associated protein	Apmap	APMAP_MOUSE	2
C2 domain-containing protein 2-like	C2cd2l	C2C2L_MOUSE	4

Ceruloplasmin	Cp	CERU_MOUSE	2
COP9 signalosome complex subunit 1	Gps1	G3UXW9_MOUSE	4
Delta-aminolevulinic acid dehydratase	Alad	HEM2_MOUSE	2
DmX-like protein 2	Dmxl2	DMXL2_MOUSE	4
Endophilin-B2	Sh3glb2	SHLB2_MOUSE	2
EPM2A-interacting protein 1	Epm2aip1	EPMIP_MOUSE	3
ES1 protein homolog, mitochondrial	D10Jhu81e	ES1_MOUSE	3
Galectin-related protein	Lgalsl	LEGL_MOUSE	4
Gamma-crystallin A	Cryga	CRGA_MOUSE	2
Golgi apparatus protein 1 (Fragment)	Glg1	GSLG1_MOUSE	2
Golgi reassembly stacking protein 2, isoform CRA_d	Gorasp2	GORS2_MOUSE	3
Isochorismatase domain-containing protein 2A, mitochondrial	Isoc2a	ISC2A_MOUSE	2
LanC-like protein 2	Lancl2	LANC2_MOUSE	2
Leucine-rich repeat-containing protein 59	Lrrc59	LRC59_MOUSE	3
Low molecular weight phosphotyrosine protein phosphatase	Acp1	PPAC_MOUSE	2
MCG140784	Try10	Q792Z1_MOUSE	2
NAD(P)H-hydrate epimerase	Apoa1bp	NNRE_MOUSE	2
PEX5-related protein	Pex5l	D3YYH0_MOUSE	2
Phosphoribosyl pyrophosphate synthase-associated protein 2	Prpsap2	KPRB_MOUSE	2
Protein Ahnak2 (Fragment)	Ahnak2	F7DBB3_MOUSE	3
Protein NDRG3	Ndr3	NDRG3_MOUSE	2
Protein SET (Fragment)	Set	SET_MOUSE	2
Tumor protein D52 (Fragment)	Tpd52	D3Z125_MOUSE	2
Uncharacterized protein	Tubb4b-ps1	J3QNR5_MOUSE	2
Up-regulated during skeletal muscle growth protein 5	Usmg5	USMG5_MOUSE	2

Appendix III:



Western blots of biotinylated proteins from retinal homogenates following biotin switch assay.

Retinal homogenates from three light-adapted (LA) or dark-adapted (DA) mice were subjected to the biotin switch assay (BSA, See Chapter 2 Materials and Methods) and the presence of biotin was confirmed by western blot. Biotin was detected using the S-nitrosylation Detection Reagent I (conjugated to Horseradish Peroxidase) (Cayman Chemical, Item #10006524) followed by detection using enhanced chemiluminescence. **A:** Immunoblot of retinal lysates collected after biotin switch assay (BSA), prior to enrichment with neutravidin agarose (Pierce), so the sample contained proteins with and without biotin. Total protein concentration was $\sim 10 \mu\text{g}/\mu\text{L}$ for all samples. $7.5 \mu\text{L}$ of lysate was mixed with $2.5 \mu\text{L}$ 4X sample buffer for a total volume of $10 \mu\text{L}$ loaded per lane. Lanes 1-6 contain lysates that were collected following the BSA. Lane 7 contained retinal lysates that were not subjected to BSA as a control for endogenously biotinylated proteins (arrow). **B:** Western blot showing biotinylated proteins after purification with neutravidin. Protein concentrations were lower following purification: LA 1 $\sim 1 \mu\text{g}/\mu\text{L}$, LA 2 & LA 3 $\sim 2 \mu\text{g}/\mu\text{L}$, DA 1, 2 & 3 $\sim 0.5 \mu\text{g}/\mu\text{L}$. Each lane was loaded with $5 \mu\text{L}$ of lysate mixed with $2 \mu\text{L}$ 4X sample buffer for a total volume of $7 \mu\text{L}$. Instead of normalizing each sample to a determined protein concentration, a single volume of protein sample was used for all lanes to allow for gross comparison of S-nitrosylation as measured by the detection of biotin. Second, a minimal volume of sample was used for western blot experiments in order to maximize the amount of enriched protein sample that was used for qualitative MS analysis. The low protein concentration of the LA1 and DA 1, 2, & 3 samples made detection of biotin difficult, however the $5 \mu\text{L}$ used was 10% of the entire sample volume on hand. Had we used more for the western blot, we may have hindered our ability to determine protein identities through MS analysis. Lane 7 contained retinal lysates that were not subjected to BSA as a control for endogenously biotinylated proteins (arrow).

The results we present here, particularly the banding patterns that can be seen in A and B, are consistent with Jaffrey et al. (2001) who developed the BSA and used it to describe S-nitrosylation of brain proteins following incubation with an NO donor.

Appendix IV:

J. Neurosci's Permissions Policy

http://www.jneurosci.org/site/misc/Permissions_Policy.pdf

October 2, 2014 (Accessed on March 30, 2015)

Starting in January of 2010, *The Journal of Neuroscience* adopted a License to Publish form to replace the previously used copyright form. The License to Publish form allows authors to retain the copyright to their article while granting the Society for Neuroscience a 6-month period to exclusively publish the article.

After six months, anyone may use the material for non-commercial purposes under the terms of the Creative Commons Attribution-Noncommercial-Share Alike 3.0 Unported License (<http://creativecommons.org/licenses/by-nc-sa/3.0>). This agreement allows data and text mining, use of figures in presentations, and posting the article online, as long as the original article is attributed.

Authors need NOT contact the journal to obtain rights for any non-commercial reuse their own material so long as authors provide attribution to the place of original publication and, for the first six months after publication, refrain from making the work publicly available. Authors are automatically granted permission to:

- Reuse the article in print collections of their own writing.
- Present a work orally in its entirety.
- Use an article in a thesis and/or dissertation.
- Reproduce an article for use in the author's courses.
- Reuse a figure, photo and/or table in future non-commercial works.

For any non-author uses of the work, please follow the “get permissions” link in the sidebar to the right of any full text article in *J. Neurosci*. This link will take you to [Copyright Clearance Center](#), which processes these requests for *J. Neurosci*.

If you are requesting permission to reprint with a nonprofit publisher, please email a detailed request directly to jnpermissions@sfn.org. In most cases, these requests are granted at no cost.

Anyone requesting to reprint with a for-profit publisher, there will be a charge for each figure you reuse. We do not process these fees directly, but you can request permission online through the [Copyright Clearance Center](#) website.

Please contact the *J. Neurosci's* Central office at jnpermissions@sfn.org with any questions.